Title
Mechano-NPS and Visco-NPS: Microfluidic Approaches to Single-Cell Mechanics

Author
Kim, Junghyun

Publication Date
2018

Peer reviewed|Thesis/dissertation

Mechano-NPS and Visco-NPS:
Microfluidic Approaches to Single-Cell Mechanics

By

Junghyun Kim

A dissertation submitted in partial satisfaction of the

requirements for the degree of

Doctor of Philosophy

in

Engineering – Mechanical Engineering

in the

Graduate Division

of the

University of California, Berkeley

Committee in charge:

Professor Lydia L. Sohn, Chair
Professor Michael Lustig
Professor Grace O'Connell

Fall 2018

Abstract

Mechano-NPS and Visco-NPS: Microfluidic Approaches to Single-Cell Mechanics
By
Junghyun Kim
Doctor of Philosophy in Engineering – Mechanical Engineering
in the Graduate Division of
the University of California, Berkeley
Professor Lydia L. Sohn, Chair

The mechanical properties of cells provide valuable information regarding biological and clinically relevant cellular characteristics. In this dissertation, we demonstrate two new microfluidic platforms, mechano-node-pore sensing (mechano-NPS) and visco-node-pore sensing (visco-NPS), to characterize cellular mechanical behavior. Mechano-NPS is a multi-parametric single-cell-analysis method to quantify simultaneously cell diameter, resistance to compressive deformation, transverse deformation under constant strain, and recovery time after deformation. We define a new parameter, the whole-cell deformability index (*wCDI*), which provides a quantitative mechanical metric of the resistance to compressive deformation that can be used to discriminate among different cell types. The *wCDI* and the transverse deformation under constant strain show malignant MCF-7 and A549 cell lines are mechanically distinct from non-malignant, MCF-10A and BEAS-2B cell lines. We categorize cell recovery time and show that the composition of recovery types, which is a consequence of changes in cytoskeletal organization, correlates with cellular transformation. Through the *wCDI* and cell-recovery time, mechano-NPS discriminates between sub-lineages of normal primary human mammary epithelial cells. Mechano-NPS identifies mechanical phenotypes that distinguishes lineage, chronological age, and stage of malignant progression in human epithelial cells.

Visco-NPS is a new, electronic-based, microfluidic rheology platform that quantifies cellular viscoelastic properties under periodic deformation. We measure the storage (G') and loss (G'') modulus of individual cells, which represent cellular elasticity and viscosity, respectively. By applying a wide range of deformation frequency, our platform quantifies the frequency dependency of viscoelastic properties. The measurement of G' and G'' shows that malignant breast epithelial (MCF-7) cells have distinctly different viscoelastic properties as compared to non-malignant breast epithelial (MCF-10A) cells. With its sensitivity, visco-NPS is able to dissect the individual contributions of different cytoskeletal components, i.e. actin filaments and microtubules, to whole-cell mechanical properties. Through G' and G'', visco-NPS can also quantify the mechanical transitions—a consequence of changes in cytoskeletal organization and nucleus structure—that cells undergo as they traverse the cell cycle. visco-NPS identifies viscoelastic characteristics of cells, which can provide both a biophysical understanding of cellular behavior and a potential for clinical applications.

To my family —
Lovely Hyeri,
my parents, my sister,
and relatives from both my parents' and my parents-in-law's sides

ACKNOWLEDGEMENTS

I'd like to specially thank my research advisors at UC Berkeley. Lydia L. Sohn—you are a true educator, researcher, and the spiritual mother of my life in the US. You have been a candle in my life, giving me a direction for where to head next. I couldn't have completed my PhD without your terrific mentorship, advice, support and input. Michael Lustig, you have taught me how to handle preliminary dataset and analyze electrical signals in effective ways. Grace O'Connell, who served as one of my qualifying exam committee members—I valued your lectures; they opened my eyes to the intersection of cellular mechanics and microfluidics. I also appreciate to Mohammad Mofrad who was also one of my qualifying exam committee members for his keen insights and feedback on my research.

I also thank faculty members from outside the Berkeley campus. I thank Mark A. LaBarge at City of Hope and Zev J. Gartner at UCSF, none of whom had any official role in dissertation, but who provided me with invaluable feedback and comments on my research. I also thank Masaru Miyano and Jessica Bloom at LBNL; Vasudha Srivastava at UCSF. Academic discussions and collaborating with them inspired me and helped to broaden my research topics.

I am grateful to Linda von Hoene, Assistant Dean for Professional Development in the GSI Teaching and Resource Center at UC Berkeley, for giving me the chance to become a fellow of Summer Institute for Preparing Future Faculty.

I thank fellowships I have been received, Graduate Student Fellowship from Jungsong foundation, Block Grant Award from UC Berkeley, and John-and-Janet McMurty fellowship throughout the many years.

I have learned a lot from my fellow Ph.D. students and post-doctoral researchers in the Sohn Lab. Olivia Scheideler, Nahyun Cho, Roberto Flacon, Thomas Carey, Brian Li, Kristen Cotner, Sewoon Han, Daniel Yang, Nathaniel Liu, and Molly Kozminsky—your paths and journeys in the Sohn Lab have become guidance for my research. You provided meaningful conversations that were a significant contribution to my Ph.D. life.

I wish to thank my amazing undergraduate researchers: Andy Lei, Youngbin Kim, Bita Mehziz, Jeremy Whang, and Justin Inman.

I also thank the administrative staff on campus. I thank Shareena Samson, Yawo Akpawu, Donna Frances Craig from the Department of Mechanical Engineering and all staff from QB3 Berkeley. Their support and collaboration on administrative matters enabled me to keep focused on what I had to do as a graduate student on campus.

Lastly, I thank my family for their endless support, patience, and love. My wife, my parents, my brother, and relatives from both my parents' and my parents-in-law's sides in Korea have been the strongest supporters of my Ph.D. studies. Without their sacrifices, I would not have been able to complete such a long journey abroad.

Table of Contents

List of Figures

List of Tables

1 INTRODUCTION

Chapter Overview

This introduction summarizes the motivation for the research and the organization of the chapters in this dissertation.

1.1 Motivation

Cellular mechanical properties correspond to the biological status and function of cells and originate from the structure and dynamics of their intracellular components. To quantify the mechanical characteristics of cells, various methods have been developed (Figure 1.1). As a gold standard, Atomic Force Microscopy (AFM) (1-3) and micropipette aspiration (4, 5) have been widely used. However, they are burdened by slow analyzing speed, only just a few cells/hr (6, 7). Similarly, other traditional measurements—optical tweezers (8, 9) and microplate rheometer (10)—also suffer from low throughput. Given these circumstances, new approaches to mechanical phenotyping are replacing these traditional measurements. For example, hydrodynamic stretching cytometry (11), suspended microchannel resonators (SMR) (12), and real-time deformability cytometry (RT-DC) (13, 14) have been developed for high-throughput analysis. Even though these methods introduce efficient ways of mechanical phenotyping for identifying specific cell types, they do not provide the means to screen complex cellular mixtures and to investigate basic cellular mechanics. Thus, despite the many different platforms for cell mechanical measurements that exist today, none thus far have been able to provide a robust screening platform and a comprehensive view of cellular mechanics.

This dissertation describes two new microfluidic approaches to quantify mechanical characteristics of single-cell populations. First, a novel microfluidic platform called "mechano-Node-Pore Sensing" (mechano-NPS) is introduced. Mechano-NPS involves integrating a node-pore sensor (15, 16) with a contraction channel and performing a four-terminal measurement of the current across the integrated microfluidic channel. Using this *electronic-based* method, mechano-NPS quantifies simultaneously four different biophysical properties of a single cell: free-cell size, amount of deformation, resistance to compressive deformation, and recovery time after releasing from the deformation. Mechano-NPS provides the means to use these biophysical parameters as label-free biomarkers for identification and differentiation among cell types and, uniquely, to determine the effects of chronological age and malignant progression based on cell elasticity and recovery from deformation.

Second, visco-node-pore sensing (visco-NPS), a method to measure viscoelastic properties of cells, is also introduced. Visco-NPS employs a rheological approach by including a contraction channel with periodically changing width to induce oscillating deformation to cells. By integrating this channel with a node-pore sensor (15, 16), visco-NPS enables the measurement of the storage (elasticity) and loss (viscosity) modulus of cells. This microfluidic rheology platform successfully quantifies differences in viscoelastic properties between malignant and non-malignant breast epithelial cells. The contribution of cytoskeletal components including actin filaments and microtubules to whole cell viscoelastic properties can be analyzed. In addition, this approach enables evaluation of the effects of dynamic cellular transitions that occur during different cell-cycle phases on the mechanical behavior of cells.

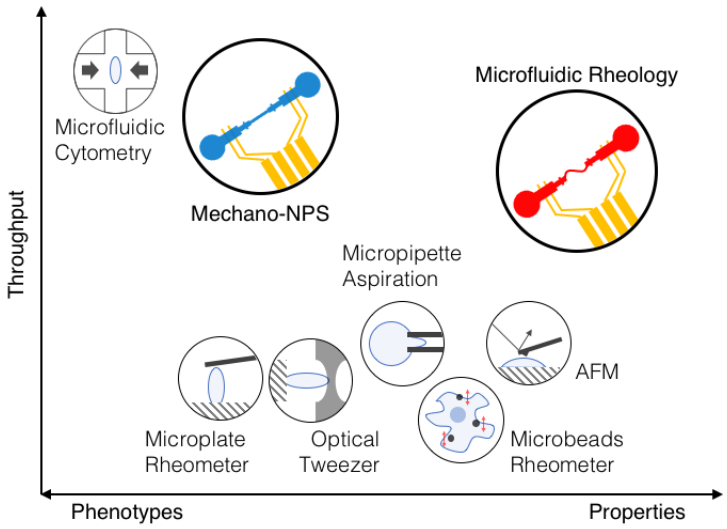

Figure 1-1. Comparison of mechano-NPS and visco-NPS to existing platforms used to quantify cellular mechanical properties.

1.2 Organization of the Dissertation

This dissertation begins with an introduction to resistive pulse sensing, node-pore sensing, and single-cell mechanics. Thereafter, this dissertation delves into the development and applications of a mechano- and visco-NPS. Finally, this dissertation concludes with key findings and recommendations for future research.

- **CHAPTER 1. INTRODUCTION**
  This introduction summarizes the motivation for the research and the organization of the chapters in the dissertation.

- **CHAPTER 2. THEORETICAL CONSIDERATIONS**

This chapter provides a theoretical consideration of resistive-pulse sensing, node-pore sensing, contraction-based cellular deformation, and rheological approach to single-cell mechanics.

- **CHAPTER 3. DEVICE FABRICATION AND MEASUREMENT**
  This chapter presents descriptions of device fabrication procedures and equipment set up for the measurement.

- **CHAPTER 4. MULTI-VARIABLE MECHANICAL PHENOTYPING**
  This chapter introduces a microfluidic platform for mechanical phenotyping of cancer cells, describes detailed experimental methods, and presents data of malignant and non-malignant epithelial cells acquired from the microfluidic platform.

- **CHAPTER 5. MECHANICAL PHENOTYPING OF HUMAN MAMMARY EPITHELIAL CELLS**
  This chapter describes the pre-clinical study of human mammary epithelial cells using the assay that was introduced in Chapter 4.

- **CHAPTER 6. MICROFLUIDIC RHEOLOGY THROUGH VISCO-NODE-PORE SENSING**
  This chapter introduces a new microfluidic approach to quantify viscoelastic properties of cells in a high-throughput manner. The detailed experimental methods and results are presented to show its capability to compare mechanical properties of various cell lines and to evaluate the contribution of sub-cellular components to whole-cell properties.

- **CHAPTER 7. CELLULAR TRANSITION AND MECHANICAL PHENOTYPING**
  This chapter explores the application of cellular mechanical phenotyping through microfluidic approaches. In particular, Epithelial to Mesenchymal Transition (EMT) and tissue growth potential of Nucleus Pulposus Cells (NPCs) are screened for their mechanical phenotypes.

- **CHAPTER 8. CONCLUSION AND FUTURE RESEARCH**
  This chapter summarizes the results of the dissertation research and provides overall conclusions and recommendations to academic scholars about single-cell mechanics.

2 THEORETICAL CONSIDERATIONS

Chapter Overview

This chapter provides the detailed theory behind resistive-pulse sensing (RPS), node-pore sensing (NPS), contraction-based mechanical phenotyping, and rheological approaches for single-cell mechanics. It details how RPS and NPS can be used to monitor the changes in electrical resistance in a microfluidic channel when a particle transits through and how such changes provide information on particle size and transit time. As well, this chapter also present principles of compressive mechanical phenotyping of cells, and describes single-cell rheology and the corresponding mechanical models to quantify viscoelastic properties of cells.

2.1 Principles of Resistive Pulse Sensing

Resistive-pulse sensing (RPS), also called the Coulter-counter technique (17, 18), has been used as a label-free method for detecting and characterizing biological samples, such as sizing various cells (15, 19, 20), detecting viruses (21, 22), and measuring cellular responses to stimuli (16, 23). The basic principle of RPS is measuring the change of electric current or resistance across a pore when a non-conductive particle passes through it (Figure 2-1). As such a particle transits a pore, it partially blocks the flow of current, resulting in a temporary decrease of the current. Once the particle exits from the pore, the current returns to the baseline value (I_{base}). By analyzing width and height of the current drop, we can quantify the particle size and transit time.

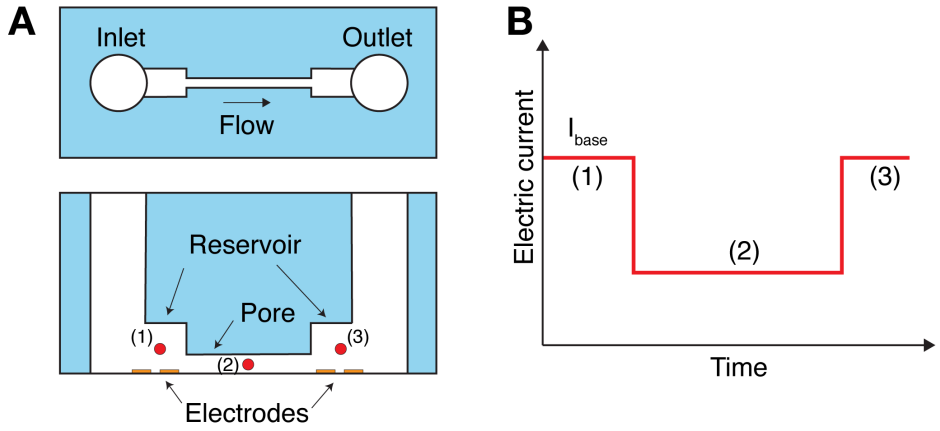

Figure 2-1. Principle of resistive pulse sensing. A, Top (top) and Side (bottom) view of the RPS platform. Red circles indicate a non-conductive particle in the channel. **B**, Electric-current pulse

produced by a particle transiting through the channel. Numbers correspond to positions of the particle in **A**. I_{base} denotes the baseline value of the electric current.

2.1.1 Particle Size Determination with RPS

RPS allows us to measure the size of particle in a pore by analyzing the change of electrical resistance. By the definition of electrical resistivity, the resistance of the pore (R) is

$$\boldsymbol{R = \rho \int \frac{dz}{A_{pore}(z)} = \frac{4\rho L}{\pi D^2}} \tag{2.1}$$

where ρ, A_{pore}, and L denote the electrical resistivity of the fluid and the cross-sectional area and length of the pore, respectively. When a non-conductive particle enters the pore, it displaces an equivalent volume of conductive fluid (Figure 2-2). This consequently increases the resistance across the pore at that time point. The increase in resistance (ΔR) is

$$\boldsymbol{\Delta R = \rho \int \frac{dz}{A_{pore}(z) - A_{particle}(z)} - \rho \int \frac{dz}{A_{pore}(z)}} \tag{2.2}$$

where $A_{particle}$ represent the cross-sectional area of particle.

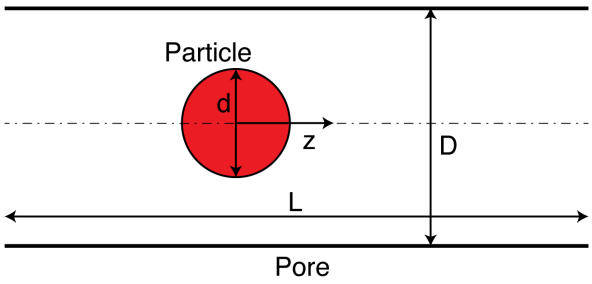

Figure 2-2. Definition of variables. Cross-sectional view of a spherical, non-conductive particle (red) in a pore. D and d are the diameter of particle and pore, respectively. L represents the length of the pore.

The solution to Equation (2.2) is dependent on the particle size relative to that of the pore. When the particle is infinitely small, the relative increase in resistance ($\Delta R/R$) is

$$\Delta R/R = d^3/D^2 L \tag{2.3}$$

where d, D, and L are the diameter of the particle and the diameter and length of the pore, respectively.

When the particle has a size that is relatively smaller than that of the pore ($d<D$), Deblois and Bean showed that the solution of Equation (2.2) is based on the distribution of the electric field lines around the particle (24). In this case, the increase of resistance is,

$$\frac{\Delta R}{R} = \frac{d^3}{D^2 L}\left[\frac{D^2}{2L^2} + \frac{1}{\sqrt{1+(D/L)^2}}\right] F\left(\frac{d^3}{D^3}\right) \tag{2.4}$$

where $F(d^3/D^3)$ is a numerical correction factor given by Deblois and Bean.

As the particle diameter approaches that of the pore diameter ($d\sim D$), Equation (2.4) is no longer applicable. In this case, and as Gregg and Steidley had examined in the limit of $d \leq D$ (25), the pore cross-sectional area without the particle is $A(z) = \pi D^2/4$, and with particle is $A(z) = \pi(D^2 - d^2 + 4z^2)/4$. Substituting $A(z)$ into Equation (2.1) and (2.2), the increase of resistance is thus,

$$\frac{\Delta R}{R} = \frac{D}{L}\left[\frac{arcsin(d/D)}{(1-(d/D)^2)^{0.5}} + \frac{d}{D}\right] \tag{2.5}$$

Although Equation (2.3), (2.4), and (2.5) successfully address the relationship between $\Delta R/R$ and the relative size of spherical particle, each equation only describes specific regime of particle size and the pore diameter.

To describe the intermediate regime (d/D=0.4~0.9), Deblois *et al.* used an experimental approach to determine $\Delta R/R$ (26-28),

$$\frac{\Delta R}{R} = \frac{d^3}{D^2 L}\left[\frac{1}{1-0.8(d/D)^3}\right] \tag{2.6}$$

In the measurements described in this dissertation, the relative change of current is approximately equal to the relative change of resistance ((|$\Delta I/I$|~|$\Delta R/R$|) because the resistance of the pore dominates.

2.1.2 Fluidic Flow in Microfluidic Channel

To drive particles through an RPS channel, we apply a non-pulsatile pressure to the channel inlet. Analyzing the Reynolds number (*Re*) gives us a full understanding of the fluidic conditions in the channel and the transit velocity of particles in pore. By definition,

$$\boldsymbol{Re} = \frac{\boldsymbol{\rho UL}}{\boldsymbol{\mu}} \tag{2.7}$$

where ρ, U, L and μ denote the fluid density, the fluid velocity, the channel length, and the dynamic viscosity of fluid, respectively. Physically, *Re* represents the ratio of inertial to viscous forces within the flow. Since we use a microfluidic channel which has micro-scale dimensions (e.g. 25 μm x 25 μm, width x height), *Re* of the channel is less than 1, indicating that the system always has laminar flow. In addition, this low *Re* implies that entrance effects of flow are negligible. Within a fluidic channel having a diameter *D*, the entrance length parameter is proportional to *D* and *Re* (29). Therefore, given the micro-scale dimensions and low *Re* of our system, we can conclude that the fluid flow is stabilized immediately after entering the channel and has a parabolic velocity profile (Figure 2-3).

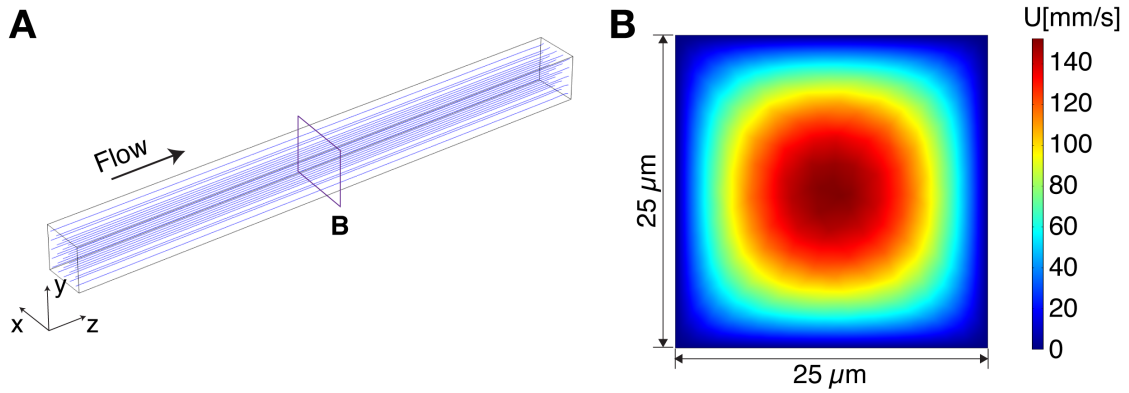

Figure 2-3. Fluidic flow in a microfluidic pore as simulated by Comsol Multiphysics. A, Stream lines (blue) of flow in a pore with micro-scale dimensions (25 μm x 25 μm, width x height). **B**, Velocity profile of a cross section (purple rectangle in A) of the pore. The flow has maximum velocity at the center of the pore and minimum velocity near the walls of the pore.

2.2 Principles of Node-Pore-Sensing (NPS)

Utilizing RPS is a robust method to quantify size and transit time of particles. However, analyzing the resulting electrical current pulse has limited temporal resolution, as only the total transit time of a particle through the pore can be deduced. To address this limitation, Balakrishnan *et al.* developed node-pore-sensing (NPS). NPS utilizes a pore that has been segmented with multiple nodes, which are characterized by a sudden expansion of the channel width (15, 16) (Figure 2-4). As a particle passes through pairs of nodes and pores, the lower current density within the nodes produces peaks in the electric current. Thus, the number of peaks correspond to the number of nodes. By analyzing the resistivity changes as a particle transits node-pores, we can measure particle size. Also, from the width of segmented current pulses, we can quantify the transit times through each segment of the pore. Compared to RPS which involves a single pore, NPS provides higher temporal resolution and also more robust Signal-to-Noise Ratio (SNR), as a unique electronic pulse, reflecting the sequence of nodes and pores, is produced.

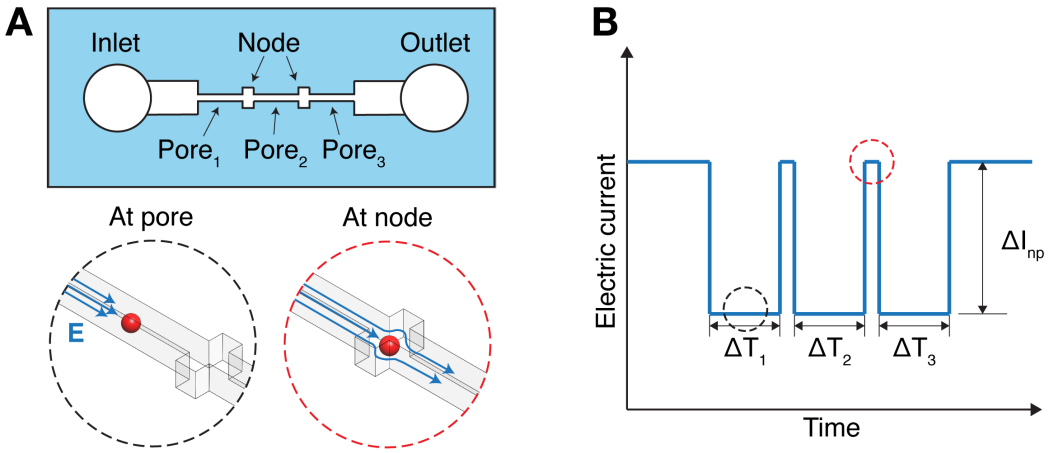

Figure 2-4. Principle of Node-Pore-Sensing (NPS). A, Schematic drawing of the NPS platform. A pore is segmented by nodes which have more current density than that in the segments (E, blue lines in bottom insets). **B**, Expected current signal produced by a particle transiting through node-pores. Dashed black and red circles indicate the current drop and increase at the pore and node, respectively, and correspond to the bottom insets of **A**. ΔI_{np} and $\Delta T_{x\,(=1,\,2,\,\text{and}\,3)}$ represent the amount of current drop at the pore and the transit time of the particle at each section of pore, respectively.

2.3 Contraction-based Mechanical Phenotyping

To characterize the mechanical properties of cells, we integrate a contraction channel into a regular NPS device (Figure 2-5A). The contraction channel is designed to have a smaller channel width than a cell diameter (D_{cell}). Thus, when cells are driven through the contraction channel, they experience compressive deformation. Strain, ε, represents the amount of deformation and is determined by D_{cell} and width (w_c) of the contraction channel (ε=(D_{cell}-

w_c)/D_{cell}). As shown Figure 2-5B, the straight contraction channel induces constant-strain deformation to cells with respect to time. Based on the amount of deformation and transit time through the contraction channel, we can quantify mechanical phenotypes. The diameter of deformed cell (D_d) indicates the amount of deformation in the direction of the channel height and length, and the transit time (ΔT_{cont}) represents the required time for the cell to pass through the contraction channel.

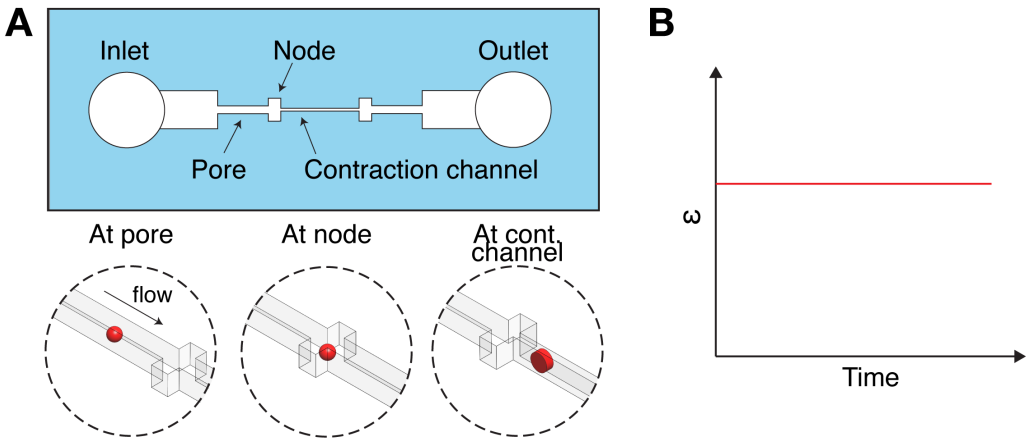

Figure 2-5. Principle of contraction-based cellular deformation. A, Schematic drawing of a microfluidic device containing a contraction channel. When a cell passes through the contraction channel, the narrow width of the channel causes compressive deformation of the cell. **B**, Expected strain (ε) curve of the cell during the deformation.

To distinguish cell populations through these measured parameters, we derived a dimensionless number, which we refer to as the whole cell deformability index (*wCDI*). We assume a functional relationship among the biophysical parameters of a cell and fluid flow as follows,

$$\boldsymbol{F\left(E, D_{cell}, h_{channel}, U_{flow}, \Delta T_{cont}, \mu, L_c\right) = 0} \tag{2.8}$$

where E, D_{cell}, $h_{channel}$, U_{flow}, U_c, μ, and L_c correspond to elastic modulus, free cell diameter, height of the microfluidic channel, flow velocity within the node segment leading to the contraction channel, the transit velocity of cells in the contraction channel, fluid viscosity, and the length of the contraction channel, respectively. Three fundamental dimensions (n=3)—mass (M), length (L), and time (T)—are included in each of these six parameters (n'=7) as follows,

$$\boldsymbol{E = \left[ML^{-1}T^{2}\right]} \tag{2.9a}$$

$$\boldsymbol{D_{cell} = [L]} \tag{2.9b}$$

$$\boldsymbol{h_{channel} = [L]} \tag{2.9c}$$

$$\boldsymbol{\Delta T_{cont} = [T]} \tag{2.9d}$$

$$\boldsymbol{U_{flow} = \left[LT^{-1}\right]} \tag{2.9e}$$

$$\boldsymbol{\mu = \left[ML^{-1}T^{-1}\right]} \tag{2.9f}$$

$$\boldsymbol{L_c = [L]} \tag{2.9g}$$

Following the Buckingham π theorem (30), the relationship among these parameters can be written in terms of a set of four dimensionless parameters (n'-n=4). To find these dimensionless parameters (π_i; i=1, 2, 3, and 4), we select repeating variables (h_{channel}, U_{flow}, and π), where the number of required variables is equal to the number of fundamental dimensions (n=3). Multiplying one of the nonrepeating variables with the product of the repeating variables, we can define the following π terms,

$$\boldsymbol{\pi_1 = \frac{h_{channel}E}{U_{flow}\mu}} \tag{2.10a}$$

$$\boldsymbol{\pi_2 = \frac{h_{channel}}{\Delta T_{cont}U_{flow}}} \tag{2.10b}$$

$$\boldsymbol{\pi_3 = \frac{D_{cell}}{h_{channel}}} \tag{2.10c}$$

$$\boldsymbol{\pi_4 = \frac{L_c}{h_{channel}}} \tag{2.10d}$$

We define the dimensionless parameter, *wCDI* (Equation (2.11)), to be the product of π_2 x π_3 x π_4. The *wCDI* could also be defined as a function of π_1, in which (π_1=f(π_2, π_3, π_4)), but the exact analytical expression can only be determined by experiment (30).

$$\boldsymbol{wCDI = \frac{L_c}{U_{flow}h_{channel}} \cdot \frac{D_{cell}}{\Delta T_{cont}}} \tag{2.11}$$

Comparing the *wCDI* with cellular cortical tension (See Chapter 4 for the detailed method) and the previously reported elastic modulus (*E*) of various cell lines (Figure 2-6), we experimentally determined that the *wCDI* is inversely related to these traditional parameters.

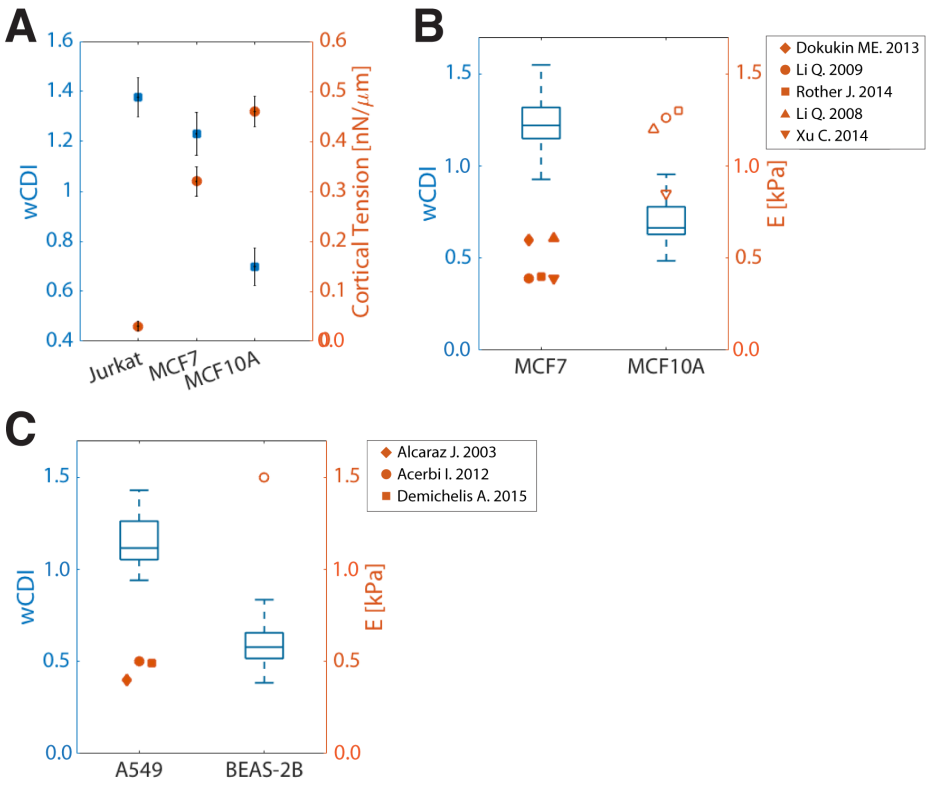

Figure 2-6. Relationship between mechanical properties and *wCDI*. **A**, Comparison of *wCDI* with cortical tension as determined by micropipette aspiration of Jurkat, MCF7, and MCF10A cells. The *wCDI* is inversely related to cortical tension. Error bar indicates standard deviation for *wCDI* and standard error for cortical tension. **B** and **C**, Comparison of *wCDI* with the elastic modulus, as measured by AFM, of breast cell lines (B) and lung cell lines (C). Within each blue box, the central line is the median and the edges of the box correspond to 25% and 75% of the *wCDI* distribution. The orange symbols are the reported elastic modulus of each cell line. The trend of *wCDI* over various cell lines is inversely proportional to the elastic modulus. *From Ref (31).*

2.4 Rheological Approach to Single Cell Mechanics

While it is a robust method to evaluate cellular mechanical behavior and to screen certain types of cells, contraction-based mechanical phenotyping provides limited biophysical information. Such information, which include elasticity, viscosity, and time-dependent mechanical

properties, could be obtained via rheological approaches (Figure 2-7). Among the various experimental methods, we employed oscillatory rheology to reveal the viscoelastic properties of cells and their time-dependent characteristics over specific frequency ranges. As will be shown in detail in Chapter 2.3, strain values correspond to the amount of cellular deformation in the contraction channel. By definition, strain (ε) is determined by the free-cell diameter (D_{cell}) and width of the contraction channel (w_c). Because w_c is periodic along the channel's longitudinal axis (Figure 2-8), so, too, ε is periodic,

$$\varepsilon = \varepsilon_0 \cos(\omega t) + \varepsilon_p \tag{2.12}$$

where ε_0, ε_p and ω denote strain amplitude, compressive pre-strain, and deformation frequency, respectively.

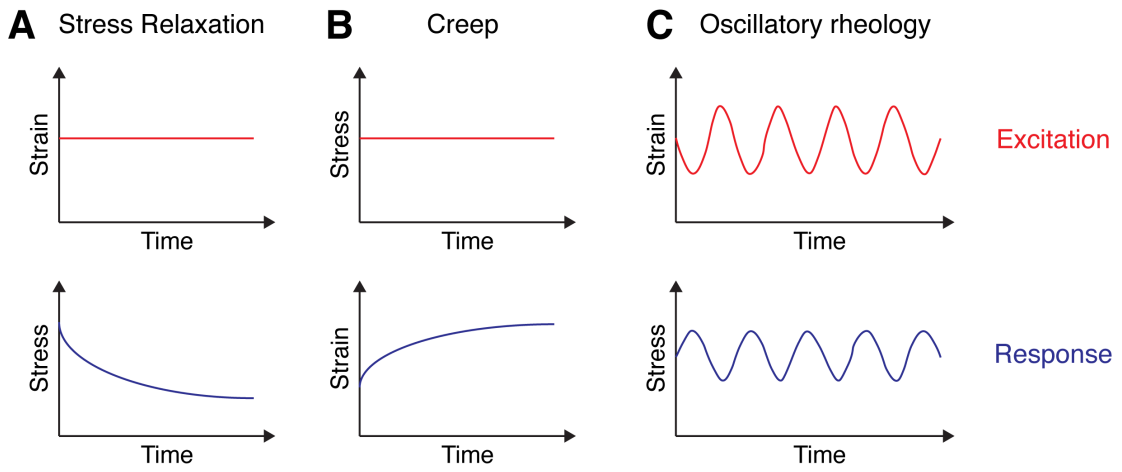

Figure 2-7. Mechanical loading conditions to measure time-dependent properties. A, Stress relaxation corresponds to applying constant strain to a material over time and monitoring stress values over time. **B**, Creep test corresponds to applying constant stress to a material over time and monitoring the change in strain. **C**, Oscillatory rheological approach corresponds to applying a sinusoidal strain excitation to a material and monitoring a cyclic stress response.

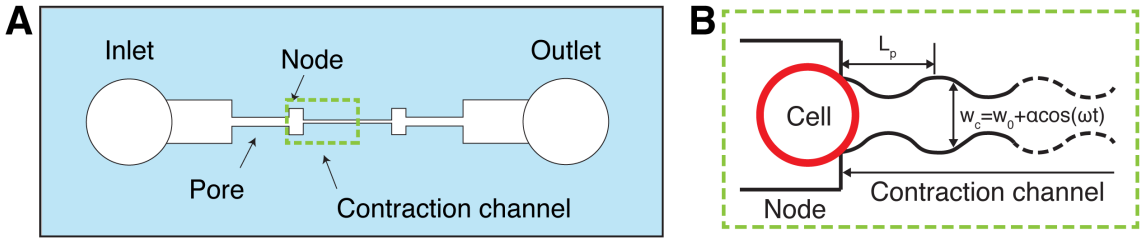

Figure 2-8. Principle of microfluidic rheology to measure the viscoelastic properties of cells. A, Schematic drawing of a microfluidic device containing a contraction channel with periodically

changing width. **B**, Enlarged drawing of the sinusoidal contraction channel (dotted green box in **A**). The width of channel (w_c) gradually changes as a cosine function ($w_0+\alpha\cos(\omega t)$). L_p, w_0, α and ω correspond to the contraction channel's periodic length, initial width, strain amplitude, and deformation frequency, respectively. *From Ref*(32).

To determine the stress value (σ) of a cell within our contraction channel, we first analyze the external forces surrounding a deformed cell. As it transits the contraction channel and deforms, a cell is subject to driving (F_{drive}) and drag forces (Figure 2-9). F_{drive} is a result of the pressure distribution around the deformed cell (Equation (2.13)). To calculate this force, we modeled (via Comsol Multiphysics) the fluid dynamics within our device and used as our parameters the specific flow rate and channel geometry we employed in our experiments. With F_{drive}, we then calculated the average pressure difference (ΔP_{avg}) across the deformed cell in the channel's longitudinal axis direction (Equation (2.13)). Frictional forces (F_{fric}) between the cell surface and channel wall (Figure 2-9), which are in the opposite direction of the flow, are defined by the frictional coefficient (μ_f) and normal force (F_n) (Equation (2.14)).

$$\boldsymbol{F_{drive} = \int \Delta P dA = \Delta P_{avg} \cdot w_c \cdot D_d} \tag{2.13}$$

$$\boldsymbol{F_{fric} = \mu_f \cdot F_n = \mu_f D_d^{\,2} \pi \sigma / 4} \tag{2.14}$$

Since a cell transits the contraction channel with constant velocity (Figure 2-10), there is a zero-net force around the deformed cell (Equation (2.15)). Substituting F_{drive} and F_{fric} into Equation (2.15), we determine σ from our fluidic conditions and the compressive deformation of cells (Equation (2.16)).

$$\boldsymbol{F_{net} = F_{drive} - 2F_{fric} = 0} \tag{2.15}$$

$$\boldsymbol{\sigma = 2\Delta P_{avg} w_c / \pi \mu_f D_d} \tag{2.16}$$

With ε (Equation (2.12)) and σ (Equation (2.16)) defined for an individual cell, we employ a rheological stress-strain relationship to quantify a cell's viscoelastic properties. This relationship is defined in Equation (2.17), where σ_p, G', and G'' indicate the pre-stress induced by ε_p, storage modulus (cell elasticity), and loss modulus (cell viscosity), respectively. Substituting Equation (2.9) (ε) and Equation (2.16) (σ) into Equation (2.17), we can subsequently numerically calculate the unknown variables, μ_f, σ_p, G', and G'', using Least Squares Fitting (see Appendix C for the detailed MATLAB code for Least Squares Fitting).

$$\boldsymbol{\sigma = \sigma_p + G'\varepsilon_0 cos(\omega t) + G"\varepsilon_0 sin(\omega t)} \tag{2.17}$$

In addition to quantifying the viscoelastic properties of a cell at any given frequency, ω, we can utilize the power-law structural damping model (33) to provide more information about a cell's dynamic behavior with respect to a wide range of frequency. The complex modulus (G^*) is defined as,

$$\boldsymbol{G^*(\omega) = G'^{(\omega)} + iG"(\omega)} \tag{2.18a}$$

$$\boldsymbol{= G_0\left[1 + itan\left(\frac{\pi}{2}\alpha\right)\right]\left(\frac{\omega}{\omega_0}\right)^{\alpha} + i\mu\omega} \tag{2.18b}$$

$$\boldsymbol{= G_0\left(\frac{\omega}{\omega_0}\right)^{\alpha} + i\left[G_0 tan\left(\frac{\pi}{2}\alpha\right)\left(\frac{\omega}{\omega_0}\right)^{\alpha} + \mu\omega\right]} \tag{2.18c}$$

where G_0, α, and μ denote shear modulus at zero frequency, power-law exponent, and viscosity, respectively. G_0 and ω_0 are scaling factors for stiffness and frequency, and ω_0 =1 Hz in our experiments. All power-law components are numerically calculated by Least Squares Fitting. Although the spring-dashpot models such as Maxwell, Kelvin, Standard Linear Solid model (34) (Figure 2-11) have been widely used to analyze mechanical behavior, these models generally overestimate a material's frequency dependence. This is because spring-dashpot models employ the combination of discrete elements to describe the stress-strain relationship, which is continuous in the time domain (35, 36). In contrast, the power-law structural damping model provides a higher and more appropriate sensitivity to detect the frequency dependence of cellular viscoelastic properties at the single-cell level.

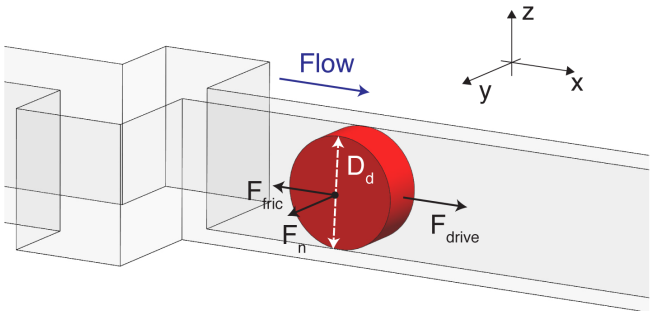

Figure 2-9. Schematic drawing of the forces around the deformed cell while in the contraction channel. F_{drive}, F_n, F_{fric}, and D_d correspond to the driving force, normal force, frictional force, and the diameter of the deformed cell, respectively. Under a cell's constant velocity, the driving force generated

by the pressure difference around the cell is counter-balanced by the frictional forces between cell surface and the channel wall. *From Ref(32).*

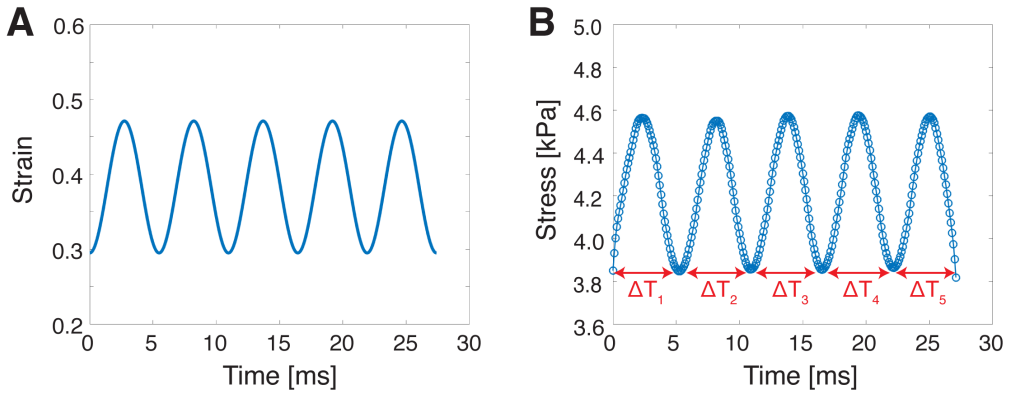

Figure 2-10. Stress-Strain of an MCF7 cell measured by visco-NPS. A, Applied strain and **B**, stress of an MCF-7 cell transiting the contraction channel with L_p=500 μm and v_{pore}=65 mm/s. $\Delta T_{n=1,2,\ldots,5}$ represent the period of each cycle of oscillating stress. During the cell's transit through the channel, $\Delta T_{n=1,2,\ldots,5}$ represent the period of stress ($\overline{\Delta T_n} = 5.5 \pm 0.17$ [ms]) it experiences. The constant period of stress indicates that the cell transits the contraction channel with constant velocity. *From Ref*(32).

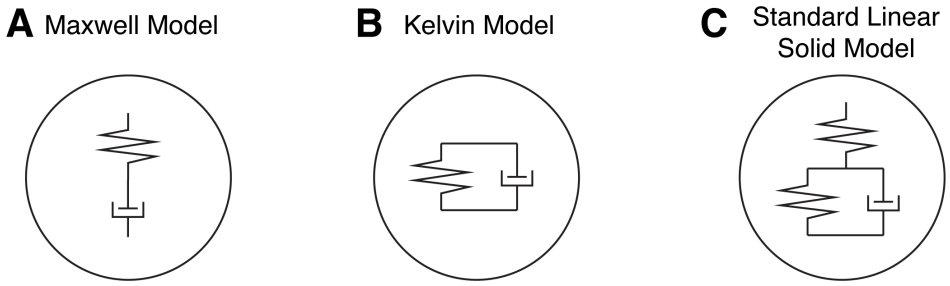

Figure 2-11. Spring-dashpot models. A, Maxwell model involves having a spring and a dashpot in series. B, Kelvin model involves placing the spring and dashpot in parallel. C, Standard Linear Solid (SLS) model involves two springs and one dashpot connected in series and parallel. In all these models, the spring and dashpot represent the elasticity and viscosity of a material, respectively.

2.5 Conclusion

As discussed in this chapter, RPS and NPS provide a unique and robust means to measure cell size and transit time. By including a contraction channel and performing the same measurements, these techniques can quantify the mechanical phenotypes of cells at the single-cell level. By including a contraction channel whose width periodically changes, one can achieve a rheological approach and measure the viscoelastic properties of individual cells. In

the following chapter, I will describe the detailed fabrication procedure to create the microfluidic devices that are used for the experiments detailed throughout this thesis.

3 DEVICE FABRICATION AND MEASUREMENT

Chapter Overview

This chapter describes the device manufacturing protocol and experimental set up for the mechano-NPS and visco-NPS measurements described throughout this thesis.

3.1 Device Fabrication

The manufacturing of the microfluidic devices used in this thesis includes electrode- and polydimethylsiloxane (PDMS) mold-fabrication (Figure 3-1). The electrodes are created on a glass substrate through electron-gun (e-gun) metal deposition. Soft-lithography is employed to make PDMS molds of the various microfluidic channels. Once bonding between these two is achieved, device fabrication is complete.

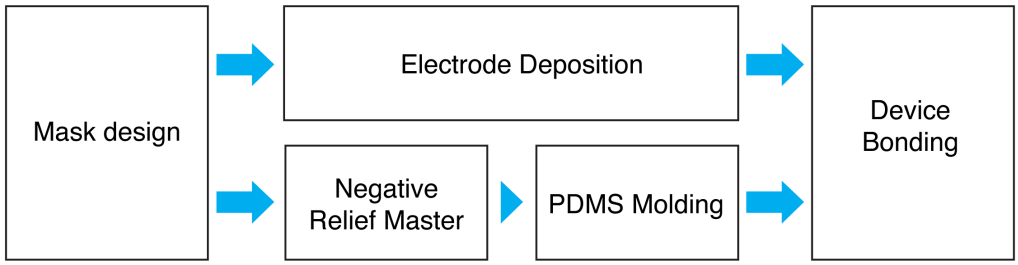

Figure 3-1. Fabrication workflow for the microfluidic devices used in this thesis.

3.1.1 Electrodes

We fabricate metal electrodes and contact pads onto a glass substrate to measure the change in electric current across the microfluidic channel. As shown in Figure 3-2, standard photolithography with positive photoresist (S1813, MicroChem, USA) is used to pattern the glass substrates. We spin-coat the positive photoresist (PR) onto a pre-cleaned glass slide (VWR, USA) at 3000 rpm for 30 seconds to achieve a height of 1.5 μm. We next soft bake the resist-coated slide at 100°C on a hotplate for 1 minute. Following baking, we then expose the slide to UV light under a transparency mask for 27 seconds at 275W, and subsequently develop using MF321 (MicroChem, USA) developer for 15 seconds. After the development process, we wash the glass slides with deionized (DI) water and dry with nitrogen gas. We next use e-gun evaporation to deposit a 100/250/250 Å layer of Titanium (Ti)/Platinum (Pt)/Gold (Au). We subsequently perform a lift-off step in acetone to remove the excess metal. We use a gold wet etchant (Gold Etchant TFA, Transene Company, USA) to expose the Pt electrodes. The contact pads remain gold-coated.

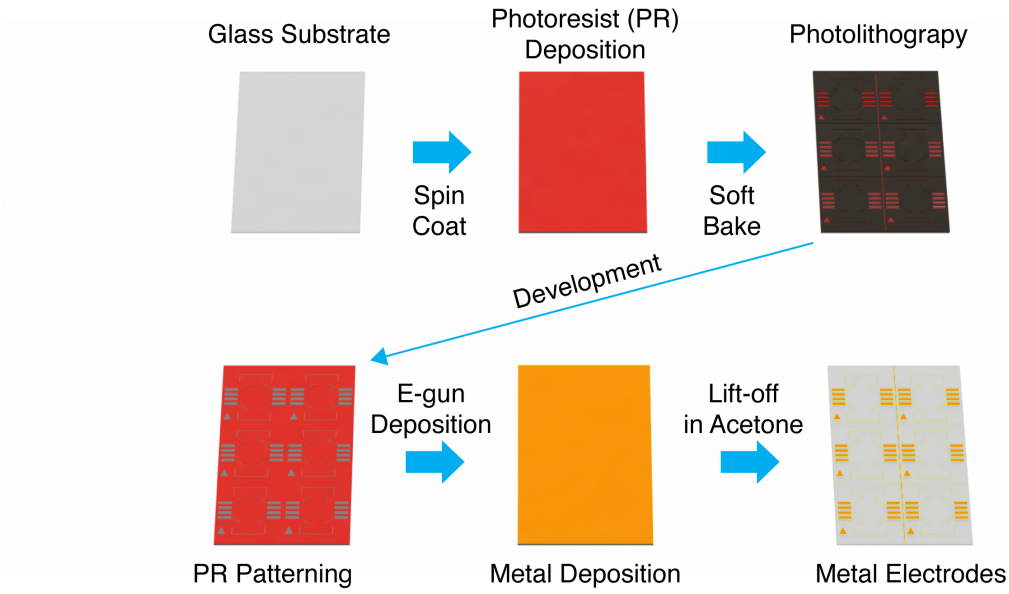

Figure 3-2. Electrode fabrication processes. Schematic of the 6 steps for electrode fabrication. Standard photolithography is used to pattern positive PR onto glass substrates. E-gun deposition is employed to deposit multiple layers of metal on the pre-patterned glass substrates. By removing excess metal with an acetone lift-off, we complete the fabrication of the electrodes.

3.1.2 PDMS Mold

We employ standard soft-lithography to fabricate the PDMS molds for our microfluidic devices. To make negative-relief masters, we pattern SU-8 3025 resist (MicroChem, USA) onto a silicon wafer (Figure 3-3). First, we spin a resist layer at 4000 rpm for 30 seconds to produce a 22 μm thick layer. Next, we soft-bake the wafer at 95°C on a hotplate for 10 minutes. To pattern, we expose the wafer to UV light (275W) for 36 seconds with a transparency mask that has the specific channel design. We post-exposure bake the wafer at 65°C on a hotplate for 1 minute and then 95°C for 5 minutes. After cooling the wafer to room temperature, we developed the wafer in SU-8 Developer (MicroChem, USA) for 3 minutes. We then rinse the wafer with isopropanol, acetone, and DI water, and subsequently anneal at 150°C on a hotplate for one hour in order to prevent cracking of the patterned negative-relief master.

Using the fabricated negative-relief master, we mold the microfluidic channel with PDMS. We poured a mixture of PDMS (1:9 weight ratio of elastomer to curing agent, Dow Corning, USA) onto the masters and subsequently cured at 85°C on a hotplate for 2 hours. Once cured, we cut and excise from the master a slab of PDMS with the embedded

microfluidic channel. In addition, we core inlet and outlet holes using a 1-mm biopsy punch (Integra LifeSciences, USA).

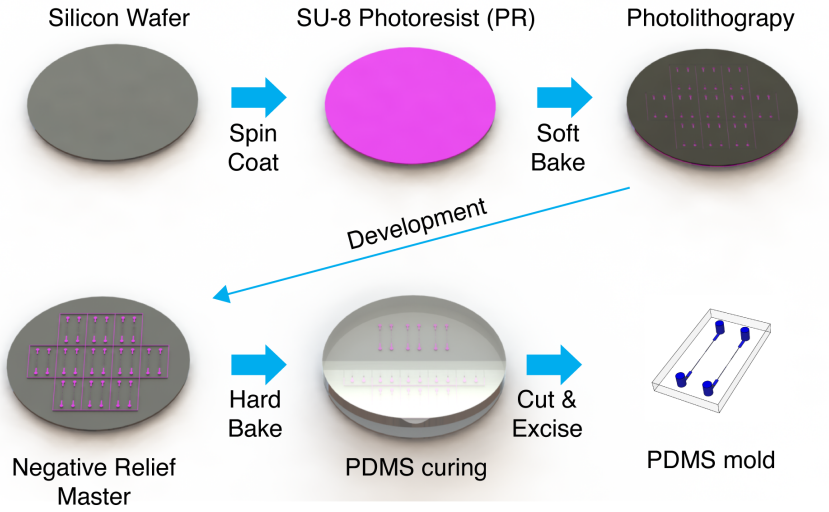

Figure 3-3. Fabrication procedure for creating the negative-relief master and PDMS devices.

3.1.3 Device Bonding

To complete the device, we expose both the PDMS mold and the glass substrate with oxygen plasma (470 mTorr, 80W, 1min). After exposure, we deposit 20 µL of a 2:1 methanol: DI water mixture onto the glass substrate. We next align the PDMS mold on top of the glass substrate (Figure 3-4), and subsequently heat the devices at 85°C on a hotplate for 2 hours to create a permanent bond.

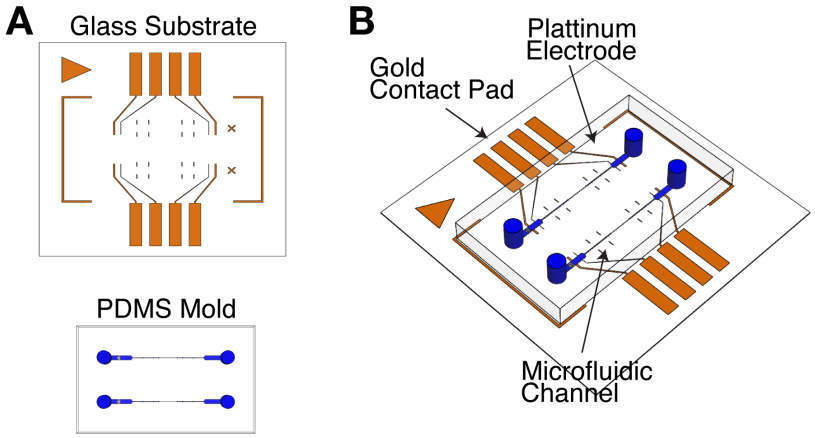

Figure 3-4. Schematic of device bonding. A, Schematic of the glass substrate with patterned electrodes and the PDMS mold containing microfluidic channels. **B**, The glass substrate and PDMS mold are aligned using multiple alignment markers.

3.2 Platform Set Up

3.2.1 Data Acquisition

Figure 3-5 shows the experimental set up, including the electrical circuit model, to measure the completed microfluidic device. To flow a suspension of cells through the channel, a commercial microfluidic flow control system (OB1 MK3, Elveflow) applies a non-pulsatile pressure within the range of 13.8~27.6 kPa to the inlet reservoir of the channel. As shown in Figure 3-5, the electrical circuit model is based on a four-point measurement with 1V of applied DC voltage (29). In the circuit, R_c and C_c are the resistance and capacitance of the microfluidic channel, respectively. R_H and R_L represent the resistance of the fluid in the inlet and outlet reservoir. The two different operational amplifiers, INA100 and OP27, are employed as a summing amplifier and integrator, respectively. In this circuit, the electric current flows from I_H, through I_L, to I_{out}. R_f and C_f represent the feedback circuit elements of the integrator. The electrical current passes through a current preamplifier (DL Instruments 1211) that converts into a voltage signal before the measurement is sent to a DAQ Board (National Instruments PCI-6035E) for data sampling and subsequent recording via LabVIEW software.

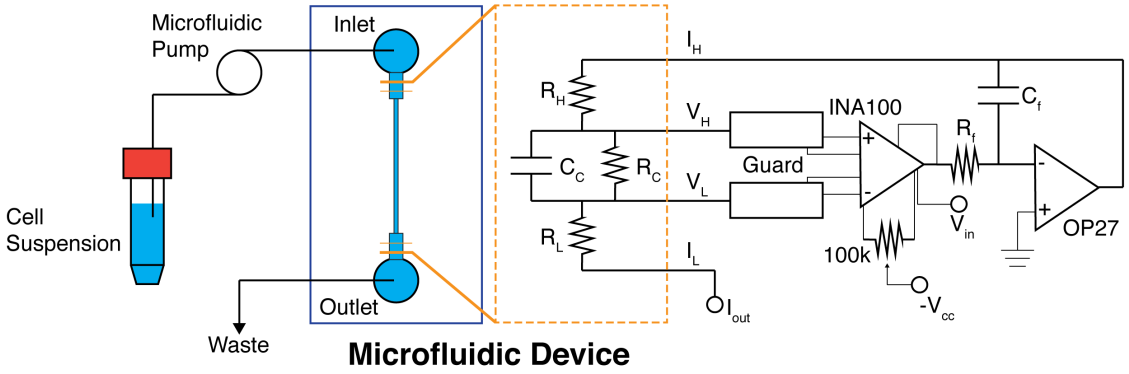

Figure 3-5. Experimental Set up for mechanical phenotyping and viscoelastic cell measurements. The fluidic set up is shown on the left. A schematic drawing on the right shows the electrical circuit model. The orange dashed box indicates the equivalent circuit elements of the fluid in the reservoir and microfluidic channel. The output current passes into a current amplifier, then into a DAQ board, and finally recorded by LabVIEW software.

3.2.2 Data Analysis

To measure the width and height of individual current pulses, we employ multiple signal processing steps via customized MATLAB code (Figure 3-6) (a full description of the MATLAB code can be found in Appendices A and B). As a first step, we remove electrical noise from the acquired signal using low-pass filtering. We normalize the slope of the base-line current in order to remove any drift. We subsequently use a derivative cut-off detection to identify the start and end points of individual pulses in the time domain. Based on these time points, we determine the width and height of the pulses.

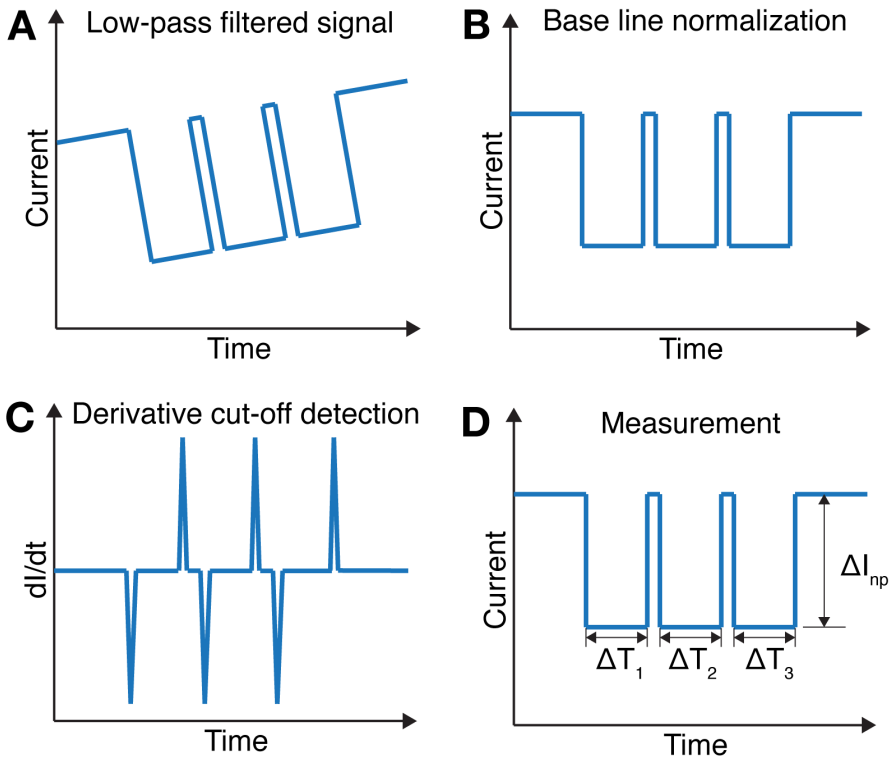

Figure 3-6. Signal processing for data analysis. The acquired signal is first **A**, low-pass filtered to remove noise, and then, **B**, the inclined base-line current is normalized. **C**, A derivative cut-off detection is subsequently employed to determine the start and end point of each pulse. **D**, the current pulse magnitude (ΔI_{np}) and duration (ΔT_1, ΔT_2, and ΔT_3) are measured based on the identified start and end time point.

3.3 Conclusion

In this chapter, we describe the fabrication steps required to make the microfluidic devices used in this thesis. These steps include photolithography and thin-metal deposition to create electrodes, negative relief masters and soft lithography to create PDMS molds of the microfluidic channels; and thermal bonding to complete the devices. To quantify the current pulses caused by the cells transiting the microfluidic channel, we employ a four-terminal measurement of the current. For data analysis, we develop and optimize the signal processing steps to measure the current-pulse magnitude and duration.

4 MULTI-VARIABLE MECHANICAL PHENOTYPING

Chapter Overview

This chapter introduces an electronic-based microfluidic platform—mechano-NPS—to determine the mechanical phenotypes of cells at the single-cell level. Mechanical phenotyping via this platform is shown to differentiate among cell types and malignant vs non-malignant cells.

4.1 Introduction

Cells derive their mechanical properties from the structure and dynamics of their intracellular components, including the cytoskeleton, cell membrane, nucleus, and other organelles—all of which, in turn, emerge from cell type-specific genetic, epigenetic, and biochemical processes. The ability to identify differences within a population of one cell type or different cells among heterogeneous populations, or to detect changes due to disease or environmental interactions all based on cellular mechanical properties has potentially important implications for cell and tissue biology and clinical metrics. As examples, metastatic potential (37, 38), cell-cycle (39, 40), differentiation state (7, 41-45), the outcome of tissue self-organization (46), and infection with intracellular pathogens (47, 48) have all been shown to correlate with changes in cellular mechanics. Even the process of aging has been shown to affect the ability of cells within the vascular system and musculoskeletal system to recover from mechanical deformation (49). Thus, methods to measure multiple cellular mechanical properties rapidly and accurately have tremendous potential as label-free research tools and diagnostics.

Atomic-force microscopy (AFM) (1, 3, 50) and micropipette aspiration (4, 51) are the gold standard for performing mechanical measurements on cells. These methods provide controlled loading conditions (e.g. stress relaxation and creep indentation) and quantify such cellular properties as elastic modulus and cortical tension. They are, however, burdened by slow throughput, capable of analyzing only just a few cells/hr (6, 7), although recent adaptations of both methods have demonstrated higher throughput via more efficient analysis (52, 53). Likewise, optical tweezers (54, 55) and microplate rheometery (10)—two other well-established methods to measure cellular mechanical properties—also suffer from low throughput. Given these drawbacks, a number of microfluidic platforms have consequently been developed, including hydrodynamic stretching cytometry (11, 56, 57), suspended

microchannel resonators (SMR) (12), and real-time deformability cytometry (RT-DC) (13), to name only a few. Each of these methods, through optical imaging or measuring changes in resonant frequencies, can analyze populations of cells in a relatively short time (e.g. 2,000~65,000 cells/s for hydrodynamic stretching cytometry (11, 56, 57), 30 cells/s for SMR (12), and 100 cells/s for RT-DC (13)). To identify specific cell types, these methods most often focus on correlating cell size or mass with a specific mechanical property. For example, hydrodynamic stretching cytometry and RT-DC compare cellular deformability with cell size, and SMR determines the transit time of cells through a narrow channel with respect to cell mass. Populations of cells are complex with respect to the continua of cell states that are represented within, and as such, multiple biophysical parameters are necessary to deconvolve and identify complex cellular mixtures.

Recently, Masaeli *et al.* and Lin *et al.* (58, 59) have reported using deformability cytometry to measure multiple parameters, such as cell size, morphology, and relaxation rate, while cells undergo deformation. In so doing, they were able to identify different cellular states associated with pluripotent and neural stem-cell differentiation, respectively. While this achievement emphasizes the need for measuring multiple biophysical parameters to identify specific cell types, Masaeli *et al.* and Lin *et al.* (58, 59) focus on defining cellular phenotypes only while cells undergo deformation. Since overall recovery of a cell once released from deformation plays significant roles in cellular migration processes such as cancer metastasis (60) and in providing a protective mechanism of cells against mechanical damage (61-63), it is imperative for mechano-phenotyping platforms to have a *temporal window* sufficient enough to analyze the recovery that a cell undergoes after deformation.

Here, we describe in detail mechano-NPS. As we introduced in Chapter 2, mechano-NPS involves integrating a node-pore sensor (15, 16) with a contraction channel and performing a four-terminal measurement of the current across the integrated microfluidic channel to quantify four biophysical properties of a single cell, *simultaneously*: diameter, resistance to compressive deformation, transverse deformation, and recovery from deformation. This *electronic-based* method of multi-dimensional mechanical phenotyping provides the means to use these biophysical parameters as label-free biomarkers for identification and differentiation among cell types. Mechano-NPS distinguishes malignant from non-malignant immortal epithelial cells and measures deformability changes in the cytoskeleton. With these findings, mechano-NPS represents an efficient, simple, and direct means to quantify multiple mechanical properties of single cells in heterogeneous populations.

4.2 Experimental Methods

4.2.1 Platform Design

The platform consists of a 30 μm-high microfluidic channel embedded in a PDMS mold bonded to a glass substrate with pre-defined Pt electrodes and gold contact pads (Figure 4-1,

see Chapter 2 for fabrication details). The central part of the channel, which we refer to as the "contraction channel", is long (2055 μm) and narrow (10 or 12 μm-wide) and flanked on either side by a series of nodes and pores that are 85 μm and 25 μm wide, respectively (Figure 4-1, inset). The length of the contraction channel was chosen to provide sufficient time (~30ms) over which a cell experiences constant applied strain. The node and pore dimensions were chosen for sufficient signal-to noise ratios. Given the flexibility and ease of device design and fabrication, different contraction channel lengths and node and pore dimensions could be employed. Filters that are 25 μm in width (the width was based on the size range of cells measured in these studies, ~15-20 μm in diameter) are included at the entrance of the microfluidic channel in order to remove cellular clusters that may otherwise clog the device. Applying a constant DC voltage (1V) across the channel, we employ a four-terminal measurement technique (15, 16, 29) (See Chapter 2 for detailed description) to measure the current pulses caused by cells transiting across the microfluidic channel when a non-pulsatile pressure of ~21 kPa (OB1 MK3, Elveflow) is utilized. After low-pass filtering all current versus time data, we employ custom-written software (See Chapter 2 and Appendices A and B) to extract both the magnitude and duration of each current sub-pulse (ΔI_{np}, ΔI_c, ΔT_{cont}, and ΔT_r in Figure 4-2).

Power analysis was employed to ensure that our sample size for mechanical phenotyping offers adequate power (≥0.80) to detect differences between experimental groups within a 95% confidence interval (64) from the measured data set. For all cases which have a p–value < 0.05, the analyzed sample size (N_a) provided sufficient power value to measure statistical differences (Table 4-1). Statistical significance was determined by performing a paired t-test or chi-square test. To ensure repeatability of results, all data presented in this study were measured using multiple microfluidic devices. The *wCDI* of MCF-7 cells (see Chapter 2 for a detailed analysis of the *wCDI*) obtained with different device replicas showed no statistical difference (Figure 4-3, p=0.173).

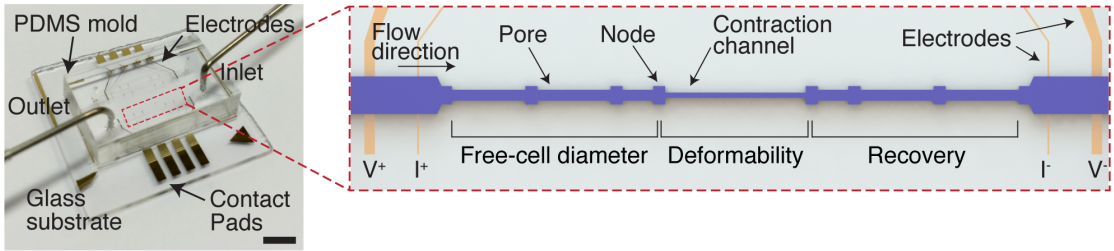

Figure 4-1. A schematic image of the microfluidic platform. Red-dashed box shows a close-up view of the entire microfluidic channel. The microfluidic channel (pore) is segmented by nodes and a contraction channel. Two electrodes at both ends of the channel apply a constant voltage (1V), and two inner electrodes measure the change of current across the channel. The regions where free-cell diameter, deformed diameter, and cell recovery are measured are as indicated. The scale bar corresponds to 4 mm**.** *From Ref (31).*

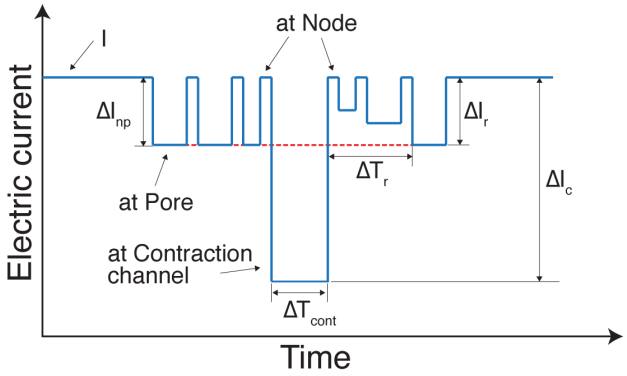

Figure 4-2. Expected current pulse generated by a cell transiting the microfluidic channel. I, ΔI_{np}, ΔI_c, and ΔI_r correspond to the baseline current and the current drop by a cell transiting a node-pore, a contraction channel, and a node-pore after the contraction channel, respectively. ΔT_{cont} corresponds to the time duration of a cell passing through the contraction channel, and ΔT_r indicates the time needed for ΔI_r to equal ΔI_{np}. *From Ref (31).*

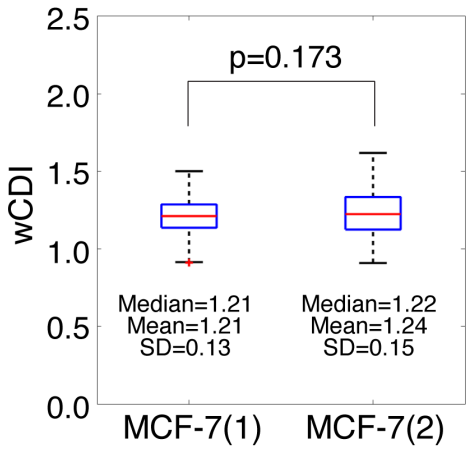

Figure 4-3. *wCDI* of MCF7 cells from different replicas of the mechano-NPS device. MCF7 cells were measured by different replica of the device showing no statistical difference (MCF-7(1): n=97, MCF-7(2): n=99, p=0.173). The statistical difference was determined by a paired t-test. Within each blue box, the central line is the median and the edges of the box correspond to 25% and 75% of the *wCDI* distribution. *From Ref (31).*

Table 4-1. Power analysis of experimental groups based on sample size. To ensure adequate power to detect differences within experimental groups, we measured the power of each group using 2-sample and 1-slided power analysis with 95% confidence interval. The analysed sample size, N_a, provided the

adequate power value (≥0.80) throughout the all experimental cases. In this table, N.A indicates power analysis is not applicable due to the high *p*-value ($p \geq 0.05$). *From Ref (31).*

Cell type	**MCF10A**	**MCF7**	**A549**	**BEAS-2B**	**MCF7_PDL**	**MCF7_BSA**
N_a	99	99	100	100	99	99
power	1	1	1	1	0.96	0.83
Cell type	**MCF7_LatA**	**MCF7_LatB**	**MCF10A_LatA**	**MCF10A_LatB**	**MEP**	**LEP**
N_a	99	99	99	99	99	104
power	0.86	0.81	0.99	N.A.	1	1
Cell type	**240L**	**240L-p16sh**	**240Lp16sMY**	**240L-D1**	**240LD1MY**	
N_a	54	54	54	54	54	
power	0.87	N.A.	0.99	0.98	0.87	
Cell type	**122L**	**122L-p16sh**	**122Lp16sMY**	**122L-D1**	**122LD1MY**	
N_a	54	54	54	54	54	
power	1	0.83	N.A.	0.80	0.84	

4.2.2 Cell Culture and Preparation

MCF-10A cells (ATCC® CRL-10317™) were cultured in MEBM medium, supplemented with 0.1% insulin, 0.1% hEGF, 0.4% hydrocortisone, and 10% cholera toxin. MCF-7 cells (ATCC® HTB-22™) were cultured in DMEM (Fisher Scientific, BW12719F), supplemented with 10% fetal bovine serum (FBS), 0.1 mM MEM Non-Essential Amino Acids (NEAA), 2 mM L-glutamine, and 1% Pen-Strep. BEAS-2B cells (ATCC® CRL-9609™) were cultured in BEGM BulletKit (Lonza, CC-3170). A549 cells (ATCC® CRM-CCL-185™) were cultured in F-12K medium (Fisher Scientific, MT10025CV), supplemented with 10% FBS and 1% of Pen-Strep. Jurkat cells (ATCC® TIB-152™) were cultured in RPMI 1640 medium (Thermo Scientific, 88421), supplemented with 10% fetal bovine serum (FBS), and 1% Pen-Strep. All cell cultures were maintained at 37°C in 5% CO2 and routinely passaged, per published protocols (65), once they reached 80% confluence.

Cells were dissociated by treatment with 0.25% trypsin/EDTA for either 3 min (MCF-7 and A549 cells) or 5 min (MCF-10A and BEAS-2B cells) at 37°C (66-68), washed with the respective growth media, centrifuged at 0.2 RCF, and re-suspended at a concentration of ~20,000 cells/mL in PBS. To ensure cell viability, cells were injected into the prepared devices for screening immediately following re-suspension.

4.2.3 Pharmacological Inhibition of Cytoskeletal Components

We disrupted actin polymerization with Latrunculin A and B (LatA and LatB, Enzo Life Sciences) (69). Prior to deformability measurements, MCF-7 and MCF-10A cells were incubated with 2.5 or 5μg/mL LatA or LatB in each cell's respective growth medium for one hour at 37°C and 5% CO_2 (70, 71). Cells were then released from culture flasks with 0.25%

trypsin/EDTA, rinsed once with PBS, centrifuged at 0.2 RCF, and re-suspended in PBS at a concentration of ~100,000 cells⁄mL. To confirm that actin polymerization was successfully inhibited after incubation, cells were fixed by 4% (w/v) paraformaldehyde in PBS for 15 min. They were then permeabilized with 0.1% Triton-X 100 (Sigma-Aldrich) in PBS for 5 min. Cell nuclei and F-actin were then counter-stained with 4',6-diamidino-2-phenylindole (DAPI, Sigma-Aldrich, 10236276001) and rhodamine phalloidin (Thermo Fisher Scientific, R415), respectively, per manufacturer's protocol, and then imaged with a Zeiss LSM710 confocal microscope.

4.2.4 Cortical Tension Measurement Through Micropipette Aspiration

Dr. Vasudha Srivastava (University of California San Francisco) performed cortical tension measurements via micropipette aspiration, as described previously (72, 73). Briefly, cells were trypsinized and resuspended in growth medium, and were transferred to the imaging chamber. Suction pressures in the range of 0.03 to 0.3 kPa were applied to the cells through an 8-10 μm glass micropipette. At each pressure, the cellular deformation inside the pipette was allowed to stabilize for 20-30 seconds before imaging. The average measurement from three images was used to calculate the length of deformation (L_p). Subsequently, applied pressure was increased in 0.03 kPa increments till the L_p exceeded the radius of the pipette (R_p). Any cell that blebbed was discarded. The critical pressure (P_{crit}) is defined as the pressure at which the deformation inside the pipette is hemispherical, i.e. L_p=R_p. The cortical tension (T_{eff}) was then calculated using the following equation, where R_c is radius of cell.

$$\Delta \boldsymbol{P_{crit}} = \boldsymbol{2T_{eff}} \times \left(\frac{\boldsymbol{1}}{\boldsymbol{R_p}} - \frac{\boldsymbol{1}}{\boldsymbol{R_c}} \right) \tag{4.1}$$

4.3 Results

4.3.1 Population Characterization Based on Mechanical Phenotypes

The repeated expansion and contraction of the width of our overall microfluidic channel shown in Figure 4-1 produces a unique and symmetric current pulse, consisting of sub-pulses, for each cell that transits the channel. Upon entering the microfluidic channel, a cell partially blocks the flow of current, and consequently, the measured current immediately drops from a baseline value, I (Figure 4-2). When the cell enters the first node, the current returns to baseline only to drop again once the cell exits that node. This is a hallmark of NPS (See Chapter 2) (15, 16). The rise and fall of current repeats as the cell enter and exists the next two nodes. Upon entering the contraction channel where the width is narrower than the diameter of the cell, the cell deforms as shown in Figure 4-5. Because the cell blocks nearly all of the current flow in this part of the channel, the current drop from baseline is far more dramatic than that resulting from the cell transiting the earlier pores (Figure 4-6). The cell subsequently enters and exits a

series of node-pore pairs following the contraction channel, ultimately leading to the symmetrical shape of the overall current pulse. This symmetry is intentional by design and critically allows the monitoring of a cell's recovery from constant strain deformation.

The magnitude of the current sub-pulse produced in the node-pore sequence (ΔI_{np}) and the contraction channel (ΔI_c) corresponds to the free-cell diameter (D_{cell}) and cell elongation length (L_{deform}), respectively (Figure 4-5B). As described in Chapter 2, the relationship among the current drop (ΔI), baseline current (I), particle diameter (d), the overall channel length (L) and the channel's effective diameter (D_e) is defined by (15, 16, 29) Equation (2.6).

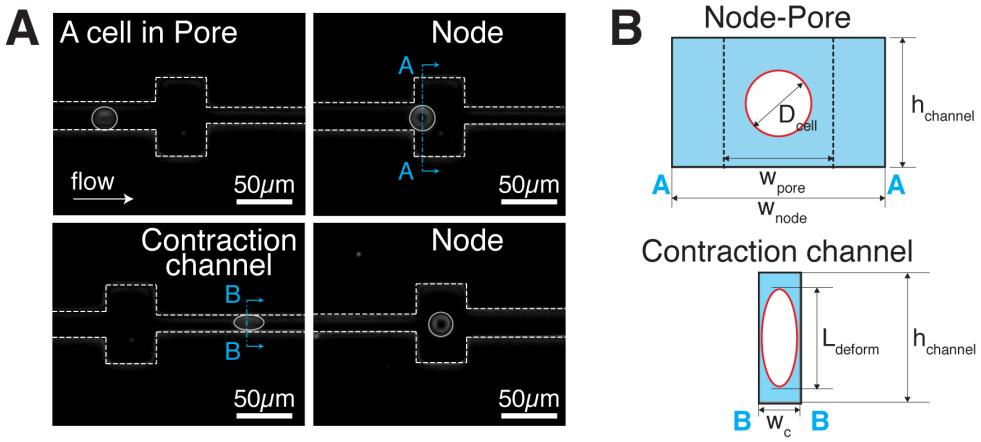

Figure 4-4. Cellular deformation within the microfluidic channel. A, Time-snapshots of an MCF-7 cell (bordered by a white circle) in each of the different segments of the microfluidic channel (white dashed line) **B**, Cross-sectional diagram of the channel segments occupied by a cell. 'AA' and 'BB' indicate the corresponding cross-sections in A. w_{pore}, w_{node}, w_c, and $h_{channel}$ correspond to the widths of the pore, node, and the contraction channel, and the height of the channel, respectively. D_{cell} and L_{deform} correspond to the free-cell diameter in the node-pore channel and the elongated length of the deformed cell in the contraction channel, respectively. *From Ref (31).*

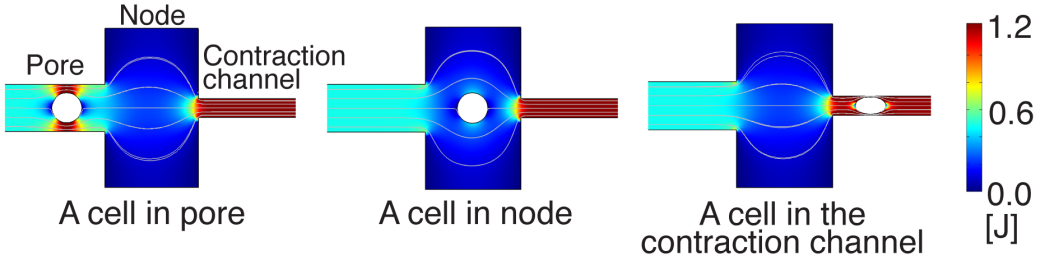

Figure 4-5. Computational modelling of the electric field when a cell transits each section of the mechano-NPS microfluidic channel. The fine lines correspond to the calculated electric-field lines in each section of the microfluidic channel, and the white circle corresponds to a cell. As

determined, the electric-field density, J, in the contraction channel is greater than that in the node. Computational simulation was performed using Comsol Multiphysics 5.0. *From Ref (31).*

To determine D_e, we measure polystyrene microspheres of known size with the microfluidic channel (Table 4-2). Using the values of $\Delta I/I$ arising from the microspheres, along with the known values of L and d (the size of the microspheres in this instance), we can numerically solve for D_e in Equation (2.6). Once D_e is known, we can subsequently determine D_{cell} of a screened cell by numerically solving for d in Equation (2.6) using the obtained values of $\Delta I_{np}/I$. We can also determine the volume of the deformed cell, V_{deform}, by the relationship (15, 16, 29), $\Delta I_c/I \sim V_{deform}/V_{contraction}$, where $V_{contraction}$ is the volume of the contraction channel. To calculate L_{deform}, we assume the cell undergoes an isometric deformation in the direction of both the channel's longitudinal axis and channel height, resulting in an oblate-spheroid shape. From the relationship between the volume and major radius of the oblate spheroid, $V_{deform} = \pi w_c {L_{deform}}^2/6$ where w_c is the contraction-channel width, we can determine L_{deform} from $\Delta I_c/I$. We quantify the transverse deformation of the cell, $\delta_{deform} = L_{deform}/D_{cell}$, as it transits the contraction channel.

Table 4-2. Measuring the channel effective diameter using polystyrene microspheres. Polystyrene microspheres (Polysciences, #64155) suspended in PBS were measured with our NPS platform to determine the node-pore channel's effective diameter, D_{e_np} (n=30) and the effective diameter of the contraction channel D_{e_cont} (n=12). d_{avg}, Δd, $\Delta I/I$, L, and σ_e correspond to the average diameter of the microspheres, the diameter standard deviation, the ratio of the current drop to baseline current, the channel length, and the effective diameter standard deviation, respectively. *From Ref (31).*

d_{avg} [μm]	σ_d [μm]	$\Delta I/I$	L [μm]	D_{e_np} [μm]	D_{e_cont} [μm]	σ_e [μm]
14.73	1.36	3.07×10^{-4}	8230	36.2	-	0.594
6.30	0.71	2.98×10^{-4}	2055	-	22.9	0.253

As a cell traverses through each section of the channel, the duration of the resulting sub-pulse produced by a cell corresponds to the cell's transit time (ΔT) through that part of the channel. To quantify the resistance to compressive deformation, we utilize ΔT_{cont}. To determine the recovery time of a cell from compressive deformation (ΔT_r), we note the time required for the sub-pulses produced by the cell after exiting the contraction channel to return to the same shape and magnitude as those produced by the cell prior to entering the contraction channel, i.e. when the cell returns to its original size and shape (Figure 4-6). Given the number of node-pore pairs and the overall length of the node-pore sequence we employ after the contraction channel, our device's temporal window for measuring cell recovery is 40 ms. The flexibility of our device design and ease of fabrication allow for the inclusion of many more node-pore pairs after the contraction channel, which in turn would lead to an increase in time over which to observe recovery. Based on all the recovery times we recorded with our particular device, we discriminate among three different cell-

recovery types—instant ($\Delta T_r \sim 0$ ms), transient ($0 < \Delta T_r \leq 40$ ms), and prolonged ($\Delta T_r > 40$ ms) (Figure 4-6).

Thus, from just a single current pulse produced by a cell transiting through the entire microfluidic channel, four biophysical properties of that cell—size (D_{cell}), resistance to compressive deformation (ΔT_{cont}), transverse deformation (δ_{deform}), and recovery from deformation (ΔT_r)—are extracted. These parameters are what we collectively use to mechanically phenotype a single cell, distinguish among cell types in a heterogeneous population, and determine subtle cellular changes.

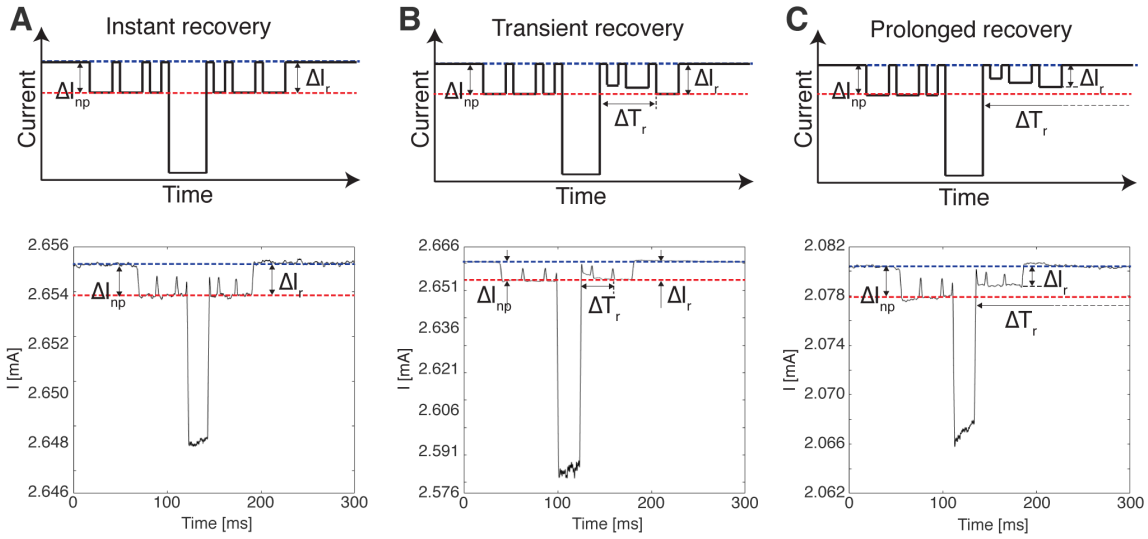

Figure 4-6. Schematic and representative mechano-sensing current pulses to illustrate the defined cellular recovery types after compressive deformation. A, Instant recovery. **B**, Transient recovery. **C**, Prolonged recovery. All schematic drawings (A, B, and C, top) show the idealized mechano-NPS current pulse. The representative current pulses (A, B, and C, bottom) show that the current at the "node" does not reach to the baseline current and has a more peak-like shape. This is due to the fast flow rate of the cells and the short length of the "node" segment. *From Ref (31).*

4.3.2 Cellular Malignancy and Mechanical Phenotyping

We investigated whether mechano-NPS could distinguish between immortal malignant and non-malignant states in two different epithelial-tissue types based on their mechanical properties alone. We compared the mechanical properties of malignant MCF-7 with non-malignant MCF-10A breast epithelial cells and malignant A549 with non-malignant BEAS-2B lung epithelial cells when individual cells were subjected to a constant applied strain along the length of the contraction channel they traversed. Because strain, ε, is a function of both cell size and contraction channel width (w_c), $\varepsilon \approx (D_{cell} - w_c)/D_{cell}$, and prior independent measurement of D_{cell} showed that malignant MCF-7 and A549 cells are, on average, larger than non-malignant

MCF-10A and BEAS-2B cells (Table 4-3), we utilized a 12 μm-wide contraction channel to measure MCF-7 and A549 cells and a 10 μm-wide contraction channel to measure MCF-10A and BEAS-2B in order to achieve the same average ε (~0.3) for all cell types (Table 4-3). As shown in the four-dimensional (4D) graphs in Figure 4-7, D_{cell} and L_{deform} of MCF-10A and BEAS-2B cells are significantly different from those of MCF-7 and A549 cells, respectively. Moreover, MCF-10A and BEAS-2B cells transit the contraction channel more slowly as compared to MCF-7 and A549 cells, respectively. When comparing transverse deformation (δ_{deform}), we find that while A549 deform significantly less than BEAS-2B cells, MCF-7 and MCF-10A cells have similar deformation (Figure 4-8A).

Table 4-3. Applied strain in the contraction channel. D_{avg}, σ, w_c, ε_{avg} correspond to the average free cell diameter, cell diameter standard deviation, width of the contraction channel, and the average strain value, respectively. Strain is defined as the ratio of deformation to the cellular diameter, $\varepsilon=(D_{cell}-w_c)/D_{cell}$. *From Ref (31).*

Cell type	D_{avg} [μm]	σ	w_c [μm]	ε_{avg}
MCF-7	18.06	2.179	12	0.335
MCF-10A	15.18	1.014	10	0.341
A549	17.64	2.215	12	0.320
BEAS-2B	15.11	2.542	10	0.338

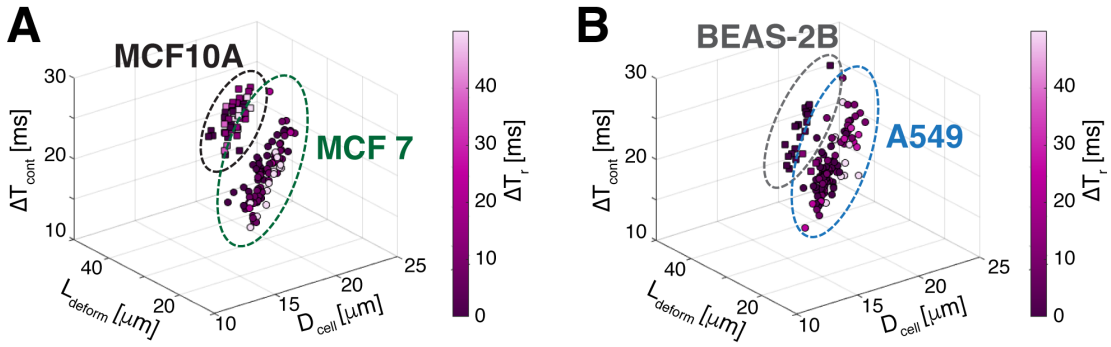

Figure 4-7. Biophysical properties of malignant and non-malignant epithelial cells. 4D plot of the free cell diameter (D_{cell}), elongation length (L_{deform}) due to an applied strain ε~0.3, transit time through the contraction channel (ΔT_{cont}), and recovery time from compressive deformation (ΔT_r) of **A**, malignant (MCF-7, n=99) and non-malignant (MCF-10A, n=99) breast cells, and **B**, malignant (A549, n=100) and non-malignant (BEAS-2B, n=100) lung cells. Dotted ovals group each cell line (MCF-10A: black, MCF-7: green, BEAS-2B: grey A549: blue). *From Ref (31).*

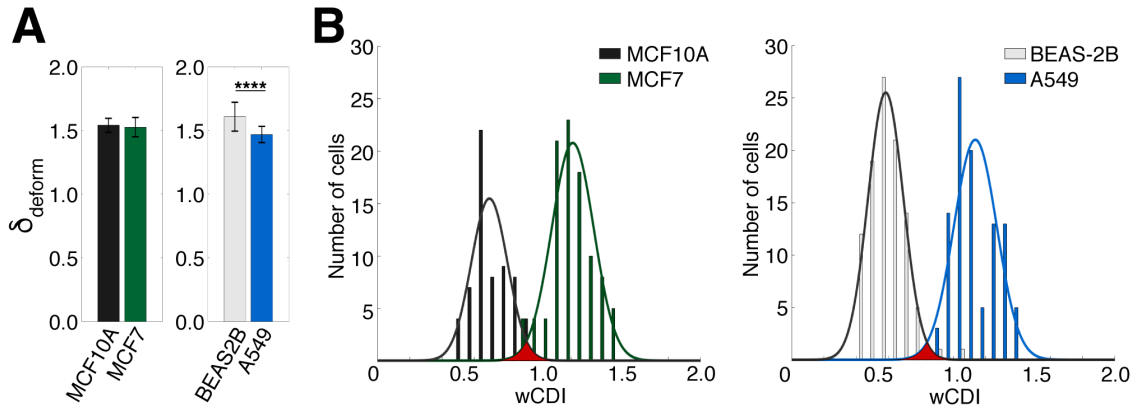

Figure 4-8. Mechanical phenotypes of malignant and non-malignant epithelial cells. A, Transverse deformation (δ_{deform}) of MCF-10A, MCF-7, BEAS-2B, and A549 cells. Statistical differences were determined by a paired t-test (**** indicates p≤0.0001). **B**, *wCDI* distribution of MCF-10A, MCF-7, BEAS-2B, and A549 cells. Statistical differences were determined by a paired t-test. (MCF-10A vs MCF-7: p=3.90e-58, BEAS-2B vs A549: p=1.10e-80). The solid lines correspond to the fitted normal wCDI distribution for malignant and non-malignant cells, respectively. MCF-10A: $\overline{wCDI}$=0.699±0.106; MCF-7: $\overline{wCDI}$=1.230±0.13; BEAS-2B: $\overline{wCDI}$=0.590±0.106; and A549: $\overline{wCDI}$=1.151±0.12. *From Ref (31).*

Although our results clearly show that the transit time through the contraction channel (ΔT_{cont}) is dependent on cell type (i.e. malignant *vs.* non-malignant), so too could cell diameter affect transit time (Figure 4-8) (74-76). Because this could lead to difficulties in distinguishing cells within a heterogeneous population (Figure 4-9 and 4-10), we employ the Buckingham π-technique (30) to define the *wCDI* (Equation (2.11), See Chapter 2 for detailed information). Among the consisting parameters of *wCDI*, U_{flow}, L_c, and $h_{channel}$ are fixed values for any given experiment, and consequently, D_{cell} and ΔT_{cont} become the key parameters in Equation (2.11). Physically, the *wCDI* describes the deformability of the cell as a whole, including the cytoskeleton, nucleus, and organelles. Cells that are more deformable (i.e. less stiff) transit through the contraction channel more easily, and subsequently at higher velocities, than those that are less deformable (i.e. more stiff). Correspondingly, these cells will have a higher *wCDI* as compared to the latter, in accordance with Equation (2.11). Moreover, cells which are larger (smaller) will transit the contraction channel more slowly (quickly), and Equation (2.11) effectively negates this cell-size effect. While the Buckingham π-technique relates the *wCDI* to the cell's elastic modulus, *E*, it does not define the explicit relationship between the two. We, therefore, performed side-by-side measurements of different cell lines (Jurkat, MCF-7, and MCF-10A) with the gold standard, micropipette aspiration, and also compared our measurements of MCF-7, MCF-10A, A549, and BEAS-2B cell lines with those obtained by AFM in the published literature (1, 3, 77-82). As shown in Chapter 2 (Figure 2-6), the *wCDI* is inversely proportional to both cortical tension and *E*, confirming our original physical description of the *wCDI*.

While future studies are necessary to determine the exact analytical expression between the *wCDI* and *E*, mechano-NPS's ability to mechanically phenotype cells successfully for cell-type discrimination is clearly demonstrated. Figure 4-8B shows the *wCDI* distribution of non-malignant *vs.* malignant cells. The solid lines correspond to the fitted normal distribution of each population and the red-shaded region is the overlap area of the two distributions. As shown in Figure 4-8B, the *wCDI* of MCF-7 cells is significantly greater than that of MCF-10A cells with a 2.6% overlap. Similarly, A549 cells have a greater numerical *wCDI* than BEAS-2B cells, but with only a 1.6% overlap. Given the sensitivity demonstrated using the *wCDI* vs. ΔT_{cont} or cell size, alone (Figure 4-8B, 4-9, and 4-10), mechano-NPS and correspondingly the *wCDI* could potentially be utilized as a method for detecting subtle heterogeneities within cell populations such as those found in primary tissue (83, 84), heterogeneous cell lines and strains (85), and biopsied tissue samples (86, 87).

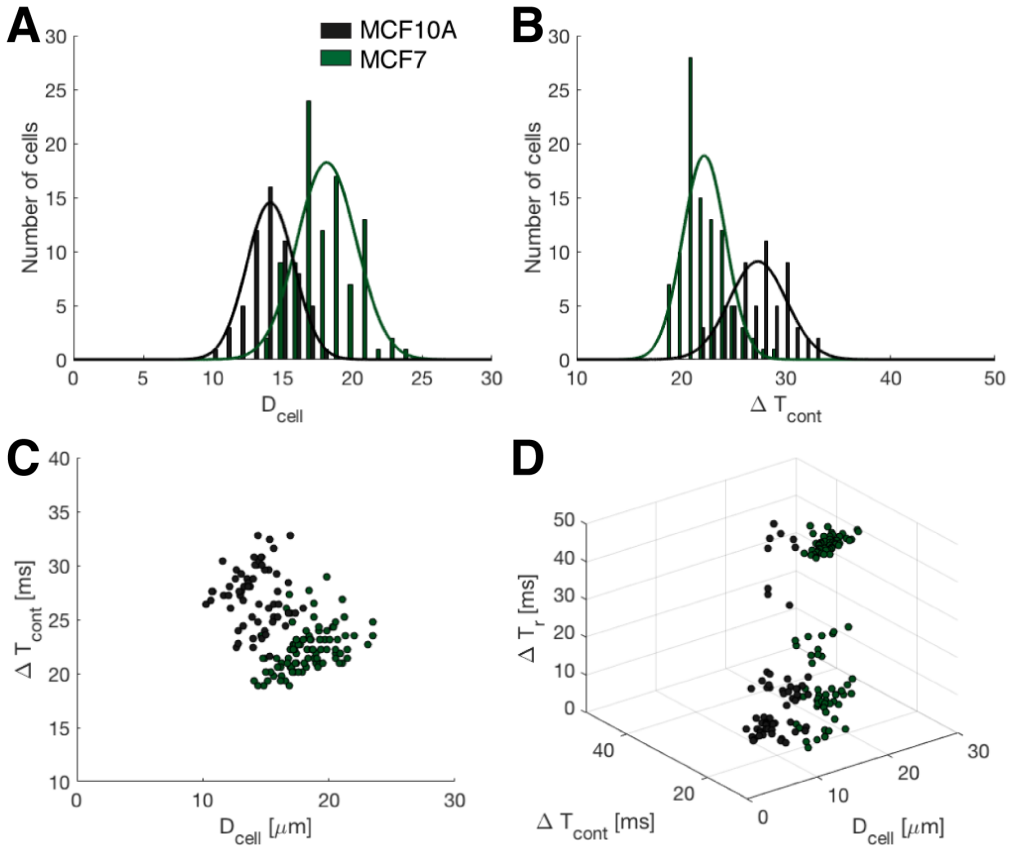

Figure 4-9. Biophysical parameters of breast epithelial cell lines as measured by mechano-NPS. A and **B**, Histogram of **A**, the free-cell diameter (D_{cell}) and **B**, the transit time (ΔT_{cont}) for breast epithelial cells (n=99 for both MCF-10A and MCF-7). The overlap area of the two ΔT_{cont} distributions is 28% of the total area. **C**, ΔT_{cont} of MCF-10A and MCF-7 cells with respect to cell size. **D**, 3D plot of the measured biophysical parameters of MCF-10A and MCF-7 cells. *From Ref (31).*

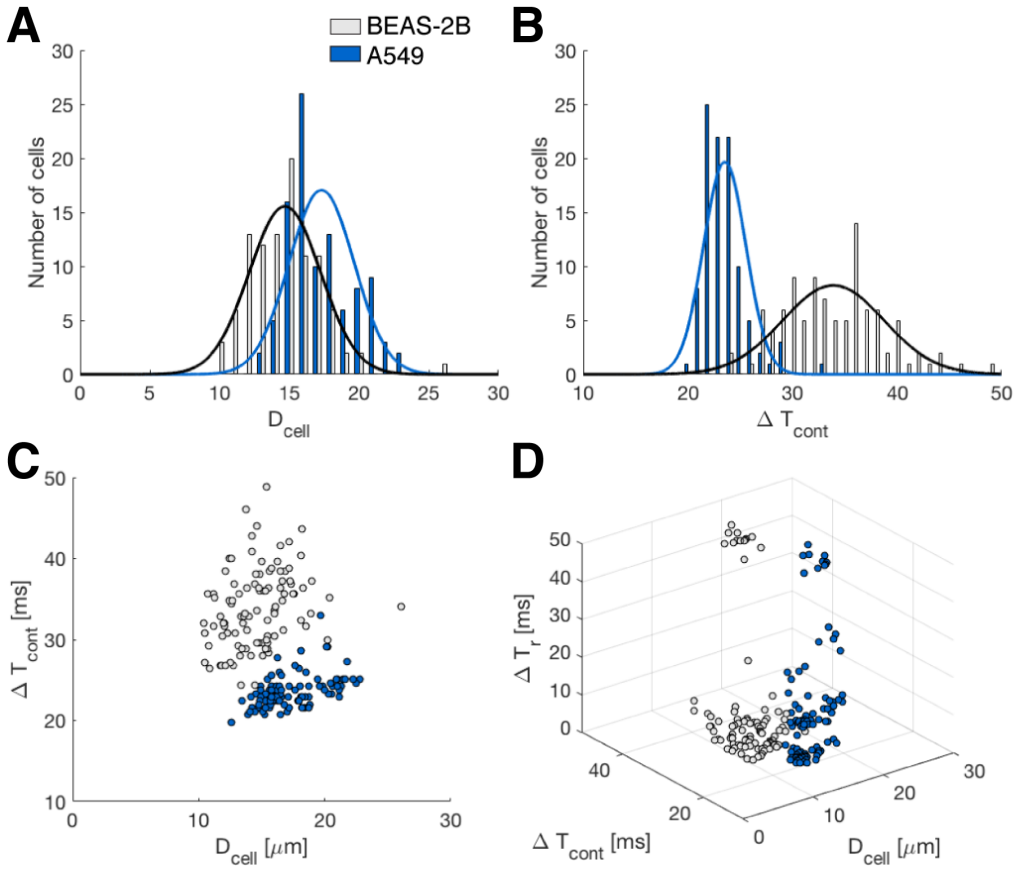

Figure 4-10. Biophysical parameters of lung epithelial cell lines as measured by mechano-NPS. A and **B**, Histogram of **A**, the free-cell diameter (D_{cell}) and **B**, ΔT_{cont} for lung epithelial cells (n=100 for both BEAS-2B and A549). The overlap area of the two ΔT_{cont} distribution is 12% of the total area. **C**, ΔT_{cont} of BEAS-2B and A549 cells with respect to cell size. **D**, 3D plot of the measured biophysical parameters of BEAS-2B and A549 cells. *From Ref (31).*

Clear differences are observed in the recovery time after mechanical strain between breast and lung epithelial cell lines and, in the case of the latter, between malignant and non-malignant cell lines. Figure 4-11 shows that there was no statistical difference (using a chi-square analysis) regarding instantaneous recovery from mechanical deformation among breast epithelial cells (38.3% malignant MCF-7 cells vs. 50% MCF10-A cells, p=0.101). This is in striking contrast to lung epithelial cells in which there was a strong statistical difference (p<0.0001) between malignant and non-malignant cell lines: 37.0% of malignant A549 cells recovered instantaneously vs. 82.0% of non-malignant BEAS-2B cells screened (Figure 4-11). Even though both are malignant cell lines, MCF-7 and A549 cell populations show surprising differences in their composition of transient and prolonged cell-recovery types. Whereas the majority of screened A549 cells transiently recovered (53.0%), MCF-7 cells were nearly evenly divided between transient and prolonged recovery (38.3% and 47.5%, respectively).

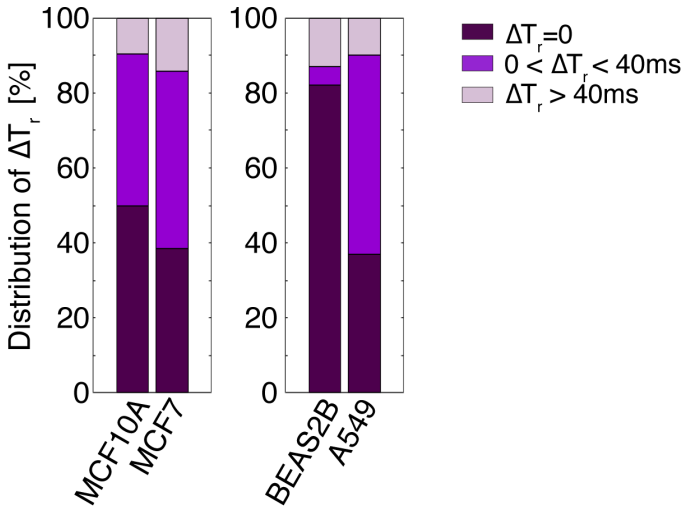

Figure 4-11. Cellular recovery of epithelial cells. The proportion of cells screened that recovered instantaneously ($\Delta T_r \sim 0$), required 40 ms or less ($0 < \Delta T_r \leq 40$ms), or did not recover within the window of time measured ($\Delta T_r > 40$ms). A chi-square test was employed to determine the statistical differences between the proportions of cell recovery types. There was no statistical difference in recovery types between MCF10A and MCF7 cells. In contrast, there was a significant statistical difference between BEAS-2B and A549 cells regarding instantaneous recovery ($p \leq 0.0001$) and transient recovery ($p \leq 0.0001$). *From Ref (31).*

4.3.3 Cell-Surface Interactions in Mechano-NPS

To determine whether cell-surface interactions greatly affect the passage of a cell within the contraction channel, and in turn contribute significantly to its *wCDI*, we screened MCF-7 cells in channels coated with either poly-D-lysine (PDL) or bovine serum albumin (BSA) and compared the resulting *wCDI* with that obtained by screening with a bare-PDMS channel (Figure 4-12). PDL increases cell-surface interactions by adding positive charges on the PDMS channel walls (88, 89) and would therefore lead to a lower *wCDI*. In contrast, BSA inhibits cellular adhesion to the PDMS surface (90) and would result in a higher *wCDI*. Figure 4-12B compares the *wCDI* obtained when MCF-7 cells were measured with bare-PDMS and PDL- and BSA-coated channels at different inlet pressures, i.e. flow speeds. At low pressures (P_{inlet}=7kPa and 14kPa), the average *wCDI* is appreciably lower in the PDL-coated channel and higher in the BSA-channel as compared to the bare-PDMS control channel. At P_{inlet}=21kPa, the inlet pressure at which we performed all our experiments, cells flow at a sufficiently high enough rate that cell-surface interactions are minimized within the contraction channel. As shown in Figure 4-12, the obtained *wCDI* at this inlet pressure for either the PDL- or BSA-coated channel is not a dramatic shift from that measured with the bare-PDMS control channel. Moreover, the difference in *wCDI* among the different surface treatments vs. the bare-PDMS control channel at 21kPa inlet pressure is significantly less than that measured between

malignant and non-malignant epithelial cell types (Figure 4-8). We, therefore, conclude that while surface-interactions do contribute to the *wCDI*, they are not the dominant factor at the higher inlet pressures or flow rates used for these studies.

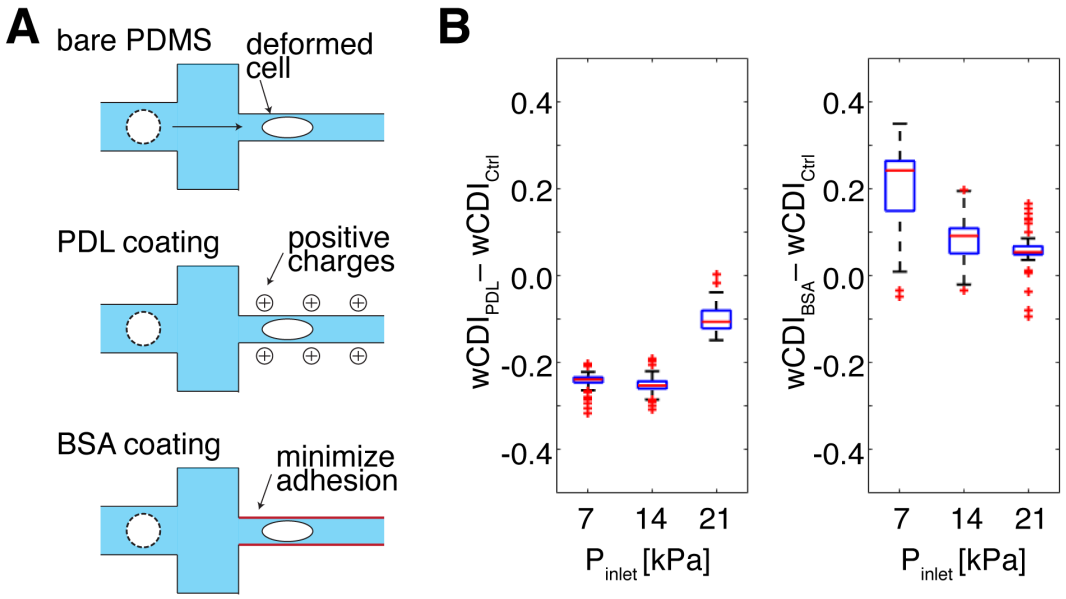

Figure 4-12. Contribution of cell-surface interaction to the mechanical phenotypes of epithelial cells. A, Schematic of experimental conditions used to measure the effects of cell-surface interaction on the *wCDI*. While poly-D-lysine (PDL) increases the positive charges on the channel wall for increased cell-surface interaction, bovine serum albumin (BSA) minimizes cellular adhesion to the channel wall. The control for all experiments was bare PDMS. **B**, The difference in *wCDI* measured when MCF-7 cells transit a bare PDMS contraction channel (control) and a PDL-coated channel or a BSA-coated channel (n=99 for all cases) under various fluidic conditions. The difference in *wCDI* becomes smaller with greater P_{inlet}. Within each box, the central red line corresponds to the median, and the edges of the box to 25% and 75% of the population. *From Ref (31).*

4.3.4 Contribution of Actin Filaments to the wCDI

Because we propose that mechano-NPS distinguishes cells based on mechanical differences, we should detect cytoskeletal perturbations. Thus, we treated MCF-7 and MCF-10A cells with the actin polymerization inhibitors, Latrunculin A (LatA) or B (LatB) (Figure 4-13), and subsequently screened them under a strain magnitude, $\varepsilon_{avg} \sim 0.3$. We found that the cellular deformation in the transverse direction (δ_{deform}) of both MCF-7 and MCF-10A cells treated with LatA and LatB was significantly reduced compared to their respective controls (Figure 4-14A), with MCF-7 cells generally more so than MCF-10A cells. Furthermore, we found that the *wCDI* increased for both LatA- and LatB-treated MCF-7 cells, and for LatA-treated MCF-10A cells as compared to the untreated control cells (Figure 4-14B). In subsequent experiments,

we observed that the change in *wCDI* caused by LatA treatment correspondingly increased with concentration for both MCF-7 and MCF-10A cells, with the latter more sensitive to the treatment (Figure 4-15). This is in contrast, however, to no detectable change in *wCDI* of MCF-10A cells no matter the LatB concentration. Overall, the different response of MCF-7 and MCF-10A cells to LatA and LatB may be due to differences in F-actin content, but further experiments are warranted here. As we confirmed with staining and confocal microscopy that the F-actin filaments were indeed inhibited in the Lat A- and B-treated cells (more so with Lat-A than with Lat-B as shown in Figure 4-14B), we conclude that mechano-NPS successfully detects cytoskeletal perturbations induced by exogenous chemicals.

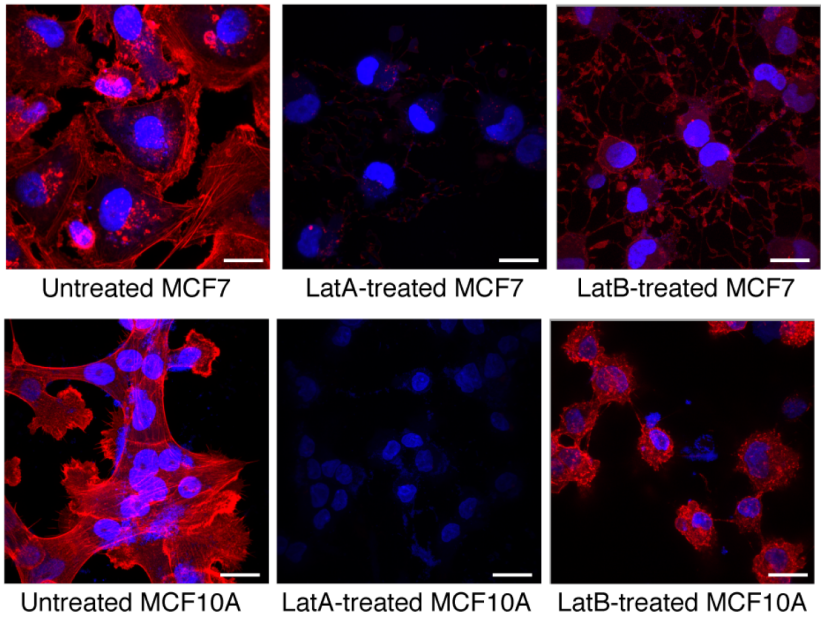

Figure 4-13. Fluorescence images of MCF-7 and MCF-10A cells after treatment with Latrunculin A (LatA, 5μg/mL, 1hr) or Latrunculin B (LatB, 5μg/mL, 1hr). Cell nuclei and F-actin are stained with 4',6-diamidino-2-phenylindole (DAPI, blue) and rhodamine Phalloidin (red), respectively. Scale bar corresponds to 20 μm. *From Ref (31).*

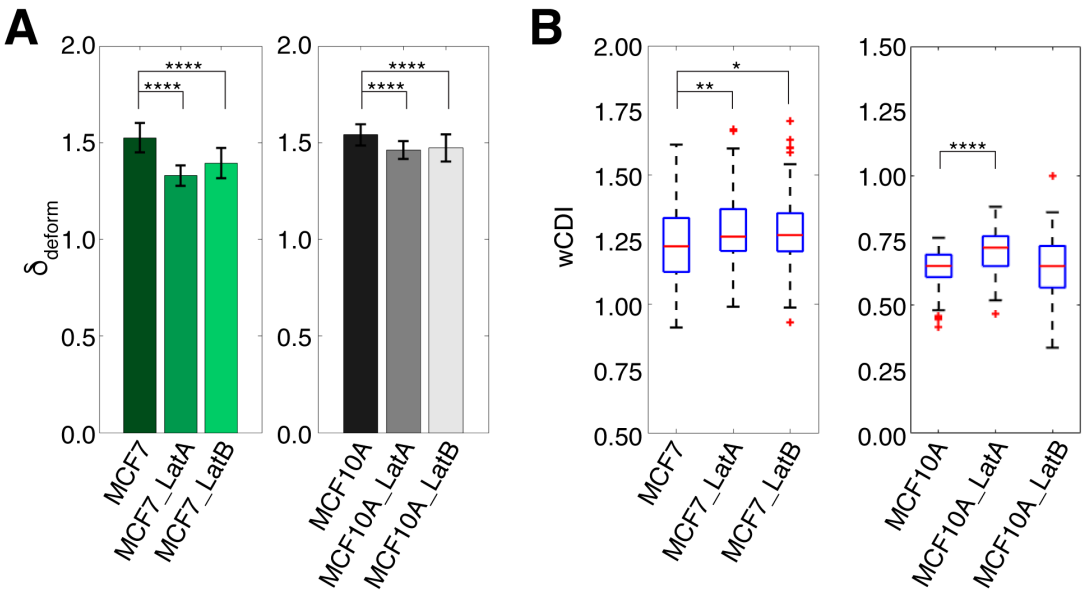

Figure 4-14. Mechanical phenotypes of Latrunculin-treated cells. A, Transverse deformation (δ_{deform}) of untreated, LatA-, and LatB-treated MCF7 and MCF10A cells (n=99). Statistical differences were determined by a paired t-test. **B**, *wCDI* distribution of MCF-7 (n=99, Ctrl vs LatA: p=0.0074, Ctrl vs LatB: p=0.0253) and MCF-10A cells (n=99, Ctrl vs LatA: p=4.8940e-7, Ctrl vs LatB: p=0.9758), in which cells were either untreated or treated with LatA or LatB. Statistical differences were determined by a paired t-test. Within each box, the central red line corresponds to the median, and the edges of the box to 25% and 75% of the population. *From Ref (31).*

While differences between the *wCDI* of LatA-treated cells are more pronounced with MCF-10A cells than MCF-7 cells, the differences in recovery time for Lat A- and LatB-treated cells in both cell types vs. the control are far more significant. Figure 4-16 shows that Latrunculin treatment results in the slow recovery of both MCF-7 and MCF-10A cells from the sudden relief of deformation. Moreover, there is a statistically significant difference between untreated and treated cells regarding recovery. In the case of MCF-7, only 8.1% of LatA–treated and 24.2% of LatB–treated cells instantaneously recover vs. 38.3% of untreated cells. For MCF-10A, the majority of LatA– and LatB–treated cells (66.7% and 41.4%, respectively) do not recover within the 40 ms time window our device offers (vs. 9.7% of untreated control cells). As we also found, the changes in cellular recovery are generally more pronounced at higher concentrations of Latrunculin treatment (Figure 4-17). These results support the notion that actin filaments contribute to the ability of cells to retain their original shape (63, 91). Moreover, mechano-NPS detects differences in recovery from deformation, either transiently or not at all, between LatA- and LatB-treatment that are consistent with LatA being the more avid inhibitor of actin polymerization.

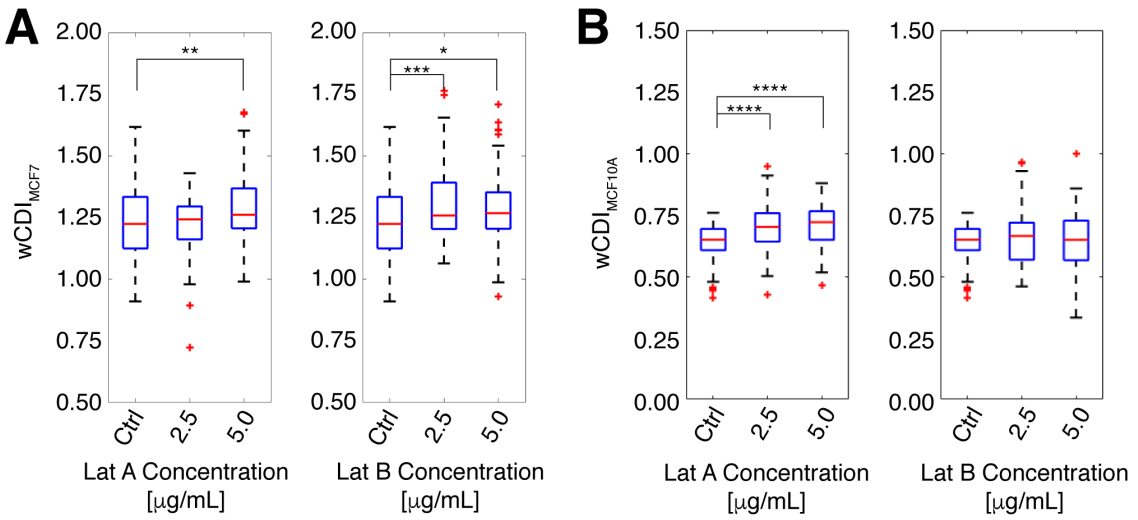

Figure 4-15. Effects of Latrunculin concentration to *wCDI*. **A**, *wCDI* of MCF-7 and **B**, MCF-10A cells treated with different concentrations of LatA and LatB (n=100 for all cases). Within each box, the central red line is the median, the red cross is an outlier, and the edges of the box correspond to 25% and 75% of the population. Statistical differences were determined by a paired t-test. For all graphs, *, **, ***, and **** indicate $p \leq 0.05$, $p \leq 0.01$, $p \leq 0.001$, and $p \leq 0.0001$, respectively. *From Ref (31).*

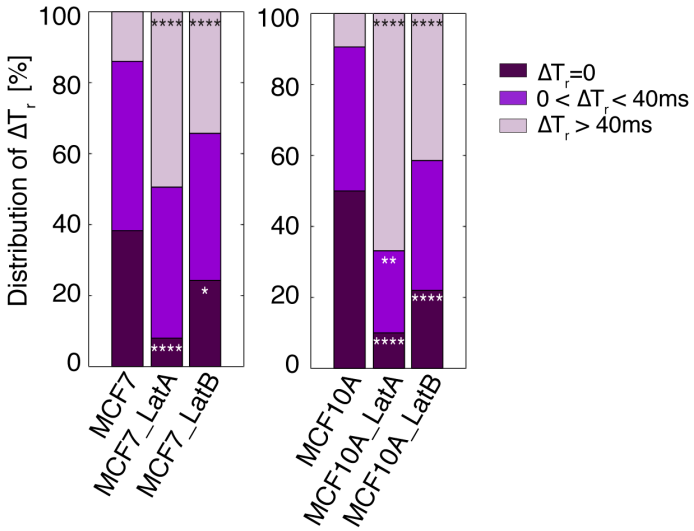

Figure 4-16. Recovery time of cells with Latrunculin treatment. The proportion of untreated and treated MCF-7 and MCF-10A cells screened that recovered instantaneously (ΔT_r~0), required 40 ms or less ($0<\Delta T_r \leq 40$ ms), or did not recover within window time measured (ΔT_r >40 ms). The statistical differences between the proportions of recovery types of untreated and treated cells were evaluated by

a chi-square test. *, **, ***, and **** indicate $p \leq 0.05$, $p \leq 0.01$, $p \leq 0.001$, and $p \leq 0.0001$, respectively. *From Ref (31).*

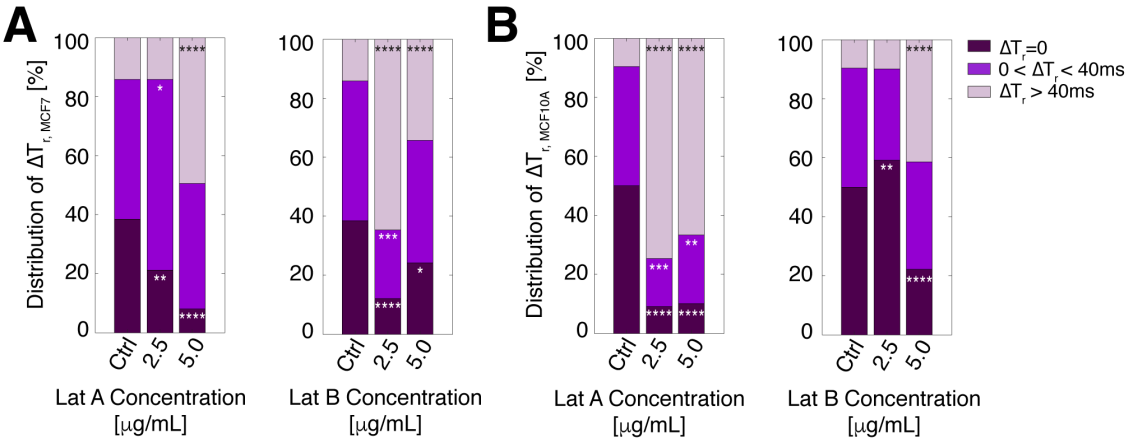

Figure 4-17. The distribution of recovery time with different Latrunculin concentration. ΔT_r of LatA- and LatB- treated **A**, MCF-7 and **B**, MCF-10A cells with various concentration. Statistical differences are determined by a chi-square test. *, **, ***, and **** indicate $p \leq 0.05$, $p \leq 0.01$, $p \leq 0.001$, and $p \leq 0.0001$, respectively. *From Ref (31).*

4.4 Discussion

Mechano-NPS is a versatile technique that can analyze populations of single cells for a number of biophysical properties, simultaneously. Our newly defined dimensionless parameter, *wCDI*, which corresponds to whole-cell deformability, allows us to compare different cell types directly. Complementing the *wCDI*, the quantification of the cellular deformation in the transverse direction when cells are subject to compressive deformation, cell recovery from deformation, and the subsequent distribution of different cell-recovery types provide unique information about a cell population. Utilizing just these three parameters, we have shown stark differences between, and even patterns of cell recovery among, malignant and non-malignant cells along with changes in the cytoskeleton. In general, the multi-variable phenotyping achieved by mechano-NPS provides a comprehensive understanding of single-cell mechanical behavior. Hierarchical clustering analysis of the NPS-screened mechanical phenotypes demonstrates a relationship among specific mechanical phenotypes with respect to different cell lines (Figure 4-18).

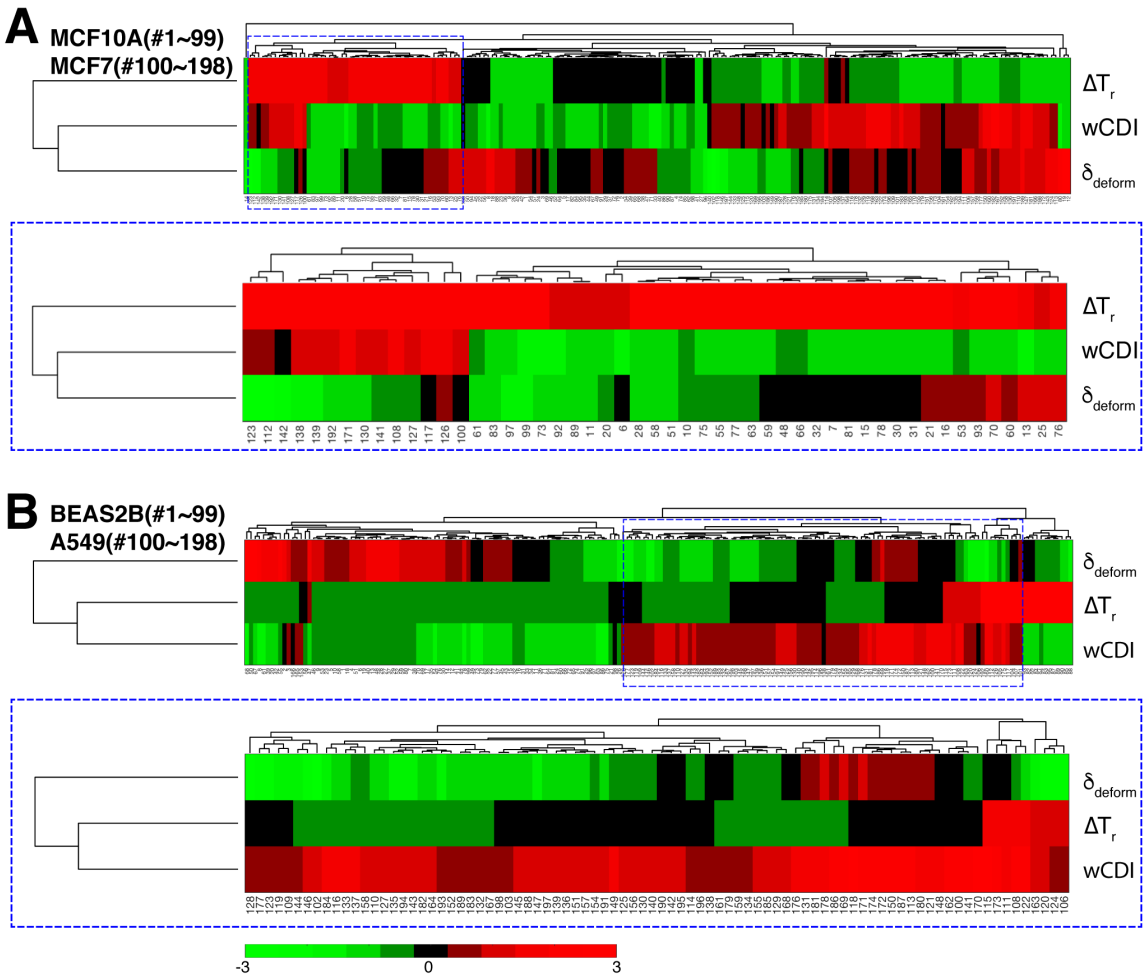

Figure 4-18. Hierarchical relationship among the mechanical phenotypes of breast and lung epithelial cells. A, Mechanical profiling of non-malignant and malignant breast epithelial cells (MCF-10A and MCF-7, respectively). An individual column represents relative intensity of mechanical phenotypes of each single cell. Blue dashed box (bottom) shows an enlarged heat map of a sub-group of the entire population. Among the mechanical phenotypes, the *wCDI* of breast epithelial cells is more related with δ_{deform} rather than ΔT_{r}. **B**, Mechanical profiling of non-malignant and malignant lung epithelial cells (BEAS-2B and A549, respectively). An individual column represents relative intensity of mechanical phenotypes of each single cell. Blue dashed box (bottom) shows an enlarged heat map of a sub-group of the entire population. Among the mechanical phenotypes, *wCDI* of lung epithelial cells is more related with ΔT_{r} rather than δ_{deform}. *From Ref (31).*

While we have focused on the *wCDI*, transverse deformation, and cell recovery here, additional biophysical parameters could be measured with mechano-NPS simply by adding more node-pore sequences, which would, for instance, increase the time resolution needed for investigating the mechanical plasticity of cells. We could also utilize different contraction channel geometries. For example, in Chapter 6, I introduce visco-NPS which utilizes a

sinusoidal contraction channel. This channel can, as will be discussed, induce periodic deformation to probe cellular viscoelastic properties. Taken together, the many biophysical properties that could be measured with mechano-NPS would lead to a better understanding of the origins of specific cellular mechanical properties and the mechanical contributions of different cellular components (e.g. cytoskeleton, nuclear envelope, organelles, and their own associated non-linear properties). In general, however, mechano-NPS in its present form successfully mechanically phenotypes cells for identification. Additional attractive features of mechano-NPS include that it is label-free, screened cells remain viable (Figure 4-19), and the potential to couple this technique with microfluidic cell-sorting technologies.

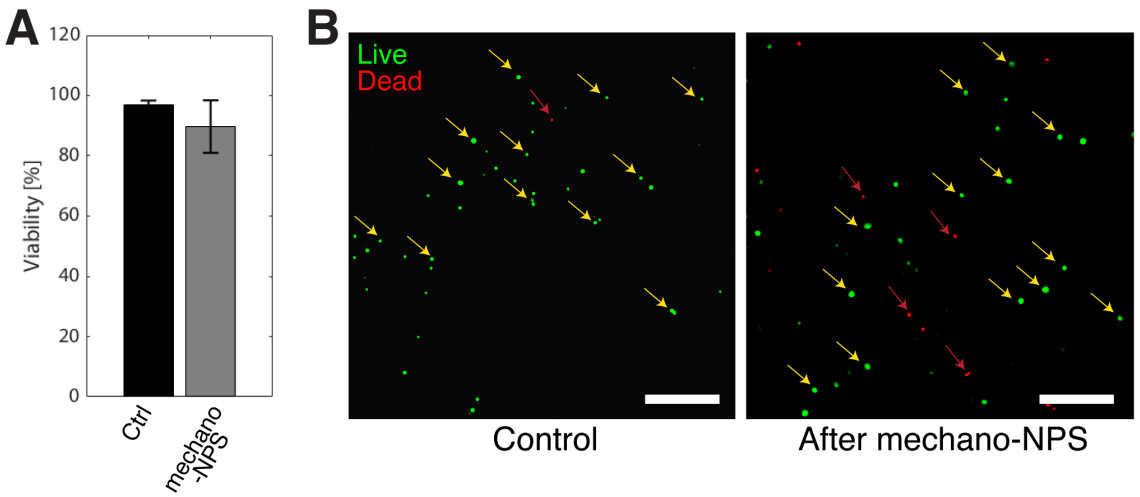

Figure 4-19. Cell viability after mechano-NPS screening. A, Viability of A549 cells after being screened with a 0.45-magnitude strain magnitude. The control corresponds to unscreened A549 cells kept at 4°C throughout the time the other cells were screened. All error bars are expressed as standard deviation. **B**, Fluorescence images of control and screened cells after Live/Dead assay (LIVE/DEAD® Viability/Cytotoxicity Kit, ThermoFisher, L-3224). Green corresponds to live cells (yellow arrows) and red to dead cells (red arrows). Scale bar corresponds to 200 μm. From Ref**(31).**

In terms of throughput, we screened up to 350 cells/min with our mechano-NPS device in the experiments we have presented. Because of the overall length of the channel, coincidence events, in which more than one cell occupies the channel at any given time, occur on occasion, especially when screening a high concentration of cells. Because of their complexity, current pulses arising from these events are presently removed from analysis. Implementing advanced signal processing, such as match filtering, could deconvolve these particular pulses and substantially increase throughput by enabling higher flow rate and higher concentration of cells (92, 93). Although it currently has significantly lower throughput compared to hydrodynamic stretching cytometry (11), deformability cytometry (58, 59), and RT-DC (13), mechano-NPS does not rely on optical imaging and therefore can easily be scaled up. Many mechano-NPS channels can be operated in parallel, resulting in overall increased throughput (potentially on the order of many thousands of cells/min), while importantly still maintaining

the ability to examine cell recovery. Equally important, the simplicity of mechano-NPS, even in multiplexed form, is preserved.

Using mechano-NPS and various other different methods to measure cell-to-cell mechanical properties open up new possibilities to understanding the biological underpinnings of the different measurements. Mechano-NPS reveals and quantifies emergent functional properties of the cytoskeleton of cells. Consequently, mechano-NPS can evaluate cytoskeleton-targeted drugs (e.g. estramustine, colchicine, and paclitaxel), which are often employed in cancer therapies (94, 95), and may provide a new window into drug resistance of cancer cells, which could be caused in part by their cytoskeletal components (96, 97).

Overall, mechano-NPS represents an efficient, simple, and direct means to quantify multiple mechanical properties of single cells in heterogeneous populations.

5 MECHANICAL PHENOTYPING OF HUMAN MAMMARY EPITHELIAL CELLS

Chapter Overview

This chapter describes using the mechano-NPS platform introduced in Chapter 4 to identify mechanical phenotypes of human Mammary Epithelial Cells (hMECs). Mechano-NPS is shown to distinguish sub-lineages of hMECs and track malignant progression.

5.1 Introduction

hMECs broadly consist of two lineages, myoepithelial (MEP) cells and luminal epithelial (LEP) cells (Figure 5-1). MEP and LEP cells have distinct roles in breast tissue. MEP cells play active roles in ductal contraction and in tumor suppression, and LEP cells produce milk and may represent a target-cell-type for carcinogenesis (98). Previous studies of mammary epithelia have implicated profound roles of cytoskeletal components in morphogenesis (46, 99, 100). To determine whether mechano-NPS could discriminate different lineages and chronological age groups within a population of primary epithelial cells, we screened the mechanical phenotypes of hMECs.

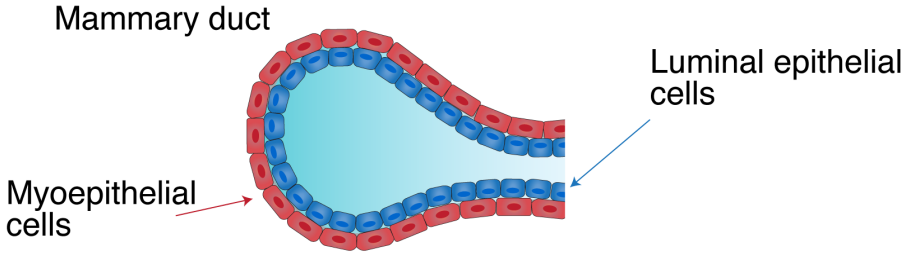

Figure 5-1. Cellular structure of the human mammary gland. The mammary duct consists of an outer layer of myoepithelial cells (red) that surround an inner layer of luminal epithelial cells (blue).

5.2 Experimental Method

5.2.1 Cell Culture and Preparation

Primary hMEC strains were obtained from our collaborators, Prof. Mark LaBarge (City of Hope) and Dr. Martha Stampfer (Lawrence Berkeley National Laboratory, LBNL), who generated and maintained these strains as described previously (101, 102). HMECs were grown in M87A medium containing cholera toxin and oxytocin at 0.5 ng/mL and 0.1nM,

respectively. Details on the derivation and culture of these hMEC strains can be found at Human Mammary Epithelial Cell (HMEC) Bank Website (103). Research was conducted under LBNL Human Subjects Committee IRB protocols 305H002 and 108H004 which allow for the use of hMEC samples for future scientific research.

5.3 Results

5.3.1 Population Characterization of Sub-lineages

We measured the mechanical characteristics of two sub-lineages of hMECs (i.e. MEP and LEP cells). Since both MEP and LEP cells have a similar size range (Figure 5-2), we employed a 10 μm–wide contraction channel, corresponding to an ε_{avg} ~0.4 for all measurements. Figure 5-3 shows the relationship among the measured parameters of MEP and LEP cells (derived from a 66-year old woman, strain 237) that were FACS-enriched ahead of mechano-NPS characterization. Although LEP cells, on average, had a similar transverse deformation as that of MEP cells, they required less time to pass through the contraction channel (Figure 5-3), thus suggesting that they are more deformable to an applied strain in the channel-width direction. Furthermore, while the deformed diameter and transit time of both lineages are dependent on the free cellular diameter, there are clear differences between the *wCDI* distribution of MEP ($\overline{wCDI} = 0.865 \pm 0.107$) and LEP ($\overline{wCDI} = 1.133 \pm 0.144$) cells (Figure 5-4A). In terms of cell recovery, MEP and LEP cells show a similar distribution of recovery types (Figure 5-4B).

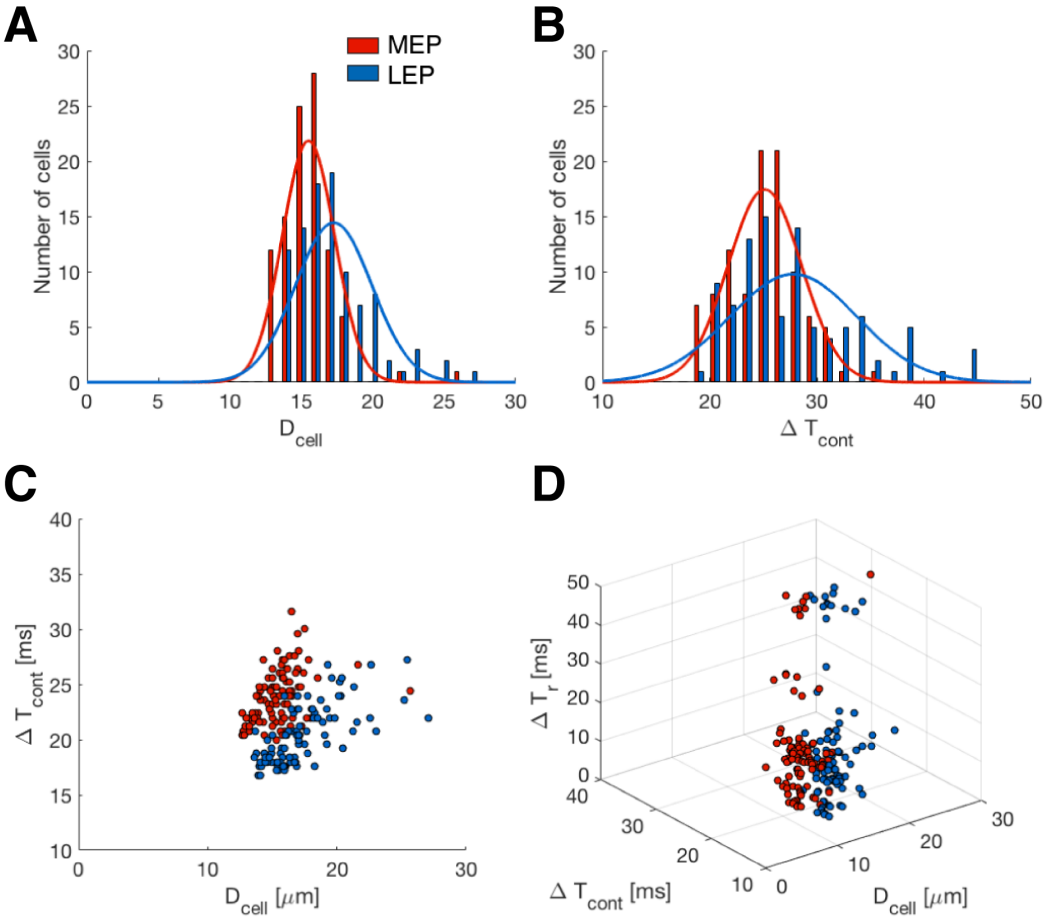

Figure 5-2. Biophysical parameters of hMECs as measured by mechano-NPS. A and **B**, Histogram of **A**, the free-cell diameter (D_{cell}) and **B**, ΔT_{cont} for sorted sub-lineages of hMECs (n=99 for both myoepithelial (MEP) cells and luminal epithelial (LEP) cells). The overlap area of the two ΔT_{cont} distributions is 68% of the total area. **C**, ΔT_{cont} of MEP and LEP cells with respect to the cell size. **D**, 3D plot of the measured biophysical parameters of MEP and LEP cells. *From Ref (31).*

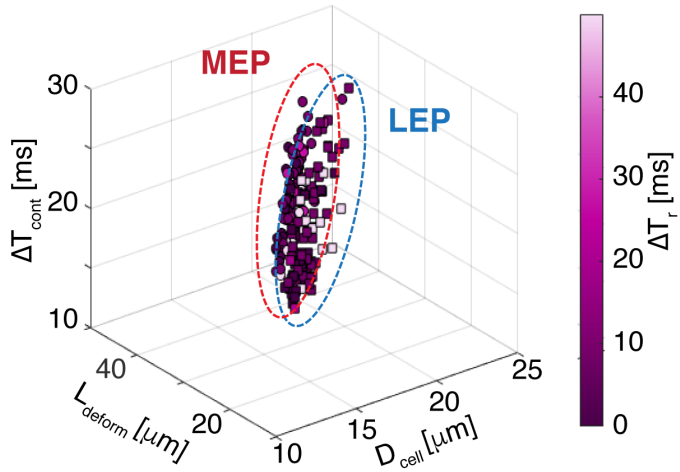

Figure 5-3. 4D plot of the cell diameter (D_{cell}), elongated length (L_{deform}), transit time through the contraction channel (ΔT_{cont}), and recovery time (ΔT_r) of myoepithelial (MEP, n=99) and luminal epithelial (LEP, n=104) breast cells. Dotted ovals group each sub-lineage (MEP: red and LEP: blue). Pre-sorted MEP and LEP cells were screened with an applied strain magnitude $\varepsilon \sim 0.4$. *From Ref (31).*

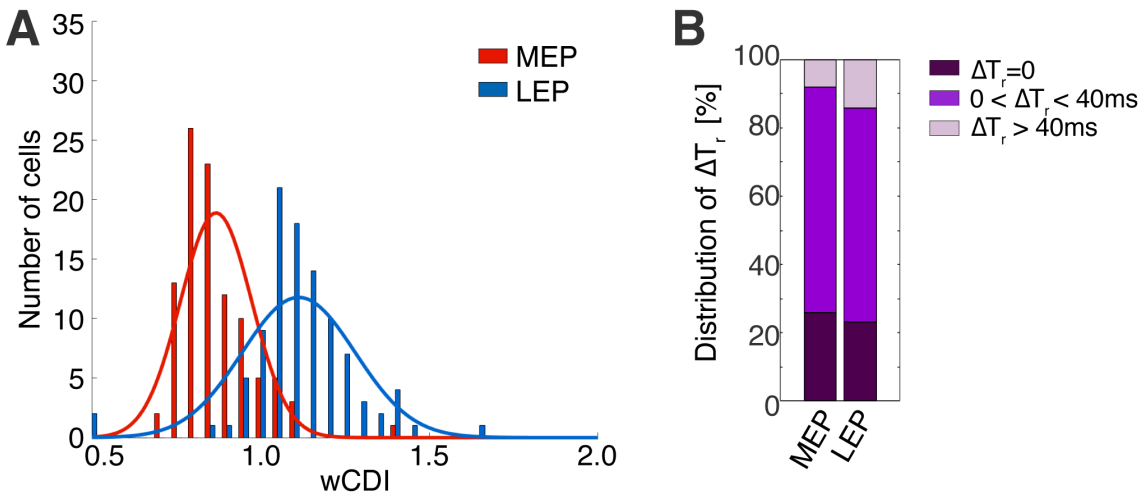

Figure 5-4. Mechanical Phenotyping of hMECs. A, *wCDI* distributions of MEP and LEP lineages (p=1.2047e-25). Statistical differences were determined by a paired t-test. The red and blue lines correspond to the fitted normal distribution of MEP ($\overline{wCDI}$=0.865±0.107) and LEP ($\overline{wCDI}$=1.133±0.144) cells, respectively. The *wCDI* overlap between the two lineages is 29.3%. **B**, Distribution of pre-sorted MEP and LEP cells that have instant (ΔT_r~0,), transient (0<ΔT_r≤40 ms), or prolonged (ΔT_r>40 ms) recovery. *From Ref (31).*

We also measured the mechanical properties of primary hMEC cultures that consisted of mixtures of MEP and LEP cells from eight women of different chronological age (four pre-menopausal women aged <30y and four post-menopausal women aged >55y). Using the

Expectation-Maximization algorithm (104), in which the *wCDI* distribution function of sorted MEP and LEP cells obtained in our earlier experiments (Figure 5-4A) were used as initial values, we determined the ratio (α) of MEP and LEP cells within each primary hMEC strain (Figure 5-5) and subsequently compared this ratio to FACS analysis of CD10+/CD227- MEP and CD10-/CD227+ LEP (Figure 5-6). The component ratios of MEP and LEP cells, as determined by the *wCDI* distributions, match exceptionally well with those obtained from FACS, as confirmed by a chi-square test with a p-value = 0.05 (Table 5-1). Indeed, the two methods are statistically indistinguishable. Although age-dependent differences in *wCDI* were not detected, age-dependent differences were readily apparent in recovery. Figure 5-7 show the composition of cell-recovery type for MEP and LEP cells of the young and old hMEC strains. Younger hMEC strains strikingly have a higher proportion of cells that recover instantaneously (an average of 47.8%) as compared to older strains (an average of 19.9%), suggesting that the cytoskeleton in younger cells is more resilient or more active, and in turn more responsive, to mechanical deformation.

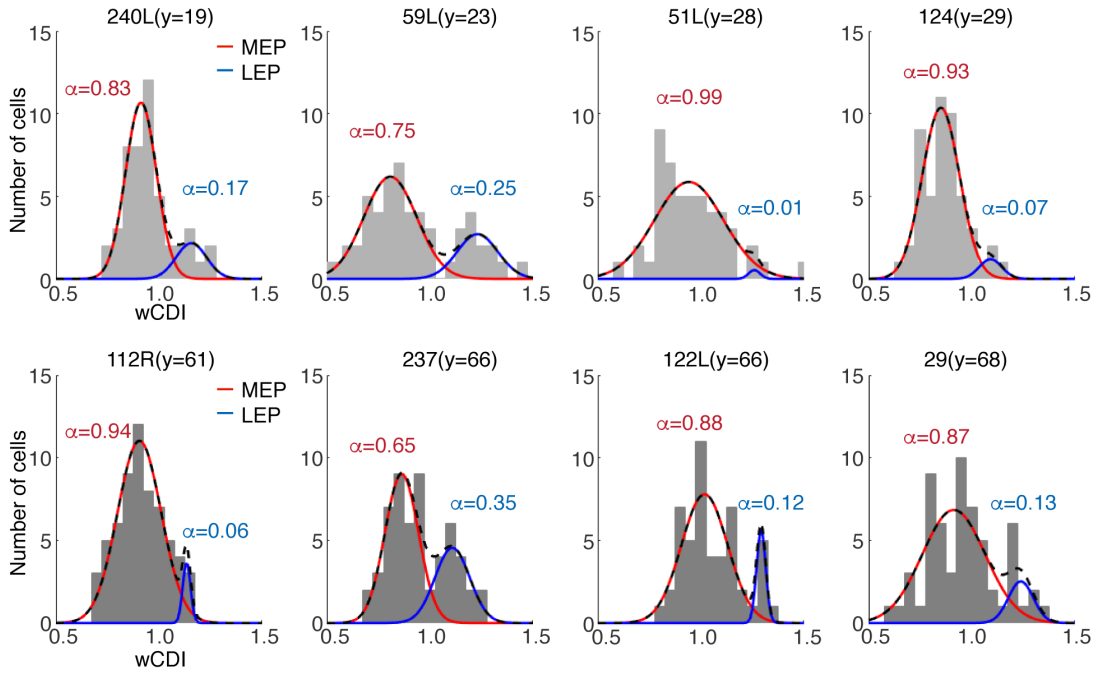

Figure 5-5. *wCDI* distribution of hMECs derived from young (y=age, 240L; *n*=54, 59L; *n*=53, 51L; *n*=50, 124; *n*=54) and old women (112R; *n*=62, 237; *n*=59, 122L; *n*=54, 29; *n*=60). Outliers over 3 standard deviation of the mean were removed. The black dashed line corresponds to the fitted normal distribution of hMECs (MEP+LEP). The red and blue solid lines represent the normal distribution of MEP and LEP cells, respectively, with the ratio (α) of each lineage in the hMEC population as determined by the Expectation-Maximization algorithm (104). *From Ref (31).*

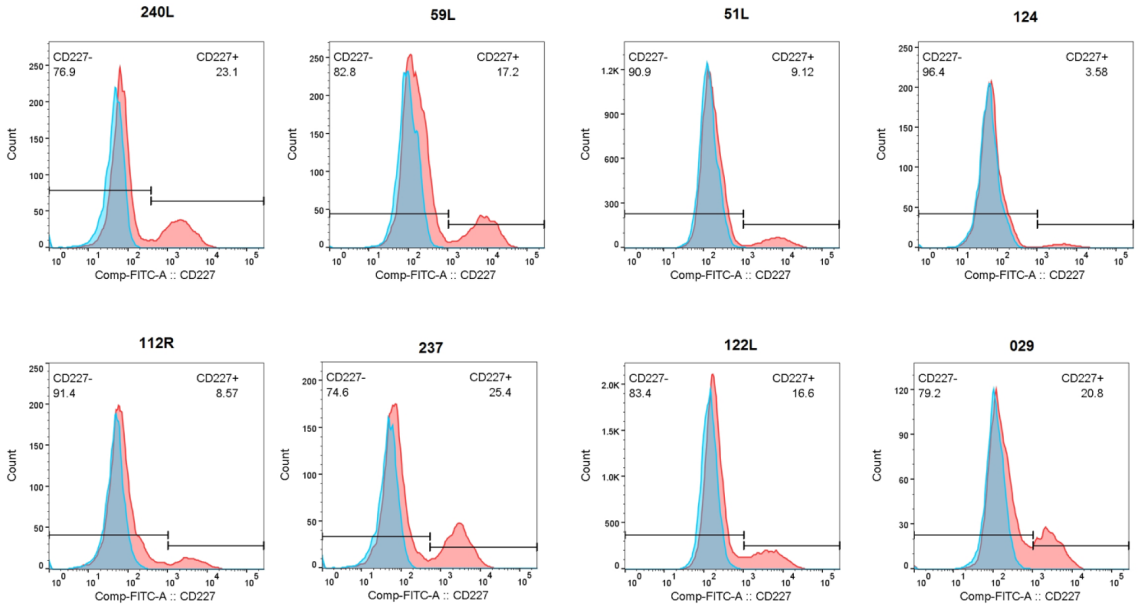

Figure 5-6. Fluorescence-activated cell sorting (FACS) analysis of hMECs. Representative histograms of MEP and LEP cells based on CD227 expression in different primary HMEC-strain populations after the fourth passage. Blue- and red-colored histograms correspond to the unstained negative control and CD227-stained cells, respectively (FITC, mouse anti-human CD227, Clone HMPV, BD Biosciences 559774). The component ratios of MEP and LEP cells, as determined by FACS, match exceptionally well with those obtained from the *wCDI* distributions, as confirmed by a chi-square test with a *p*-value = 0.05 (Table 3). *From Ref (31).*

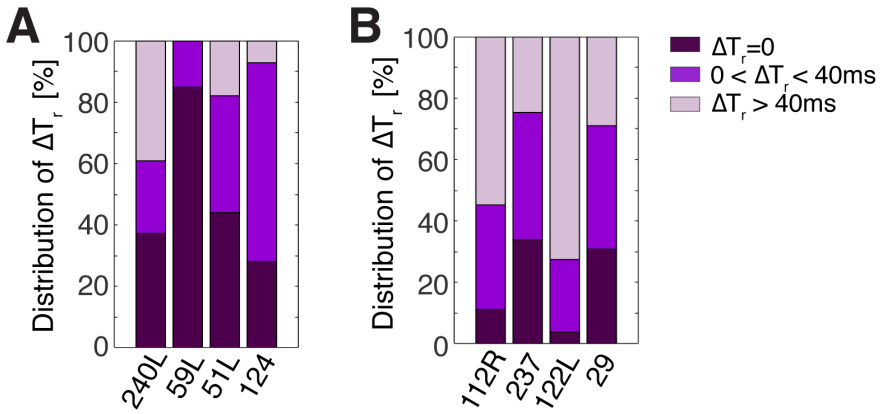

Figure 5-7. The proportion of hMECs from young (A) and old (B) women that have instant, transient, or prolonged recovery from applied strain. *From Ref (31).*

Table 5-1. Chi-square (χ^2) score of hMEC strains comparing wCDI with FACS analysis. *From Ref (31).*

Strain	240L	59L	51L	124	112R	237	122L	29

MEP χ^2	0.242	0.368	0.361	0.060	0.037	0.618	0.127	0.384
LEP χ^2	0.805	1.769	3.615	1.634	0.386	1.814	0.881	1.463

5.3.2 Effects of Malignant Progression to Mechanical Phenotypes

We next determined whether hMECs traversing the stages of malignant progression have distinctive mechanical signatures that could be used to track these stages. Our collaborator on this project, Prof. Mark LaBarge at the City of Hope, previously reported a method for producing post-stasis and immortal hMEC cell lines in the absence of gross, and confounding, genomic errors (105). In our particular experiments, expression of p16 shRNA or cyclin D1 was used to bypass the stress-induced stasis barrier, and expression of c-myc was used to bypass the replicative senescence barrier and generate immortal non-malignant cell lines (Figure 5-8). We used mechano-NPS to generate *wCDI* profiles and the recovery-type distribution of primary normal hMEC strains (240L and 122L), post-stasis finite strains (240L-p16sh, 240L-D1, 122L-p16sh, and 122L-D1), and immortal non-malignant cell lines (240Lp16sMY, 240LD1MY, 122Lp16sMY, and 122LD1MY). Each stage of malignant progression had a unique *wCDI* distribution. 240LD1MY, 122LD1MY, and 122Lp16sMY are known to have molecular and biochemical signatures of the luminal cancer subtype (106). Their *wCDI* profiles show a mean that is greater than those of their normal isogenic hMEC predecessors, which also is consistent with a more LEP phenotype (Figure 5-9). In contrast, 240p16sMY have a molecular and biochemical phenotype of basal breast cancers, which bear more similarity to MEP than to LEP lineage, and the *wCDI* distribution was more consistent with that of MEP (Figure 5-9). The post-stasis finite strains exhibited *wCDI* distributions that were intermediate phenotypes between normal hMEC and the isogenic immortal malignant cell lines, in a manner consistent with the eventual intrinsic luminal- or basal-like subtype of the immortal lines (Figure 5-9). Interestingly, all immortal non-malignant cell lines screened have a greater fraction of cells that exhibit instant or transient recovery as compared to those of post-stasis finite strains (Figure 5-10). When comparing the older pre-stasis strain, 122L to the isogenic immortal cell lines, there was a particularly stark decrease in recovery time (Figure 5-10). Thus, we observed two different types of mechanical signatures: *wCDI* differed between the MEP and LEP lineages, whereas recovery from deformation was a distinguishing characteristic of chronological age. Moreover, these data provide functional evidence to suggest that the process of immortalization is associated with fundamental changes in the ability of cytoskeletons to respond to deformation.

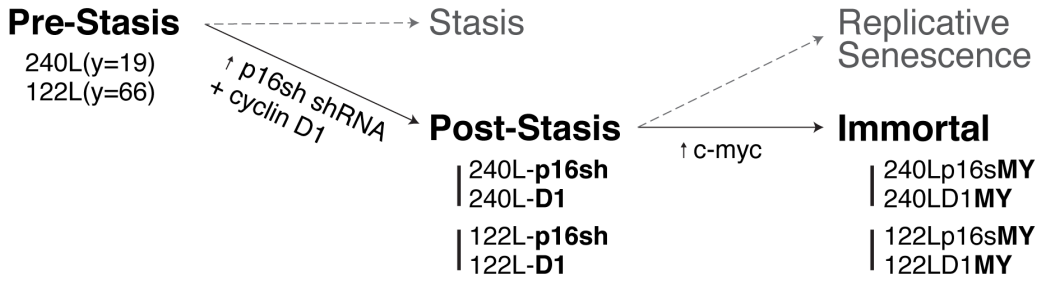

Figure 5-8. The stages of malignant progression in breast epithelia. *From Ref (31).*

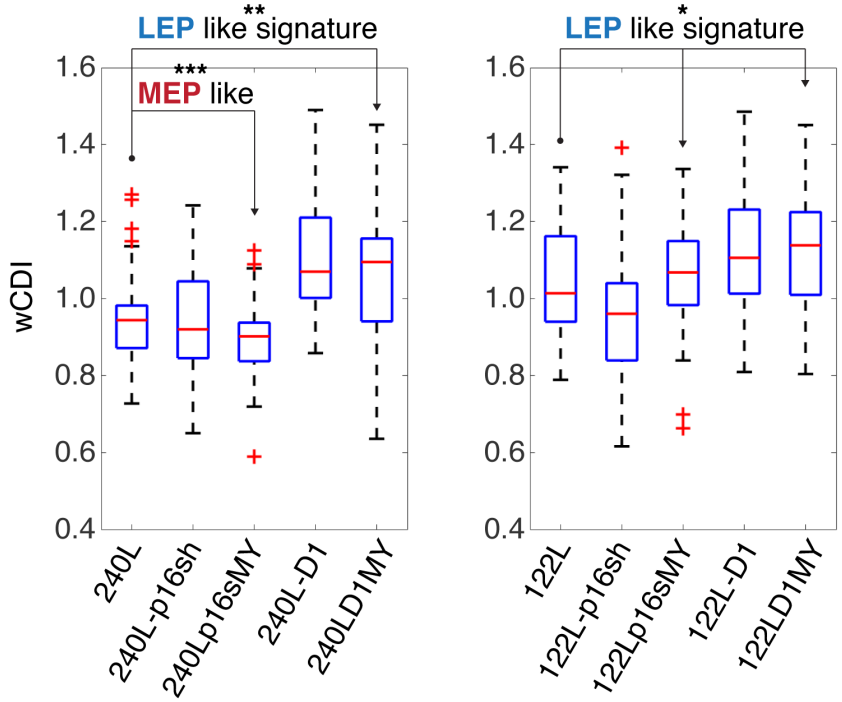

Figure 5-9. *wCDI* distribution of hMECs per the outlined immortalization steps when cells were screened with an applied strain of ε~0.4 (n=54 for all cases). Compared to primary cells (240L and 122L, respectively), each population has following p values, 240L-p16sh: p=0.5306, 240Lp16sMY: p=0.0003, 240L-D1: p=0.0005, 240LD1MY: p=0.0094, 122L-p16sh: p=0.0205, 122Lp16sMY: p=0.5668, 122L-D1: p=0.023, and 122LD1MY: p=0.011. Statistical differences were determined by a paired t-test. Within each box, the central red line is the median, the red cross is an outlier, and the edges of the box correspond to 25% and 75% of the population. *, **, ***, and **** indicate $p \leq 0.05$, $p \leq 0.01$, $p \leq 0.001$, and $p \leq 0.0001$, respectively. *From Ref (31).*

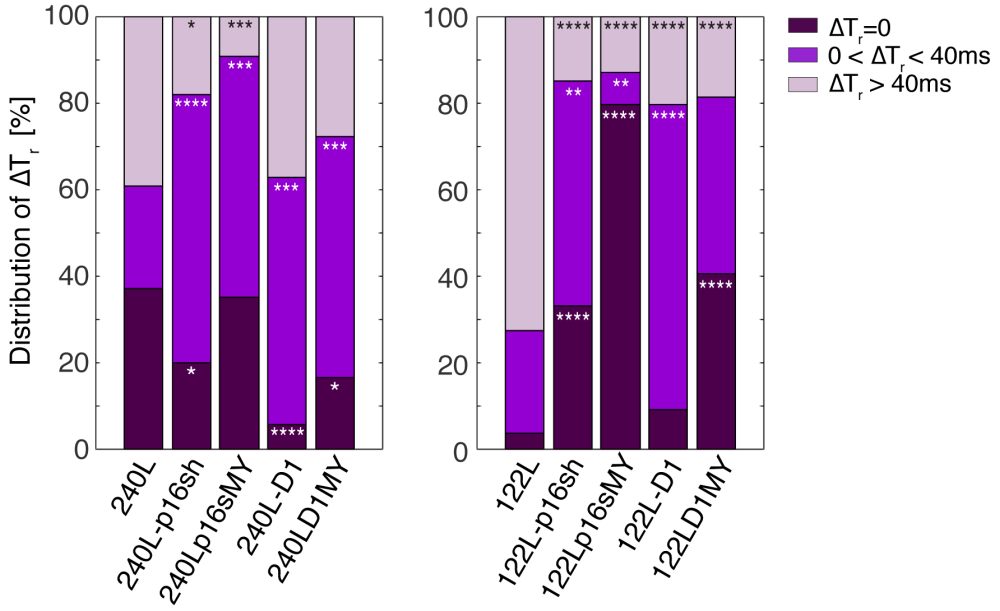

Figure 5-10. Distribution of instant (ΔT_r~0,), transient ($0<\Delta T_r\leq 40$ ms), or prolonged ($\Delta T_r>40$ ms) recovery within each hMEC population per immortalization step. The statistical differences between the proportions of recovery types of primary cells and each stage of malignant progression were evaluated by a chi-square test. *, **, ***, and **** indicate $p\leq 0.05$, $p\leq 0.01$, $p\leq 0.001$, and $p\leq 0.0001$, respectively. *From Ref (31).*

5.4 Discussion

The ability of our platform to rapidly characterize mechanical properties in populations of cells, such as hMECs, lends itself to numerous applications in cell biology and basic research. For example, mechano-NPS could be used to assay rapidly common laboratory cell lines cultured under different conditions and confluences, and to determine whether cells coming out of culture are in a similar state from day-to-day. Clinically, mechano-NPS may yield a new approach to early detection of breast and other types of cancer genesis through analyzing epithelial cells and their composition ratio. Indeed, we have already demonstrated mechano-NPS's ability to distinguish between LEP and MEP lineages in mixed populations, between epithelial cells from pre- or post-menopausal women, and between normal and immortal transformed epithelial cells from the same individual. The proportions of MEP and LEP subpopulations in mammary epithelium is highly associated with age of women (101), and when combined with distinct deformation recovery phenotypes in normal and transformed cells, mechano-NPS may yield valuable information regarding risk or diagnosis of breast cancer. LaBarge et al. (101) previously reported that the intrinsic subtype of immortal transformed hMEC was observable at the earliest stage of progression, bypass of stress-induced stasis, using molecular and biochemical markers of lineage. Here, we show that the stage of progression and the intrinsic subtypes are associated with distinctive mechanical phenotypes, opening up the possibility that *wCDI* could be used in a diagnostic setting as well.

6 MICROFLUIDIC RHEOLOGY THROUGH VISCO-NODE-PORE SENSING

Chapter Overview

This chapter introduces an electronic-based microfluidic platform to measure the viscoelastic properties of cells at the single-cell level. Compared to the mechano-NPS platform described in Chapters 4 and 5 that screens various types of cells for their mechanophenotype, visco-NPS provides a more in-depth biophysical understanding of cellular mechanics. By measuring the viscoelastic properties of cells and the frequency-dependence of these properties, we can determine the effects of malignancy, cytoskeletal structure, and cellular mechanical transitions that occur throughout the cell-cycle on whole-cell mechanical properties.

6.1 Introduction

Cellular mechanical properties are recognized as important indicators of biologically relevant functions of cells and tissues (107, 108). In particular, viscoelastic properties provide valuable information regarding how cells facilitate their movement and minimize damage from external stimuli through storing and dissipating energy (109, 110). Governing the viscoelastic responses of cells are intracellular components such as actin filaments, microtubules, and the nucleus—all of which play important roles in the dynamics of cell proliferation (111), migration (112), differentiation (41, 113), and apoptosis (114). Mechanical characterization of cells also provides clinical merits in terms of detecting cellular changes that are due to, for instance, cancer malignancy (31, 115, 116), cell-cycle (13, 117), stem cell differentiation (118-120), or epithelial-mesenchymal transition (EMT) (121, 122). Thus, analyzing viscoelastic properties of cells provides not only a fundamental understanding of biophysical characteristics but also a tremendous potential for clinical applications.

To quantify the viscoelastic properties of cells, different rheological methods have been developed. To name just a few examples, micropipette aspiration (123, 124), microplate rheometer (10, 125), optical stretcher (126, 127), and atomic force microscopy (AFM) (80, 128) have all been used to measure the viscoelastic properties of cells with respect to different loading conditions, such as force magnitude and deformation frequency. These methods, however, have low throughput (only a few cells/hour (53, 129, 130)) and consequently are not

capable of screening large populations of cells—a critical need for clinical applications. To address this key drawback, a number of higher throughput microfluidic platforms have been developed, including hydrodynamic stretching cytometry (11, 58), real-time deformability cytometry (RT-DT) (13), and mechano-NPS (31). These particular methods, however, focus on mechanically phenotyping cells for screening purposes and do not provide the means to investigate basic cellular mechanics. Recent studies have reported microfluidic platforms that take a rheological approach and drive cells through a confining channel to measure their cellular viscoelastic properties (131, 132). However, these platforms rely on imaging, and consequently, they have a very limited temporal- and spatial- window for measurement, which in turn, severely restricts sample size and experimental conditions. Key information such as what is the frequency dependency of viscoelastic properties and what is the origin of whole-cell properties cannot be easily obtained. Thus, despite the many different platforms for cell mechanical measurements that exist today, none thus far are able to provide a comprehensive view of cellular mechanics.

Here, we introduce a novel microfluidic, all electronic-based platform to measure cellular viscoelastic properties. Our platform, visco-NPS, employs a rheological approach by utilizing a sinusoidal-shaped contraction channel. Cells that traverse the channel undergo an oscillating deformation as a result of the channel's periodically changing width. By integrating this unique channel with a node-pore sensor (15), we are able to measure the storage (elasticity) and loss (viscosity) modulus of cells. As we demonstrate, visco-NPS can successfully quantify the differences in the viscoelastic properties between malignant and non-malignant epithelial cells. Moreover, it can ascertain the individual contributions of cytoskeletal components, i.e. actin filaments and microtubules, to the mechanical behavior of cells. Finally, visco-NPS can determine the changes in cell mechanical properties that result from the dynamic transitions that the cytoskeleton and nucleus undergo during the cell cycle. Overall, visco-NPS represents an efficient, simple, and direct means to quantify the mechanical properties of single cells.

6.2 Experimental Methods

6.2.1 Platform Design

Visco-NPS consists of a microfluidic channel embedded in a polydimethylsiloxane (PDMS) mold that is bonded to a glass substrate with pre-defined platinum (Pt) electrodes and gold (Au) contact pads (See Chapter 3 for a detailed description of the device fabrication) (Figure 6-1A). The embedded channel has multiple components: in-plane filters and a sinusoidal contraction channel flanked by a set of pores and nodes (Figure 6-1B). The in-plane filters have 25 μm-wide gaps and subsequently remove cellular clusters that would otherwise clog the contraction channel. The first node-pore region measures, with sufficient SNR, the free-cell size based on the Coulter principle (15, 16, 31, 133) (See Chapter 2 for a detailed description). With its periodically changing width ($w_c = w_o + \alpha\cos(\omega t)$, where w_o, α, and ω are the initial width, strain amplitude, and deformation frequency, respectively), the contraction channel measures

the viscoelastic properties of transiting cells as they undergo a sinusoidal deformation (Figure 6-2A). For the experiments described here, the contraction-channel dimensions were chosen such that MCF-7 and MCF-10A cells were subject to the same strain, $\varepsilon=0.4+0.1\cos(\omega t)$ (Figure 6-3 and Table 6-1). Different periodic contraction channel lengths (L_p) were employed to control the deformation frequency applied to each cell type. Pressure-driven flow (13.7 ~ 27.6 kPa), via a commercial microfluidic flow controller (OB1 MK3, Elveflow), is used to drive 10 ~ 50 cells per minute cross the channel without coincidence events. By varying the flow rate, a wide range of ω is achieved even with the same L_p. A four-terminal measurement, as detailed in Chapter 3, is employed to measure the current across the channel (15, 16, 134). After low-pass filtering to remove noise from the measured signal, a derivative cut-off detection method (described in Chapter 3 and Appendices A and B) is employed to identify the start and end time point of each sub-pulse (ΔI_{np} and ΔI_c in Figure 1D) (31).

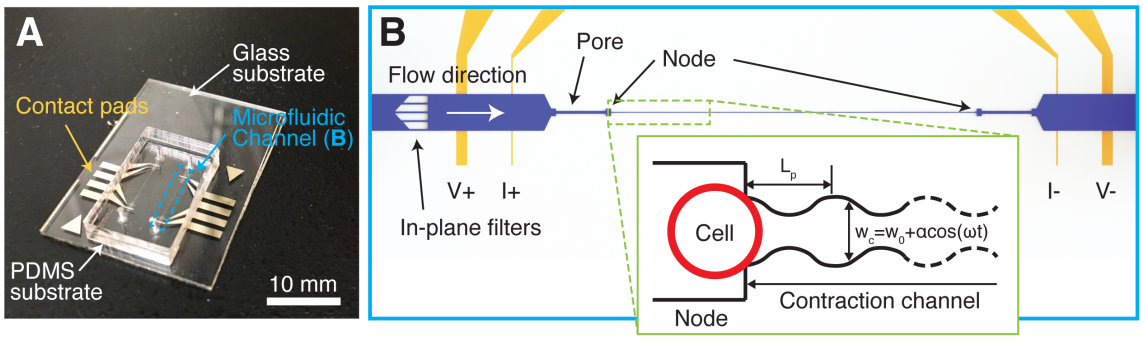

Figure 6-1. Structure of visco-NPS. A, photographic image of visco-NPS. The platform consists of a PDMS mold of a microfluidic channel bonded to a glass substrate with pre-defined electrodes (Blue dashed box). **B**, A schematic of the microfluidic channel, which has three main features: a pore, a node, and a sinusoidal contraction channel (Green dashed box). The outer electrodes apply a DC voltage across the channel, and the inner electrode pair measures the current across the channel. The in-plane filters, with their 25 μm gaps, prevent cellular clusters from entering the contraction channel. The inset shows the sinusoidal geometry of the contraction channel. The width of channel (w_c) gradually changes as a cosine function ($w_0+\alpha\cos(\omega t)$). L_p, w_0, α and ω correspond to the contraction channel's periodic length, initial width, strain amplitude, and deformation frequency, respectively. *From Ref (32).*

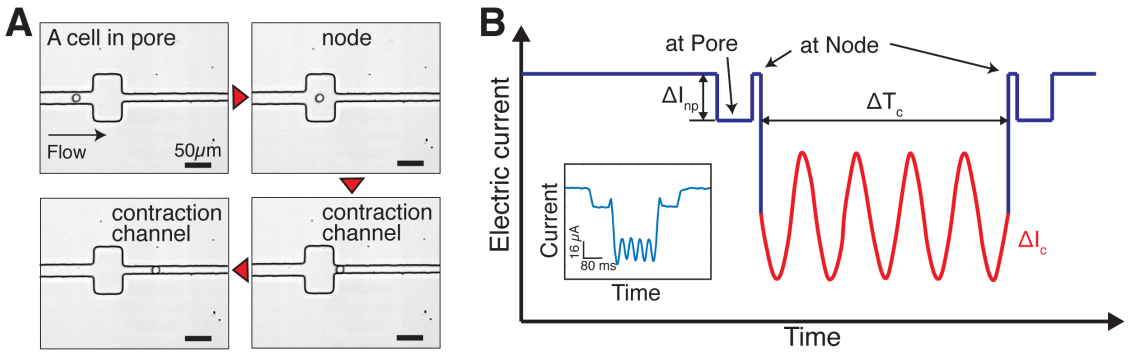

Figure 6-2. Cellular deformation through visco-NPS. A, Time-snapshots of an MCF-10A cell in each region of the microfluidic channel with the time sequence indicated by the red arrow. Because w_c (=8.75+1.5cos(ωt)) gradually changes along the channel length (L_p=1000 μm), the sinusoidal geometry of the contraction channel is not visible with the naked eye. **B**, Expected current pulse produced by a cell transiting the microfluidic channel. ΔI_{np} and ΔI_c correspond to the current drop by a cell transiting a node-pore and the contraction channel, respectively. The periodically changing width of the contraction channel causes the current drop to have the shape of sinusoidal function (red solid line). ΔT_c indicates the time duration of a cell transiting through the entire contraction channel. The inset shows an actual current pulse produced by an MCF-7 cell traversing a microfluidic channel with L_p =500 μm, a flow rate of 1.89 mm^3/min, and w_c of 10.5+1.5cos(ωt). *From Ref (32).*

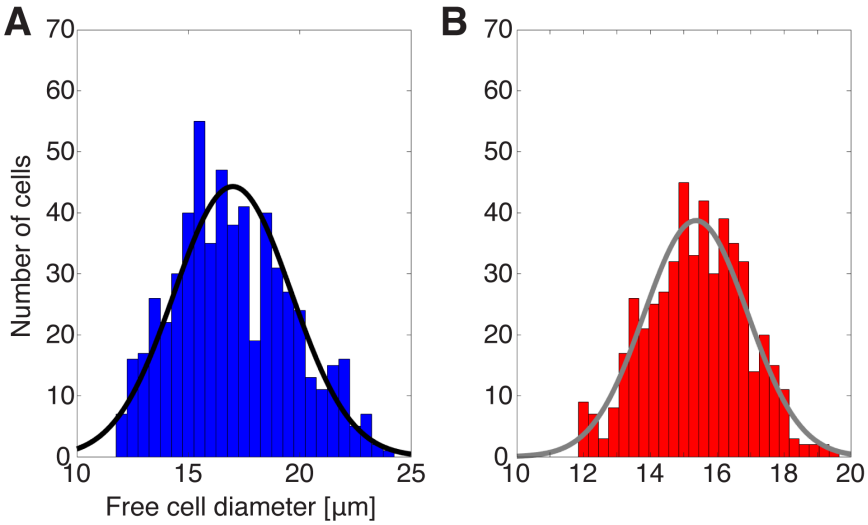

Figure 6-3. Distribution of free cell diameter for A, MCF-7 (D_{cell}=17.0±2.63μm, n=585) and B, MCF-10A (D_{cell}=15.2±1.48μm, n=515) cells. The black and grey solid lines correspond to the normal distribution of MCF-7 and MCF-10A cell diameter, respectively. *From Ref (32).*

Table 6-1. Microfluidic channel dimensions and the applied strain to cells. L_p, w_{pore}, and w_c, correspond to the periodic length of the contraction channel, pore width, and the contraction channel

width, respectively. D_{cell} is the free cell diameter (mean±standard deviation) and ε, the applied strain to the cells. *From Ref (32).*

Cell type	L_p [μm]	w_{pore} [μm]	w_c [μm]	D_{cell} [μm]	ε
MCF-7	1000 500	22	10.5+1.5cos(ωt)	17.0±2.63	0.4+0.1cos(ωt)
MCF-10A	1000 500	18	8.75+1.5cos(ωt)	15.2±1.48	

To validate statistical significance, an unpaired t-test, two-way ANOVA test, and/or Pearson correlation coefficient test was performed. Power analysis was employed to ensure that the measured sample size provides adequate power (>0.08) to detect statistical differences compared to their control groups with 95% confidence interval. All experimental groups with p-value <0.05 showed sufficient power value with the analyzed sample size (n=100) (Table 6-2). All data presented in this study were measured using two different microfluidic devices per experimental case to ensure repeatability of results. For example, the storage modulus (G') of MCF-10A cells was measured with two different device replicas. A comparison of the results showed no statistical difference (Figure 6-4).

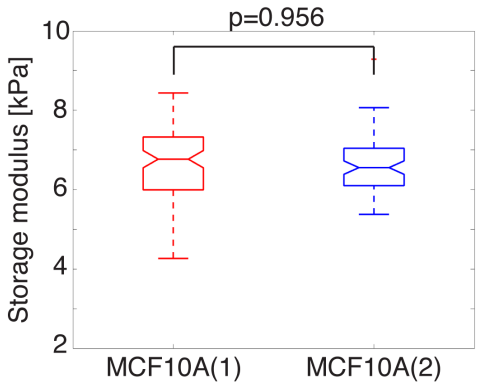

Figure 6-4. Storage modulus (G') of MCF-10A cells from different replicas of the visco-NPS device at a deformation frequency of 140 Hz. G' of MCF-10A cells as measured by the two different device replicas show no statistical difference through an un-paired t-test (MCF-10A(1): n=92, MCF10A(2): n=76, and p=0.956). Within each box, the central line is the median and the edges correspond to 25% and 75% of the G' distribution. *From Ref (32).*

Table 6-2. Power of experimental groups with p<0.05. The 2-sample and 2-sided power analysis with 95% of confidence interval was employed to ensure experimental groups have adequate power compared to their own control groups. With the analysed sample size (n=100 for all), all experimental cases show adequate power (>0.08). ω_{avg} corresponds to the averaged deformation frequency. *From Ref (32).*

Cell type	MCF-7_Jas	MCF-7_Jas	MCF-7_Jas	MCF-7_LatB	MCF-10A_Jas

ω_{avg} [Hz]	125	200	275	275	100
Power	0.987	1.000	0.999	1.000	1.000
Cell type	MCF-10A_Jas	MCF-10A_LatB	MCF-10A_LatB	MCF-7_TAX	MCF-7_TAX
ω_{avg} [Hz]	140	100	140	125	200
Power	0.995	0.978	0.976	1.000	0.999
Cell type	MCF-7_Noc	MCF-7_Noc	MCF-7_Noc	MCF-10A_TAX	MCF-10A_Noc
ω_{avg} [Hz]	125	200	275	180	100
Power	1.000	0.966	1.000	0.990	1.000
Cell type	MCF-10A_Noc	MCF-10A_Noc			
ω_{avg} [Hz]	140	180			
Power	1.000	1.000			

6.2.2 Electronic-based Measurement of Visco-NPS

We quantified multiple biophysical properties of cells, including free-cell diameter and deformation, by employing NPS (15, 16, 31) (See Chapter 2 for detailed information). As shown in Figure 6-2B, a unique current pulse is measured when a cell transits the channel. This unique pulse reflects the channel geometry, leading to the current pulse with the overall periodic structure. When the cell specifically transits the sinusoidal contraction channel and is periodically deformed, the resulting current sub-pulse also oscillates.

To determine the size a cell, Equation (2.6) is employed, where ΔI, I, d, D_e, L correspond to current drop, baseline current, cell diameter, effective channel diameter, and overall channel length, respectively (24, 134). D_e is numerically determined by measuring the $\Delta I/I$ caused by polystyrene microspheres of known size, d, traversing the channel (Table 6-3). The effective diameter of the first node-pore region, D_{e_np}, can thus be determined and used with $\Delta I_{np}/I$ in Equation (2.6) to quantify the free-cell dimeter (D_{cell}). The effective contraction channel diameter (D_{e_c}) is determined by a ratio of the hydraulic diameter of the node-pore and the contraction channel ($D_{e\_c}=D_{e\_np}\cdot\sqrt{w_c/w_{pore}}$). To quantify cellular deformation in the contraction channel, we assume that the cell undergoes an isometric deformation in a plane parallel to the channel's side walls and is consequently disk shape (Figure 6-5). We determine the deformed cell diameter (D_d) from $\Delta I_c/I \sim V_{deform}/V_{contraction}$, where V_{deform} and $V_{contraction}$ are the volume of the deformed cell and contraction channel, respectively (31).

Table 6-3. Quantification of the channel's effective diameter. Polystyrene microspheres (Polysciences, #64155) were used to measure the effective diameter of the node-pore channel region (D_{e_np}) (n=20 for all cases). Within the table, d, $\Delta I/I$, w_{pore}, L, and L_p, correspond to the average diameter

+ standard deviation of the spheres, width of pore, total channel length, and periodic length of the contraction channel, respectively. *From Ref (32).*

d [μm]	$\Delta I/I$	w_{pore} [μm]	L [μm]	L_p [μm]	D_{e_np} [μm]
14.73±1.36	5.39e-4	22	6500	1000	31.30
	9.09e-4		4000	500	27.70
	8.17e-4	18	6500	1000	26.10
	14.54e-4		4000	500	25.45

6.2.3 Cell Culture and Preparation

MCF-7 cells (ATCC® HTB-22™) were cultured in DMEM (Fisher Scientific, BW12719F), supplemented with 10% fetal bovine serum (FBS), 2 mM L-glutamine, and 1% Pen-Strep. MCF-10A cells (ATCC® CRL-10317™) were cultured in MEBM medium (ATCC® PCS-600-030™), supplemented with 0.1% insulin, 0.1% human Epidermal Growth Factor, 0.4% hydrocortisone, and 10% cholera toxin. All cell cultures were maintained at 37°C in 5% CO_2 and routinely passaged, per published protocols (135), once they reached 80% confluence. Cells were dissociated with 0.25% trypsin/EDTA for either 3 min (MCF-7 cells) or 5 min (MCF-10A cells) at 37°C (67, 136, 137), washed with respective growth media, centrifuged at 0.2 RCF for 4 min, and re-suspended at a concentration of ~500,000 cells/mL in PBS. To ensure cell viability, cells were injected into the prepared devices for measurement immediately following re-suspension.

6.2.4 Pharmacological Treatment for Cytoskeletal Components

Jasplakinlide (Jas, Abcam, USA) and Latrunculin B (LatB, Enzo Life Science, USA) were used to stabilize and disrupt actin polymerization, respectively. Paclitaxel (TAX, Abcam, USA) and Nocodazole (Noc, Thermo-Fisher Scientific, USA) were used to stabilize and perturb microtubule formation, respectively. All drugs were dissolved in dimethyl sulfoxide (DMSO) and then added to the respective growth medium for each cell type to achieve a final concentration of 200nM Jas, 5 μg/mL LatB, 2 μM TAX, and 20 μM Noc. Prior to measurement, MCF-7 and MCF-10A cells were incubated with Jas, LatB, TAX, or Noc solution for 6, 2, 18, or 10 hours at 37°C, respectively. The concentration and incubation time of the pharmacological treatments were chosen to have an adequate effect on the cells and are based on previously published work (31, 138). Cells were detached from their culture flask with 0.25% trypsin/EDTA, rinsed once with growth medium, centrifuged at 0.2 RCF for 4 min, and re-suspended in PBS at a concentration of ~500,000 cell/mL. To confirm that actin polymerization was successfully stabilized or disrupted by the treatment, cells were fixed with 4% (w/v) of paraformaldehyde in PBS for 15 min. They were then permeabilized with 0.1% Triton-X 100 (Sigma-Aldrich, USA) in PBS for 5 min. To visualize the effects of Jas and LatB treatments, cell nuclei and actin filaments were counter-stained with 4',6-diamidino-2-phenylindole (DAPI, Sigma-Aldrich, USA) and rhodamine phalloidin (Thermo-Fisher

Scientific, USA), respectively, using the protocols provided by the manufacturer. Stabilization and de-activation of microtubules were confirmed by staining with CellLight® Tubulin-GFP (Life Technology, USA) for live cells. For DAPI nuclear staining, cells were fixed and permeabilized using the same protocol described above. All stained cells were imaged with a Zeiss LSM780 confocal microscope.

6.2.5 Cell-cycle Synchronization

A standard double-thymidine block and release protocol was used to synchronize MCF-7 cells to the border of Gap 1 (G1)/Synthesis (S) phase (139). Briefly, cells were first treated with 2.5 mM of thymidine (Sigma-Aldrich, USA) for 20 hours, released into growth medium for 9 hours, and then treated once again with thymidine for an additional 16 hrs. Once synchronized, cells were captured in S- or G1- phase by incubating in fresh medium for 30 min or 12 hrs, respectively. To capture cells in Gap 2 (G2) phase, synchronized cells were incubated with 9 μM of CDK1 inhibitor RO3306 (VWR, USA) for 5 hours. Cells in Mitosis (M) phase were captured by incubating synchronized cells with 10 μM of dimethylenastron (VWR, USA) for 10 hours. All incubations were performed at 37°C with 5% of CO_2. To validate cell-cycle synchronization, cells in each phase were fixed and stained with DAPI (Sigma-Aldrich, USA) and rhodamine phalloidin (Thermo-Fisher Scientific, USA). The DNA content in the nucleus was quantified using DAPI fluorescence intensity. All synchronized cells were analyzed with visco-NPS using the methods described above.

6.3 Results

6.3.1 Measuring the Viscoelastic Properties of Epithelial Cells

We investigated and compared the viscoelastic properties of malignant MCF-7 and non-malignant MCF-10A breast epithelial cells. Both cell types were subject to periodic deformation as they traveled through our platform's sinusoidal contraction channel. By using contraction channels of different L_p in combination with a range of controlled flow rates, we were able to achieve a wide range of effective deformation frequencies (ω) with respect to different cell populations. As shown in Figure 6-5A and B, ω ranged from 20 Hz to 300 Hz for MCF-7 cells, and 20 Hz to 200 Hz for MCF-10A cells. Each ω range was sufficiently large to quantify the dynamic response of the respective cell types. To determine how cell-(channel) surface interactions vary with respect to the cell types utilized in our studies and with respect to frequency, we measured μ_f (Figure 6-6). We observed no statistical difference among μ_f values for MCF-7 and MCF-10A cells throughout the entire frequency regimes tested. We subsequently treated our channels with Bovine Serum Albumin (BSA) and observed a 1.1% decrease in the mean value of μ_f for both MCF-7 and MCF-10A cells as compared to the untreated control case (Figure 6-6). Based on these results, we concluded that utilizing bare, untreated PDMS devices is appropriate under our given experimental conditions and that cell-

surface interactions, while present, ultimately do not contribute significantly to the quantitative analysis of the cellular viscoelastic properties that our platform performs.

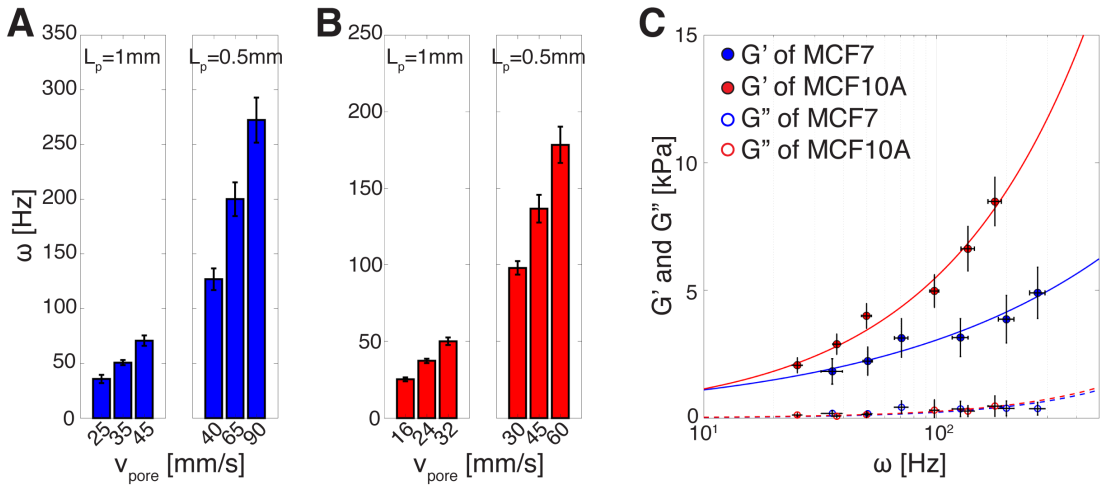

Figure 6-5. Viscoelastic properties of breast epithelial cells. A and **B**, Deformation frequency (ω) of **A**, MCF-7 and **B**, MCF-10A cells (n=100 for all cases). L_p and v_{pore} correspond to the period of the contraction channel length and the flow velocity at the pore prior to the contraction channel, respectively. By changing L_p and v_{pore}, we can adjust the ω with which cells experience in the contraction channel. Error bar represents standard deviation. **C**, Storage (G', solid circle) and loss (G", empty circle) modulus of MCF-7 and MCF-10A cells (n=100 for all cases). Solid and dashed lines indicate the power-law structural damping model (Equation (2.11)) of the storage and loss modulus with respect to deformation frequency (ω), respectively. MCF-7 cells have a smaller power-law exponent (α=0.44±0.006) than MCF-10A cells (α=0.69±0.005). Overall, MCF-10A cells show a greater G' compared to MCF-7 cells. Both cell lines have a much larger G' value as compared to that of G". All error bars in x- and y-axis correspond to standard deviation. *From Ref (32).*

Figure 6-5C shows the storage (G') and loss (G") modulus (i.e. elasticity and viscosity, respectively) of MCF-7 and MCF-10A cells. Throughout the entire frequency range we tested, G' is greater for MCF-10A cells than MCF-7 cells, indicating that these cells are generally stiffer. To investigate the frequency-dependent viscoelastic response of cells, we employed the power-law structural damping model discussed in Chapter 2 (solid and dashed lines in Figure 6-5C). Table 6-4 provides the measured power-law components—G_0 (scaling factor), α (power-law exponent), and μ (Newtonian viscosity)—that we derived from measuring both cell types. As indicated in Table 1, α is much larger for MCF-10A than MCF-7 cells (0.69 vs. 0.44), reflecting the fact that their G' increased more rapidly with deformation frequency. Physically, MCF-10A cells have a far stiffer mechanical response to increasing ω than MCF-7 cells. In regard to viscous behavior, both cell types have exceedingly small G" values as compared to G' throughout the entire frequency regime tested, with MCF-10A cells having a G" value only slightly larger than that of MCF-7 cells. The very small G" values we obtain indicate that both

malignant and nonmalignant breast epithelial cell lines have "solid-like behavior", i.e. they have low viscosity, at the single-cell level. This is remarkably different from that observed at the tissue level, where malignant breast tissue has been shown to exhibit a more viscous response to oscillating stimuli as compared to normal tissue (140).

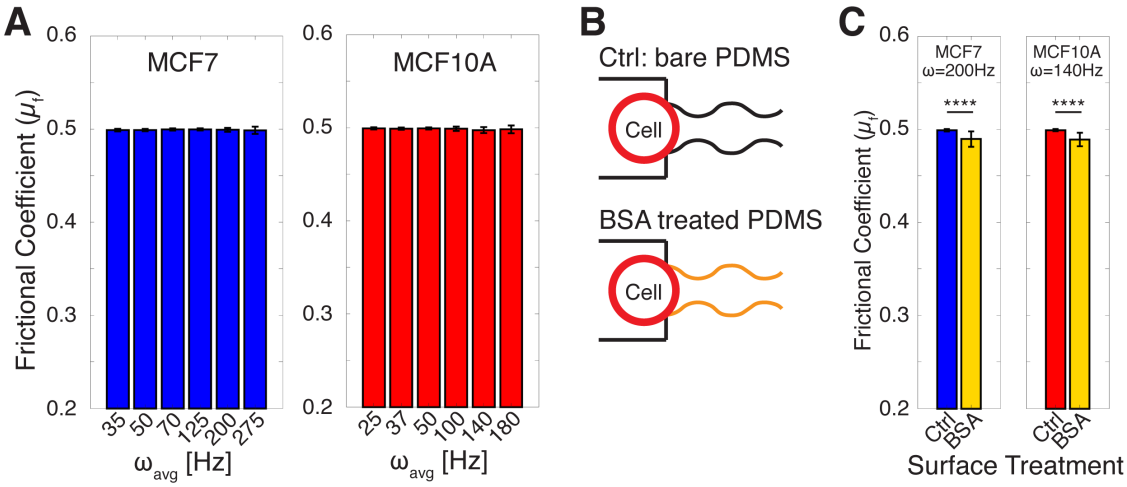

Figure 6-6. Interaction between cell surface and channel wall. A, Measured frictional coefficient (μ_f) of MCF-7 (blue) and MCF-10A (red) cells as they transit through bare PDMS devices (n=100 for all cases). No statistical difference was found in μ_f for both cell types throughout the entire ω regime measured. **B**, Schematic drawing of the experimental conditions (bare PDMS vs. BSA-treated PDMS) used to measure the effects of cell-surface interaction on μ_f. BSA treatment minimizes cellular adhesion to the channel wall. **C**, μ_f of MCF7 and MCF10A cells as they transit through bare PDMS and BSA-treated channels (n=100 for each case). For all graphs, error bar represents standard deviation. **** indicates p≤0.0001. *From Ref (32).*

Table 6-4. Parameters of the power-law structural damping model with corresponding standard error. G_0, α, and μ denote the shear modulus at zero frequency, power-law coefficient, and viscosity, respectively. *From Ref (32).*

	G_0 [Pa]	α	μ [Pa s]
MCF-7	396.42±12.438	0.44±0.006	2.17±0.045
MCF-10A	235.02±5.789	0.69±0.005	2.15±0.074

6.3.2 Contribution of Cytoskeletal Components on Cellular Properties

The cytoskeleton is an important component governing cellular mechanical behavior (141). In order to investigate the individual contributions of cytoskeletal actin filaments and microtubules to the mechanical properties of cells, we analyzed the viscoelastic response of MCF-7 and MCF-10A cells when they were subject to different pharmacological treatments. Specifically, we stabilized actin filaments with Jasplakinlide (Jas, Figure 6-7) and de-activated

them with Latrunculin B (LatB, Figure 6-7). In parallel, we stabilized and destabilized microtubules with Paclitaxel (TAX) and Nocodazole- (Noc), respectively We performed all measurements at ω>100 Hz in order to provide a sufficient window to detect different viscoelastic responses between the two cell types. As shown in Figure 6-8, stabilized actin filaments led to an increased *G*' for both cell types *vs*. the respective controls, indicating that the treated cells had become stiffer. In contrast, de-activated actin filaments led to a decreased *G*' and the treated cells had become softer. With regard to specific cell type, Jas- and LatB-treatment had the strongest effect on *G*' at different frequencies, ω_{avg}=275 Hz for MCF-7 cells and ω_{avg}=100 Hz for MCF-10A cells, indicating that actin filaments have different frequency ranges in which they are actively engaged. The difference in actin-filament behavior between MCF-7 and MCF-10A cells may be a result of their structural and functional differences, which in turn, are correlated with malignancy and metastatic potential (142-144). In terms of cell viscosity, both Jas- and LatB-treated MCF-7 and MCF-10A cells have extremely small values of *G*" as compared to *G*' (Figure 6-9). Interestingly, both Jas- and LatB-treatment enhanced the viscous behavior of MCF-10A cells (noted as larger *G*" values in our data as compared to the control untreated cells, Figure 6-9), but further study is necessary to understand the biological basis of this phenomena.

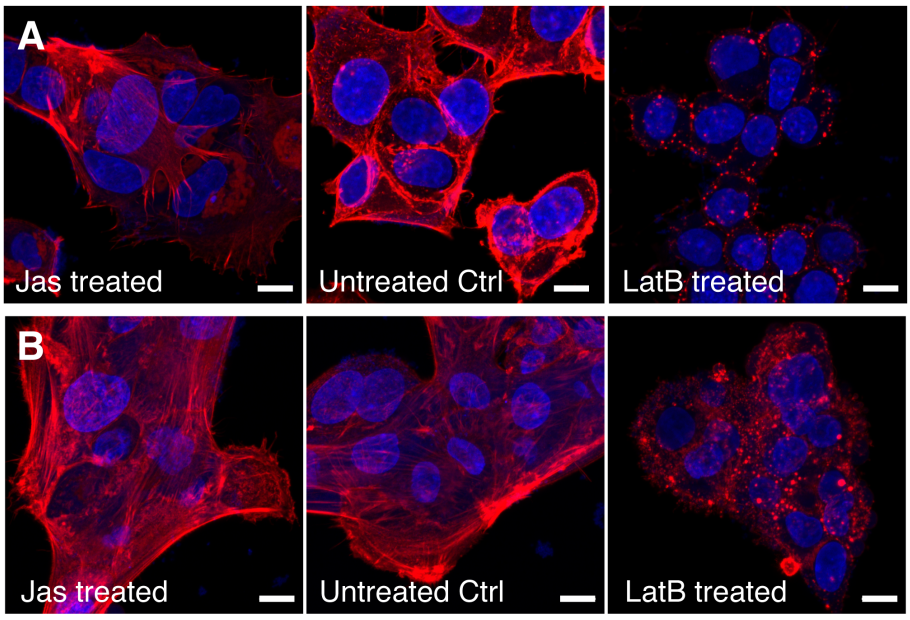

Figure 6-7. Fluorescence images of A, MCF-7 and B, MCF-10A cells after Jasplakinlide (Jas) and Latrunculin B (LatB) treatment. For comparison, fluorescence images of untreated cells (Ctrl) are also included. 4',6-diamidino-2-phenylindole (DAPI, blue) and rhodamine phalloidin (red) were used to stain the cell nucleus and actin filaments, respectively. Scale bar = 10 μm. *From Ref (32).*

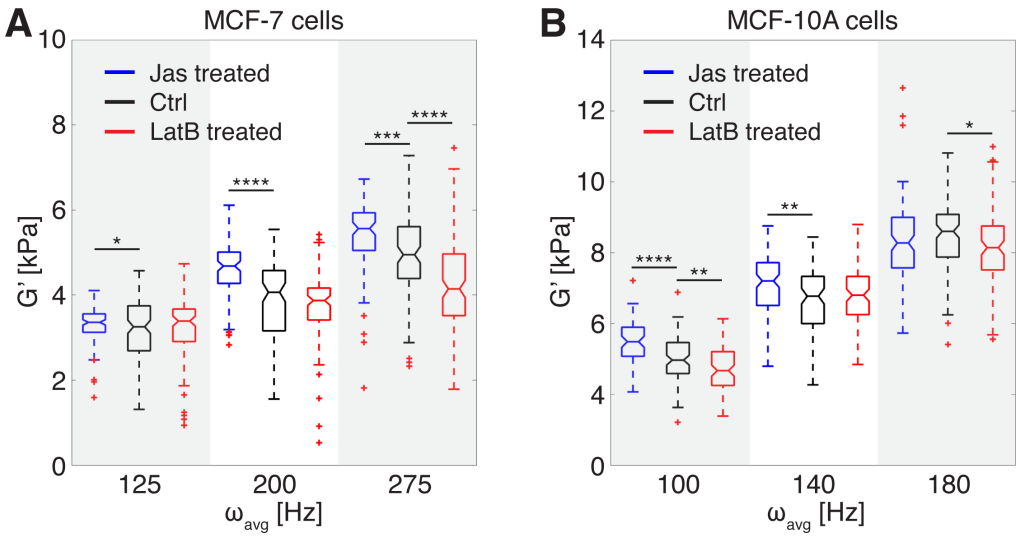

Figure 6-8. Storage modulus (*G'*) of C, treated MCF-7 and D, treated MCF-10A cells per the different ranges of deformation frequency (*ω*) (*n*=100 for all cases). Jas treatment stabilizes actin filaments and LatB treatment de-activates them. Untreated cells were used as a control (Ctrl) case. Statistical differences were determined by an unpaired t-test. Within each box, the central line is the median, the red cross is an outlier, and the edges of the box correspond to 25% and 75% of the population. *, **, ***, and **** indicate $p \leq 0.05$, $p \leq 0.01$, $p \leq 0.001$, and $p \leq 0.0001$, respectively. *From Ref (32).*

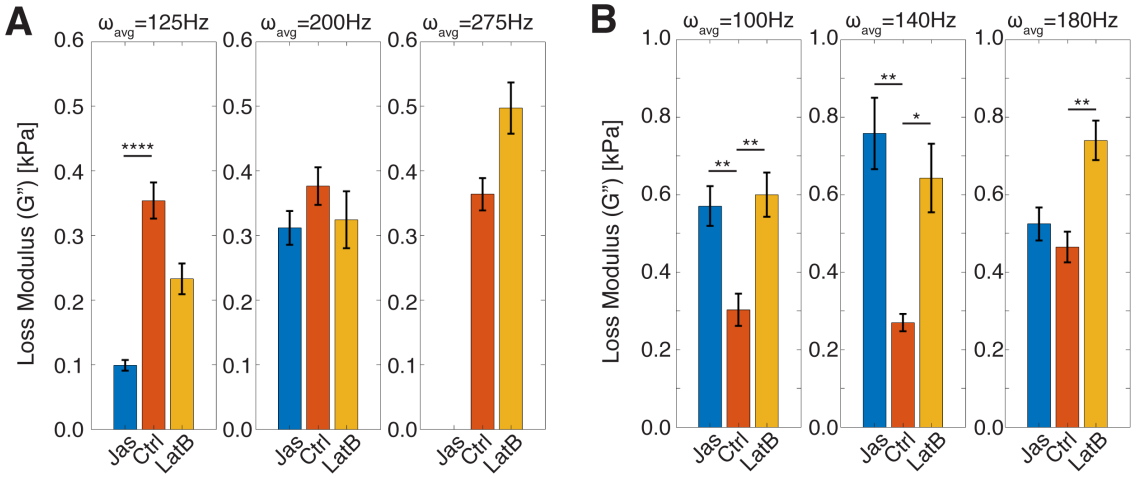

Figure 6-9. Loss modulus (*G"*) of Jas- and LatB-treated A, MCF-7 cells and B, MCF-10A cells compared to untreated (Ctrl) cells (*n*=100 for each case). Jas- and LatB-treatment induce stabilization and de-activation of actin filaments, respectively. ω_{avg} is the average applied deformation frequency. Error bar indicate standard error. *, **, ***, **** correspond $p \leq 0.05$, $p \leq 0.01$, $p \leq 0.001$, $p \leq 0.0001$, respectively. *From Ref (32).*

Figure 6-10 show microtubule structure of MCF-7 and MCF-10A cells after microtubule stabilization and deactivation. While stabilization resulted in an increased *G'* for MCF-7 cells, disruption of microtubule formation led to a reduced *G'* for both cell types throughout all applied frequencies (Figure 6-11). Both pharmacological microtubule treatments on MCF-7 cells showed the most significant effects at ω_{avg}=125 Hz (Figure 6-11A). Noc-treatment, especially, revealed a bipolar effect on elasticity (*G'*) measurements. At ω_{avg}=125 Hz, cells softened, which was reflected in the significantly smaller *G'* values as compared to untreated cells. At ω_{avg}=200 Hz, the difference in *G'* is relatively smaller than other frequencies. At ω_{avg}=275 Hz, *G'* of cells significantly decreased again by Noc-treatment. For MCF-10A cells, disrupting microtubules via Noc-treatments showed stronger effects on cellular elasticity as compared to stabilizing them with TAX-treatment throughout the frequency range we tested (Figure 6-11B). Significantly, at ω_{avg}=180 Hz, the overall values of *G'* for MCF-10A cells decreased by TAX-treatment, in contrast to other frequency conditions. This suggests that the dynamics of cytoskeletal filament formation induce different cellular mechanical behavior of cells and depends on loading conditions, i.e. frequency (141, 145, 146). Similar to our results on the viscosity of cells after Jas- and LatB-treatments, both TAX- and Noc-treated cells showed a much smaller *G"* as compared to *G'* (Figure 6-12), indicating that the cells consistently have a solid-like behavior. Finally, while TAX-treated MCF-7 cells have an increased *G"* in the high frequency range, TAX-treated MCF-10A cells have a decreased *G"* with respect to increasing deformation frequency (Figure 6-12).

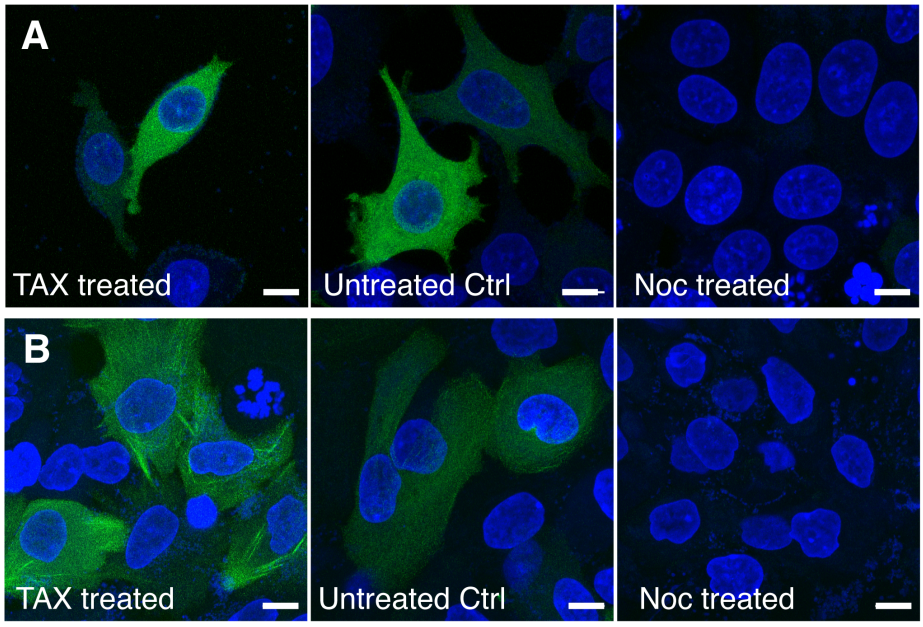

Figure 6-10. Fluorescence images of A, MCF-7 and B, MCF-10A cells after Paclitaxel (TAX) and Nocodazole (Noc) treatment. For comparison, fluorescence images of untreated cells are show as the

control case (Ctrl). DAPI (blue) and green fluorescence protein (GFP, green) stain cell nucleus and tubulin, respectively. Scale bar = 10μm. *From Ref (32).*

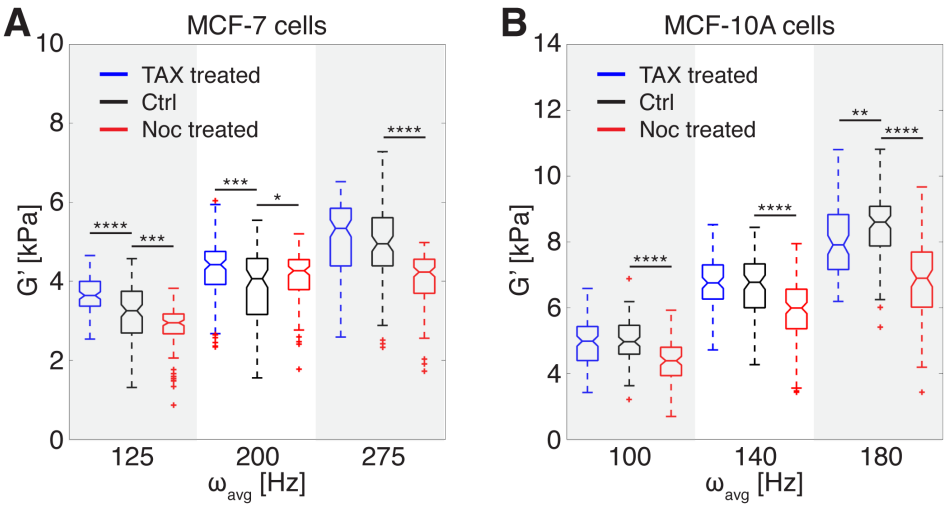

Figure 6-11. Storage modulus (*G'*) of A, treated MCF-7 and B, treated MCF-10A cells with respect to pharmacological treatments per the different range of deformation frequency (*ω*) (*n*=100 for all cases). While TAX treatment stabilizes microtubules, Noc treatment de-activates them. Untreated cells were used as a control (Ctrl) case. Statistical differences were determined by an unpaired t-test. Within each box, the central line is the median, the red cross is an outlier, and the edges of the box correspond to 25% and 75% of the population. *, **, ***, and **** indicate p≤0.05, p≤0.01, p≤0.001, and p≤0.0001, respectively. *From Ref (32).*

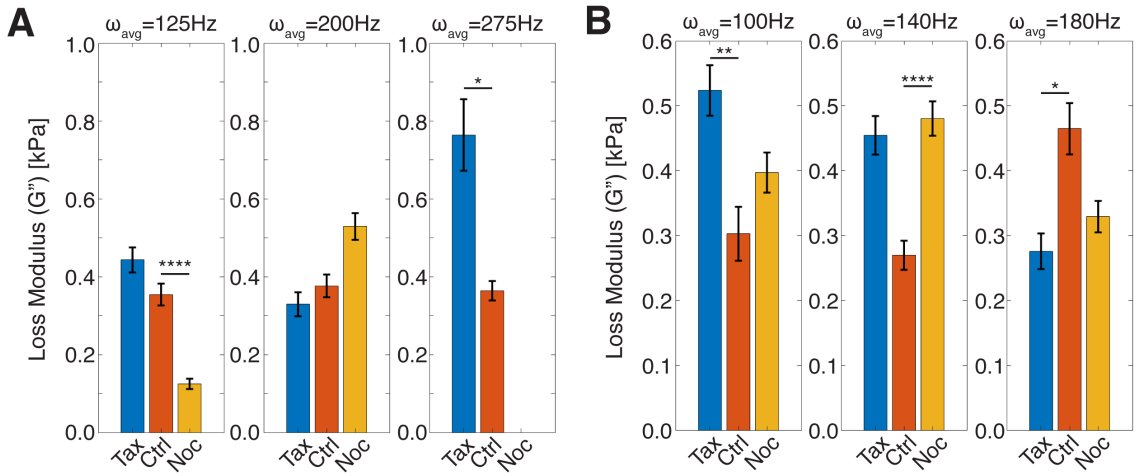

Figure 6-12. Loss modulus (G") of TAX- and Noc-treated A, MCF-7 cells and B, MCF-10A cells compared to untreated (Ctrl) cells (*n*=100 for each case). TAX- and Noc-treatment stabilize and disrupt microtubule formation, respectively. ω_{avg} is the average applied deformation frequency. Error

bar indicate standard error. *, **, ***, **** correspond $p \leq 0.05$, $p \leq 0.01$, $p \leq 0.001$, $p \leq 0.0001$, respectively. *From Ref (32).*

6.3.3 Cellular Mechanical Transition Through Cell-Cycle Phase

Cells experience dramatic changes to their cytoskeleton and nucleus during their cell cycle (147, 148), and correspondingly these changes should induce different cellular mechanical behavior. We thus analyzed the viscoelastic properties of MCF-7 cells that were synchronized in their cell-cycle via a double thymidine block and release protocol and evaluated the effects of actin-filament de-activation during each cell-cycle phase. Figure 6-13 show the morphological changes that MCF-7 cells undergo as they progress through the different cell-cycle phases, from G1- to S- to G2- to M-phase. As expected, the relative size of the nuclei increases during S-phase and stained nuclei show the classic spike shape of mitosis in M-phase. By immunostaining nuclear DNA, we validated cell synchronization and confirmed that DNA content increased as the cells traversed their cell cycle (Figure 6-13B). We screened synchronized MCF-7 cells with visco-NPS at $\omega = 200$ Hz. Our results show that G' of MCF-7 cells clearly increases as the they go from G1- to S- to G2-phase. As the cells progress from G2- to M- back to G1-phase, there is a significant decrease in G' (Figure 6-14A). Our results show that the elasticity of MCF-7 cells is highly dependent on cell-cycle phase. Cells have the stiffest mechanical response in G2-phase, suggesting that the nucleus and cytoskeletal filaments in this phase are mechanically the most stable as compared to in all other phases.

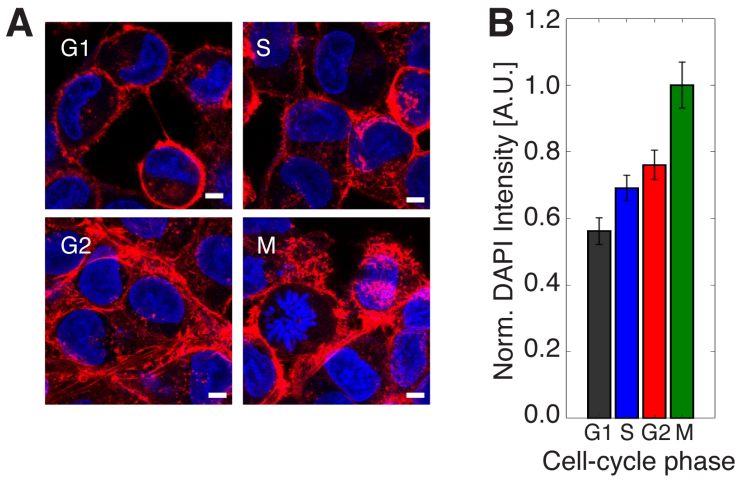

Figure 6-13. Cell cycle synchronization. A, Representative fluorescence images of MCF-7 cells in each cell-cycle phase. 4',6-diamidino-2-phenylindole (DAPI, blue) and rhodamine phalloidin (red) stain the cell nucleus and actin filaments, respectively. Scale bar = 5μm. **B**, Normalized DAPI intensity of MCF-7 cells with respect to cell cycle phases (G1 phase; n=482, S phase; n=592, G2 phase; n=437, and M phase; n=512). The condensation of nucleus DNA into chromosome structures during M-phase resulted in the strongest DAPI intensity. Error bars represent standard deviation. *From Ref (32).*

To analyze the contribution of the nucleus to the viscoelastic properties measured, we depolymerized actin filaments in each cell-cycle phase via LatB treatment. In general, we measured lower *G'* values vs. untreated cells, indicating that the cells had softened. Similar to our result on cellular elasticity, LatB-treated cells also showed the largest *G'* value in G2 phase (Figure 6-14A). We evaluated the statistical difference among all experimental conditions based on correlation coefficient (*rho*) and *p* values (Table 6-5). G1+LatB *vs.* G2+LatB, G2+LatB *vs.* M, S+LatB *vs.* M+LatB, G2 *vs.* M+LatB, and G2+LatB *vs.* M+LatB showed significant statistical difference. From this, we conclude that the cell nucleus in G1-, G2-, and M-phase has a strong effect on cellular elasticity. To quantify the statistical effect of the two variables, i.e. cell-cycle phase and LatB treatment, we performed a two-way ANOVA test and showed that both cell-cycle phase (p=6.781e-8) and LatB treatment (p=6.806e-37) had a statistically significant effect on the *G'* of MCF-7 cells. In addition, the interaction of these two variables also had a significant effect on the *G'* of MCF-7 cells (p=6.781e-8). Cellular viscosity (*G"*) showed a trend similar to elasticity (*G'*) regarding cell-cycle phase and LatB treatment. MCF-7 cells in G2-phase exhibited the largest *G"* value in both untreated and LatB treated groups (Figure 6-14B). As well, the perturbation of actin filament by LatB treatment resulted in a decrease in *G"* compared to untreated cells during each cell-cycle phase.

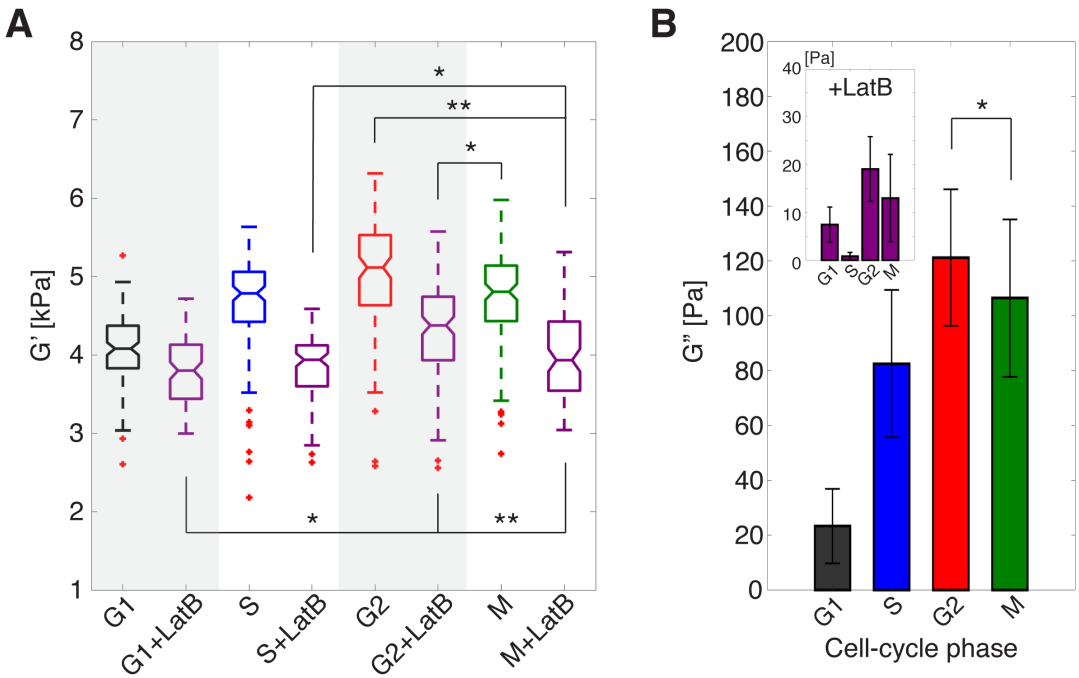

Figure 6-14. Viscoelastic properties of untreated and LatB treated cells at each cell cycle phase. **A,** Storage modulus (*G'*) of untreated and LatB-treated (purple) MCF-7 cells throughout the different cell-cycle phases, as measured with a 200 Hz deformation frequency (n=100 for all cases). The individual and combined statistical effects of LatB treatment and cell-cycle phases were determined by a two-way ANOVA test. Both LatB treatment (p=6.806e-37) and cell-cycle phases (p=1.132e-32) have significant statistical effects on change of *G'*. The interaction of those two factors also shows a significant statistical effect on *G'* as having low p-value (p=6.781e-8). Within each box, the central line is the

median, the red cross is an outlier, and the edges of the box correspond to 25% and 75% of the population. **B**, Loss modulus (G") of untreated and LatB-treated (inset) MCF-7 cells throughout the different cell cycle phases with ω_{avg}=200 Hz (n=100 for all cases). Error bars represent standard error. For all graphs, * and ** indicate p≤0.05 and p≤0.01, respectively. *From Ref (32).*

Table 6-5. Correlation coefficient (rho) and *p*-value between storage modulus (*G*') of each experimental case. Larger ρ value indicates more highly correlated relationship between the cases. G1, S, G2, M, and LatB denote Gap1, Synthesis, Gap2, Mitosis phase, and Latrunculin B treatment, respectively. * and ** indicate p≤0.05 and p≤0.01, respectively. *From Ref (32).*

vs.	G1	G1+LatB	S	S+LatB	G2	G2+LatB	M	M+LatB
G1	N.A.	rho=-0.050 p=0.631	rho=-0.122 p=0.242	rho=0.010 p=0.925	rho=-0.071 p=0.502	rho=0.181 p=0.083	rho=0.098 p=0.349	rho=-0.059 p=0.576
G1+LatB		N.A.	rho=0.053 p=0.611	rho=0.170 p=0.104	rho=0.149 p=0.155	rho=0.259 *p=0.012	rho=-0.079 p=0.455	rho=0.193 p=0.063
S			N.A.	rho=-0.032 p=0.764	rho=0.036 p=0.731	rho=-0.064 p=0.542	rho=0.201 p=0.053	rho=-0.102 p=0.332
S+LatB				N.A.	rho=0.016 p=0.875	rho=0.197 p=0.058	rho=0.054 p=0.607	rho=0.228 *p=0.028
G2					N.A.	rho=0.062 p=0.557	rho=0.023 p=0.828	rho=0.304 **p=0.003
G2+LatB						N.A.	rho=0.221 *p=0.033	rho=0.286 **p=0.006
M							N.A.	rho=0.030 p=0.772
M+LatB								N.A.

6.4 Discussion

Visco-NPS enables the analysis of populations of single cells for their viscoelastic properties. By combining a sinusoidal contraction channel with NPS (15) (or mechano-NPS (31)), we can quantify the mechanical response of cells as they periodically deform. Based on just two mechanical properties, storage (elasticity) and loss (viscosity) modulus, malignant and non-malignant breast epithelial cells show distinctly different viscoelastic behavior and frequency-dependent responses to dynamic loading conditions. Overall, both types of cells exhibit a lower viscosity as compared to elasticity for all measured frequencies (10~300 Hz). In contrast, most AFM measurements show that cell viscosity values increase beyond those of elasticity at a threshold frequency (80, 128, 149). The difference between our measurements and those of AFM may be due to the fact that while the AFM measures cellular sub-regions, visco-NPS measures the whole-cell. Moreover, AFM measurements are performed on cells that have been adhered to substrates, whereas visco-NPS measurements are performed on detached cells,

which eliminates the influence of external factors, e.g. substrate stiffness, that can influence cell behavior. As we have shown, visco-NPS can determine the individual contributions of cytoskeletal components, such as actin filaments and microtubules, to cellular viscoelastic properties. Furthermore, through pharmacological treatments, in which we stabilized or de-activated cytoskeletal filaments or microtubules, visco-NPS can quantitatively measure the subsequent effects on the elasticity and viscosity of the treated cells. Treated malignant and non-malignant cells show distinct frequency-dependent elastic responses within a range of 100~275 Hz. Finally, visco-NPS has sufficient sensitivity to measure the change in mechanical properties of cells as they traverse their cell-cycle. In general, visco-NPS provides a comprehensive understanding of the dynamic mechanical behavior of cells at the single-cell level.

Attractive features of visco-NPS include that it is label-free, does not require a high-speed camera or advanced fluidics, and has high-throughput capability. Its simplicity allows it be combined potentially with other cell analyses, including cell-surface marker screening (16) and single-cell whole-transcriptome analysis (150-152). This, in particular, would provide opportunities to correlate mechanical properties with biochemical properties. The design flexibility of visco-NPS allows us to utilize a variety of experimental conditions, models, and mechanical tests for further studies. By varying the width and period of our sinusoidal contraction channel, one can apply different levels of strain to, and can access different frequency regimes in which to measure, cells. Contraction channels with different periodic lengths placed in series would allow one to measure a single cell at multiple deformation frequencies. In so doing, one can determine the frequency-dependence of the cell's viscoelastic properties, which ultimately would provide a more in-depth understanding of cellular mechanical properties at the single-cell level.

While we have focused on the power-law structural damping model, other mechanical models (36) are applicable to this platform. For example, cortical shell-liquid core (153), linear viscoelastic solid (154, 155), and biphasic models (156, 157) could all be applied to different cell types and their corresponding biophysical function. By modifying the microfluidic channel design, one can perform different types of mechanical tests. For example, one could perform a mechanical creep test by applying a constant compressive stress to the deformed cells through pneumatic side channels positioned parallel to the sides of the sinusoidal contraction channel. Such a test could provide an understanding of the biophysical relationship between mechanical properties and cell recovery characteristics (158). Even in its present form, visco-NPS, can successfully measure the viscoelastic properties of cells under various biological conditions, as we have demonstrated here.

Cellular mechanics is an emerging area of research, especially, within the context of cancer (115, 159, 160). Quantifying the viscoelastic properties of cell populations, visco-NPS introduces new possibilities in basic biology and clinical applications, such as cancer diagnosis, cytoskeleton-targeted drug screening, and studies for cell cycle as a therapeutic target of cancer.

By combining the clear relationship between malignancy and viscoelastic properties of cells with numerous features of our platform (e.g. label-free analysis and high throughput capability), visco-NPS can be used as a cancer screening and diagnostic tool, especially for those cancer cells, e.g. triple-negative breast cancer, that are otherwise difficult to identify with traditional methods (161-163). As it can quantify the contribution of cytoskeletal filaments to whole-cell mechanical properties, visco-NPS could be employed as a screening method for the cytoskeleton-targeted drugs that are often used in cancer therapies (164-166). Recently, a number of studies have been shown that cell-cycle pathways such as, regulation of CDK (cyclin-dependent kinases), ATM (ataxiatelangiectasia mutated), and ATR (AMT- and Rad3-related) lead to aberrant cell proliferation and are critical to carcinogenesis (167-170). By analyzing the cellular mechanical transitions during the cell cycle and quantifying the mechanical properties of actin filaments as they are perturbed during each phase, visco-NPS may yield a new approach to the development of cancer therapies that target these, and other, cell-cycle pathways.

In summary, visco-NPS introduces a novel microfluidic approach to analyze cellular viscoelastic properties, and consequently, provides a tremendous potential for both biophysical studies of cellular behavior and clinical applications.

7 CONCLUSION AND FUTURE RESEARCH

Chapter Overview

This chapter summarizes the results of the dissertation research and provides an overall conclusion and recommendations for future research. Major findings on single-cell mechanics via mechano-NPS and visco-NPS are reviewed. Based on the summarized results, this chapter proposes a number of directions for future research regarding cellular mechanics.

7.1 Summary and Findings

In this dissertation, I have described microfluidic approaches for single-cell mechanics. The electronic-based mechanical phenotyping platform, mechano-NPS, enables one to discriminate cell lineage, chronological age, and stage of malignant progression in hMECSs. Employing a rheological approach, I also developed a new microfluidic platform, visco-NPS, to measure the viscoelastic properties of cells. Visco-NPS successfully quantifies elasticity and viscosity of cells and evaluates the effects of malignancy, cytoskeletal structure, and cellular transitions that occur throughout the cell cycle on whole-cell mechanical properties.

In Chapters 4 and 5, I demonstrated mechano-NPS, a multi-parametric single-cell analysis method and its applications on biological and pre-clinical studies. Integrating the contraction channel with NPS, I was able to quantify multiple biophysical properties of cells simultaneously. To minimize cell-size effects on other biophysical properties, I normalized the measured properties and defined a new dimensionless parameter, the whole-cell deformability index (*wCDI*). The *wCDI* provides a quantitative mechanical metric of the resistance to compressive deformation. Based on the *wCDI* and transverse deformation of cells, mechano-NPS shows malignant MCF-7 and A549 cell lines have mechanically distinct characteristics compared to non-malignant MCF-10A and BEAS-2B cell lines. Using these parameters, I also evaluated the contribution of actin filaments to whole-cell mechanical phenotypes. Screening cells through mechano-NPS provides a new information regarding cellular recovery after compressive deformation. In Chapter 5, I demonstrated that mechano-NPS can discriminate between sub-lineages of normal primary hMECs; these sub-lineages have distinct roles in carcinogenesis in mammary tissue. My results show that mechano-NPS identifies lineage, chronological age, and stage of malignant progression in hMECs—all solely based on cellular mechanical phenotypes.

In Chapter 6, I introduced a new microfluidic rheology platform, visco-NPS, which quantifies viscoelastic properties of cells under periodic deformation. In visco-NPS, the contraction channel has a periodically changing width which correspondingly induces periodic deformation in a cell traversing it. As such, the elasticity and viscosity of cells through the

storage (G') and loss (G'') modulus can be measured. Visco-NPS also can evaluate the frequency-dependence of cellular viscoelastic properties by applying a wide range of deformation frequencies to a cell population. Rheological measurements through visco-NPS show that the malignant breast epithelial cell line, MCF-7, has distinctly different viscoelastic properties as compared to the non-malignant breast epithelial cell line, MCF-10A. The sensitivity of visco-NPS allowed us to evaluate the individual contributions of different cytoskeletal filaments (actin filaments and microtubules) to whole-cell mechanical properties. The measurements of G' and G'' also show that visco-NPS can measure the mechanical transitions that cells undergo as they transverse the different phases of the cell cycle.

7.2 Future Research

This dissertation has presented two robust, flexible, and powerful mechanical phenotyping platforms for cellular mechanics at the single-cell level. Based on these platforms, future work could be performed to increase their value. First, higher throughput could be achieved by employing advanced signal processing. For both mechano- and visco-NPS platforms, current pulses generated by coincidence events, in which multiple cells occupy the channel simultaneously, are presently removed due to their complexity in signal identification. More robust signal-processing algorithms, such as match filtering, Barker codes, and Gold sequences, could be used to overcome this challenge (93, 171-173). Second, multiplexing strategies, e.g. parallelizing multiple mechano- and visco-NPS, could easily increase throughput of the two platforms to ~1000 cells/min.

The simplicity and flexibility of mechano- and visco-NPS allow one to customize these platforms for other types of biomechanical studies. By employing microfluidic cell separation techniques such as Deterministic Lateral Displacement (DLD) and inertial focusing, we can pre-screen cells based on their size (174-177). This pre-screening would overcome the intrinsic measurement errors generated from the size variance within a cell population, since identical mechanical deformation or forces could be applied to the cells. In addition, it can be used to minimize sample preparation steps and to screen specific cell types within heterogenous cell populations, such as that found in whole blood. We also can integrate other downstream analysis to study the correlation between cellular mechanical characteristics and other biological functions. For example, the integration of cell-surface marker profiling (16) and single-cell genome sequencing (150, 152) would provide new information about how cellular mechanical phenotypes are correspond to specific surface marker and gene expression of cells, respectively. Although this dissertation focuses on mechanical phenotyping at the single cell level, mechano- and visco-NPS can easily be customized for analyzing biological tissues and cell-to-cell interaction. As an example, by expanding the overall dimension of the contraction channel, one can use mechano-NPS enable to measure the mechanical phenotypes of whole cell spheroids. Combined with single-cell mechanical phenotyping, this approach could allow

one to analyze the mechanical characteristics of individual cells, cell-to-cell interactions, and tissue-level structure.

Cellular mechanics is a nascent and emerging area of cancer research. Characterizing mechanical phenotypes through mechano- and visco-NPS opens up new possibilities in basic biology and clinical applications. As they can quantify the roles of cytoskeletal components in whole-cell mechanical properties, these two platforms can be potentially used for development of cytoskeleton-targeted cancer treatment. The ability of these platforms for rapid characterization lend themselves to various applications for cancer screening and diagnostics. For example, identifying subpopulations in the mammary epithelium and analyzing its relationship with age of women through mechano-NPS may yield valuable information regarding breast-cancer risk. Combined with the fact that cell-cycle pathways have critical roles in cancer proliferation and carcinogenesis, analyzing mechanical transitions via visco-NPS may yield a new approach to the development of cancer therapies targeting cell-cycle pathways. Furthermore, the rapid analysis of mechano- and visco-NPS can be used to develop patient specific cancer treatment by analyzing the drug response of patient-derived cells and organoids.

Mechanical characterization of cells also provides clinical metric to detect cellular transitions such as epithelial-mesenchymal transition (EMT) (122, 178) and tissue growth potential (179, 180). In regard to EMT, mechanical phenotyping can lead to new information regarding this process. To show this, we induced EMT in normal breast epithelial (MCF10A) cells by the overexpression of the E-cadherin transcriptional repressor, SLUG (32). Figure 7-1 shows that mechano-NPS can detect the differences in mechanical phenotypes of MCF10A cells and EMT-induced (+SLUG) cells. Overall, EMT-induced cells are more deformable and take longer time to restore their original size after release from compressive deformation. These findings suggest that cells experience significant changes in their cytoskeletal or nuclear structure through EMT. Based on the strong correlation between EMT and tumor metastasis (181, 182), mechanical phenotyping could provide a new way to understand the underlying mechanism of cancer-related cellular transitions.

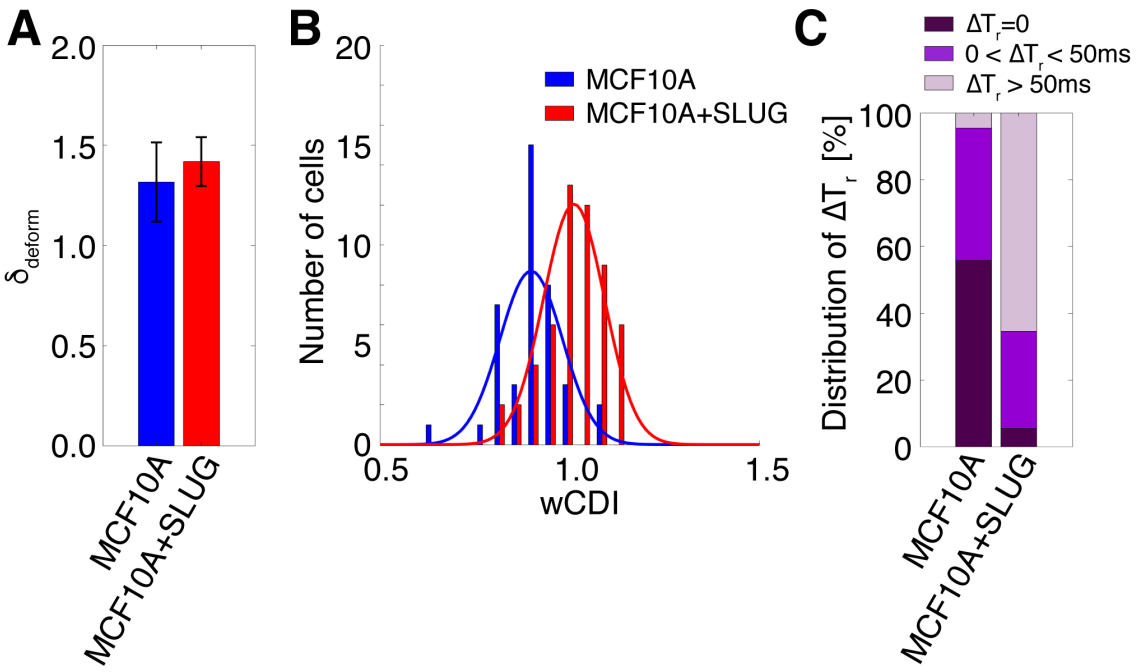

Figure 7-1. Mechanical phenotypes of normal breast epithelial cells and EMT-induced cells. A, Transverse deformation of normal MCF10A (blue) and SLUG+ MCF10A (red) cells (n=100 per each case). An E-cadherin transcriptional repressor, SLUG, was overexpressed in MCF10A cells to induce EMT. Error bars represent standard deviation. **B**, *wCDI* of MCF10A and overexpressed SLUG MCF10A cells. Overall, overexpressed SLUG+ MCF10A cells show greater *wCDI* values, indicating that EMT leads to softer mechanical phenotypes. **C**, Distribution of instant (ΔT_r~0,), transient ($0<\Delta T_r\leq 50$ ms), or prolonged ($\Delta T_r>50$ ms) recovery within MCF10A and overexpressed SLUG MCF10A cell populations.

Characterizing mechanical phenotypes at the single-cell level also can be used to evaluate tissue-regeneration potential of cells. We employed mechano-NPS to measure mechanical phenotypes of Nucleus Pulposus (NP) cells, obtained from Prof. Grace O'Connell, with respect to culture conditions (primed vs unprimed) and passages. As shown in Figure 7-2, depending on passage number and culture conditions, the mechanical phenotypes of NP cells can change. These preliminary results suggest that culture conditions and passage can have significant effects on cell mechanical properties, which in turn could affect the tissue-growth potential (180). Thus, single-cell mechanical phenotyping could provide a new method to pre-screen cells for tissue regeneration.

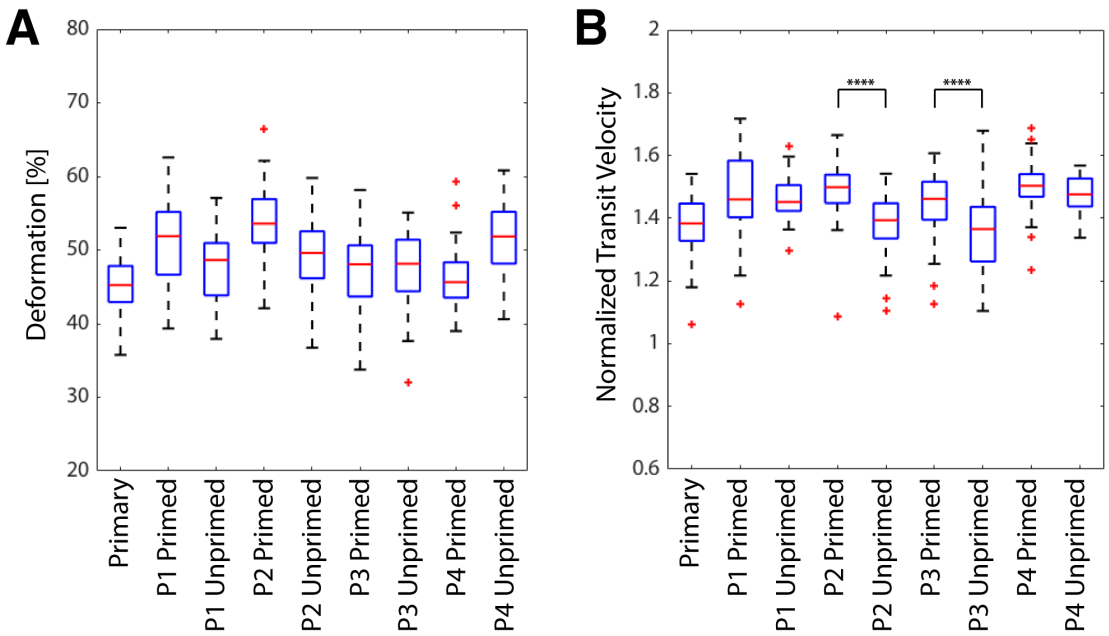

Figure 7-2. Mechanical phenotypes of Nucleus Pulposus cells with respect to culture conditions and passages. A, Deformation of primed and unprimed NP cells from primary to passage 4 (*n*=100 per each case) compared to their original size. Statistical differences were determined by an unpaired t-test. Within each box, the central line is the median, the red cross is an outlier, and the edges of the box correspond to 25% and 75% of the population. **** indicates p≤0.0001. **B**, Normalized transit velocity of primed and unprimed NP cells passing through an 8μm-wide contraction channel (via a 21 kPa non-pulsatile pressure applied to the device inlet). The transit velocity within the contraction channel is normalized by the cell velocity in the pore region, prior to the contraction channel. Statistical differences were determined by an unpaired t-test. Within each box, the central line is the median, the red cross is an outlier, and the edges of the box correspond to 25% and 75% of the population. **** indicates p≤0.0001.

Throughout this dissertation, I have demonstrated that mechano- and visco-NPS are powerful platforms that can identify the effects of cellular lineage, malignant progression, chronological age, cytoskeletal structure, and cellular transitions that occur throughout the cell-cycle. Moreover, I have shown that cellular mechanical phenotyping at the single-cell level, overall, has tremendous potential for biomedical and biological research and for clinical applications.

Bibliography

1. Li Q, Lee G, Ong C, Lim C. AFM indentation study of breast cancer cells. Biochemical and biophysical research communications. 2008;374(4):609-13.
2. Cross SE, Jin Y-S, Tondre J, Wong R, Rao J, Gimzewski JK. AFM-based analysis of human metastatic cancer cells. Nanotechnology. 2008;19(38):384003.
3. Rother J, Nöding H, Mey I, Janshoff A. Atomic force microscopy-based microrheology reveals significant differences in the viscoelastic response between malign and benign cell lines. Open biology. 2014;4(5):140046.
4. Hochmuth RM. Micropipette aspiration of living cells. Journal of biomechanics. 2000;33(1):15-22.
5. Zhou E, Quek S, Lim C. Power-law rheology analysis of cells undergoing micropipette aspiration. Biomechanics and modeling in mechanobiology. 2010;9(5):563-72.
6. Lee LM, Liu AP. The application of micropipette aspiration in molecular mechanics of single cells. Journal of nanotechnology in engineering and medicine. 2014;5(4):040902.
7. Darling EM, Di Carlo D. High-throughput assessment of cellular mechanical properties. Annual review of biomedical engineering. 2015;17:35-62.
8. Dai J, Sheetz MP. Mechanical properties of neuronal growth cone membranes studied by tether formation with laser optical tweezers. Biophysical journal. 1995;68(3):988-96.
9. Tan Y, Sun D, Wang J, Huang W. Mechanical characterization of human red blood cells under different osmotic conditions by robotic manipulation with optical tweezers. IEEE Transactions on biomedical engineering. 2010;57(7):1816-25.
10. Thoumine O, Ott A, Cardoso O, Meister J-J. Microplates: a new tool for manipulation and mechanical perturbation of individual cells. Journal of biochemical and biophysical methods. 1999;39(1-2):47-62.
11. Gossett DR, Henry T, Lee SA, Ying Y, Lindgren AG, Yang OO, et al. Hydrodynamic stretching of single cells for large population mechanical phenotyping. Proceedings of the National Academy of Sciences. 2012;109(20):7630-5.
12. Byun S, Son S, Amodei D, Cermak N, Shaw J, Kang JH, et al. Characterizing deformability and surface friction of cancer cells. Proceedings of the National Academy of Sciences. 2013;110(19):7580-5.
13. Otto O, Rosendahl P, Mietke A, Golfier S, Herold C, Klaue D, et al. Real-time deformability cytometry: on-the-fly cell mechanical phenotyping. Nature methods. 2015;12(3):199.
14. Xavier M, Rosendahl P, Herbig M, Kräter M, Spencer D, Bornhäuser M, et al. Mechanical phenotyping of primary human skeletal stem cells in heterogeneous populations by real-time deformability cytometry. Integrative Biology. 2016;8(5):616-23.

15. Balakrishnan KR, Anwar G, Chapman MR, Nguyen T, Kesavaraju A, Sohn LL. Node-pore sensing: a robust, high-dynamic range method for detecting biological species. Lab on a Chip. 2013;13(7):1302-7.
16. Balakrishnan KR, Whang JC, Hwang R, Hack JH, Godley LA, Sohn LL. Node-pore sensing enables label-free surface-marker profiling of single cells. Analytical chemistry. 2015;87(5):2988-95.
17. Bull B, Schneiderman M, Brecher G. Platelet counts with the Coulter counter. American journal of clinical pathology. 1965;44(6):678-88.
18. Koch M, Evans A, Brunnschweiler A. Design and fabrication of a micromachined Coulter counter. Journal of micromechanics and microengineering. 1999;9(2):159.
19. Bayley H, Martin CR. Resistive-pulse sensing from microbes to molecules. Chemical Reviews. 2000;100(7):2575-94.
20. Jagtiani AV, Carletta J, Zhe J. A microfluidic multichannel resistive pulse sensor using frequency division multiplexing for high throughput counting of micro particles. Journal of Micromechanics and Microengineering. 2011;21(6):065004.
21. Zhou K, Li L, Tan Z, Zlotnick A, Jacobson SC. Characterization of hepatitis B virus capsids by resistive-pulse sensing. Journal of the American Chemical Society. 2011;133(6):1618-21.
22. Akpinar F, Yin J. Characterization of vesicular stomatitis virus populations by tunable resistive pulse sensing. Journal of virological methods. 2015;218:71-6.
23. Sun T, Morgan H. Single-cell microfluidic impedance cytometry: a review. Microfluidics and Nanofluidics. 2010;8(4):423-43.
24. DeBlois R, Bean C. Counting and sizing of submicron particles by the resistive pulse technique. Review of Scientific Instruments. 1970;41(7):909-16.
25. Gregg EC, Steidley KD. Electrical counting and sizing of mammalian cells in suspension. Biophysical journal. 1965;5(4):393.
26. DeBlois RW, Bean CP, Wesley RK. Electrokinetic measurements with submicron particles and pores by the resistive pulse technique. Journal of colloid and interface science. 1977;61(2):323-35.
27. Smythe W. Flow around a sphere in a circular tube. The Physics of Fluids. 1961;4(6):756-9.
28. Smythe W. Flow around a spheroid in a circular tube. The Physics of Fluids. 1964;7(5):633-8.
29. Saleh OA. A novel resistive pulse sensor for biological measurements: Princeton University Princeton, NJ; 2003.
30. Misic T, Najdanovic-Lukic M, Nesic L. Dimensional analysis in physics and the Buckingham theorem. European Journal of Physics. 2010;31(4):893.
31. Kim J, Han S, Lei A, Miyano M, Bloom J, Srivastava V, et al. Characterizing cellular mechanical phenotypes with mechano-node-pore sensing. Microsystems & nanoengineering. 2018;4:17091.

32. Kim J, Kim Y, Li B, Sohn LL. Visco-Node-Pore Sensing: An Electronic-Based Microfluidic Rheology Platform to Characterize Viscoelastic Properties of Epithelial Cells. iScience 2019;[In revision].
33. Fabry B, Maksym GN, Butler JP, Glogauer M, Navajas D, Fredberg JJ. Scaling the microrheology of living cells. Physical review letters. 2001;87(14):148102.
34. Unal M, Alapan Y, Jia H, Varga AG, Angelino K, Aslan M, et al. Micro and nano-scale technologies for cell mechanics. Nanobiomedicine. 2014;1(Godište 2014):1-5.
35. Pritz T. Analysis of four-parameter fractional derivative model of real solid materials. Journal of Sound and Vibration. 1996;195(1):103-15.
36. Lim C, Zhou E, Quek S. Mechanical models for living cells—a review. Journal of biomechanics. 2006;39(2):195-216.
37. Swaminathan V, Mythreye K, O'Brien ET, Berchuck A, Blobe GC, Superfine R. Mechanical stiffness grades metastatic potential in patient tumor cells and in cancer cell lines. Cancer research. 2011;71(15):5075-80.
38. Xu W, Mezencev R, Kim B, Wang L, McDonald J, Sulchek T. Cell stiffness is a biomarker of the metastatic potential of ovarian cancer cells. PloS one. 2012;7(10):e46609.
39. Brunet S, Maro B. Cytoskeleton and cell cycle control during meiotic maturation of the mouse oocyte: integrating time and space. Reproduction. 2005;130(6):801-11.
40. Needham D. Possible role of cell cycle-dependent morphology, geometry, and mechanical properties in tumor cell metastasis. Cell biophysics. 1991;18(2):99-121.
41. Mundel P, Reiser J, Borja AZMa, Pavenstädt H, Davidson GR, Kriz W, et al. Rearrangements of the cytoskeleton and cell contacts induce process formation during differentiation of conditionally immortalized mouse podocyte cell lines. Experimental cell research. 1997;236(1):248-58.
42. González-Cruz RD, Fonseca VC, Darling EM. Cellular mechanical properties reflect the differentiation potential of adipose-derived mesenchymal stem cells. Proceedings of the National Academy of Sciences. 2012;109(24):E1523-E9.
43. Bagnall JS, Byun S, Miyamoto DT, Kang JH, Maheswaran S, Stott SL, et al. Deformability-based cell selection with downstream immunofluorescence analysis. Integrative Biology. 2016;8(5):654-64.
44. Bongiorno T, Chojnowski JL, Lauderdale JD, Sulchek T. Cellular stiffness as a novel stemness marker in the corneal limbus. Biophysical journal. 2016;111(8):1761-72.
45. Lee WC, Shi H, Poon Z, Nyan LM, Kaushik T, Shivashankar G, et al. Multivariate biophysical markers predictive of mesenchymal stromal cell multipotency. Proceedings of the National Academy of Sciences. 2014;111(42):E4409-E18.
46. Cerchiari AE, Garbe JC, Jee NY, Todhunter ME, Broaders KE, Peehl DM, et al. A strategy for tissue self-organization that is robust to cellular heterogeneity and plasticity. Proceedings of the National Academy of Sciences. 2015;112(7):2287-92.
47. Zheng Y, Nguyen J, Wei Y, Sun Y. Recent advances in microfluidic techniques for single-cell biophysical characterization. Lab on a Chip. 2013;13(13):2464-83.

48. Kirschenbaum LA, Aziz M, Astiz ME, Saha DC, Rackow EC. Influence of rheologic changes and platelet–neutrophil interactions on cell filtration in sepsis. American journal of respiratory and critical care medicine. 2000;161(5):1602-7.
49. Starodubtseva MN. Mechanical properties of cells and ageing. Ageing Research Reviews. 2011;10(1):16-25.
50. Zhou Z, Zheng C, Li S, Zhou X, Liu Z, He Q, et al. AFM nanoindentation detection of the elastic modulus of tongue squamous carcinoma cells with different metastatic potentials. Nanomedicine: Nanotechnology, Biology and Medicine. 2013;9(7):864-74.
51. Hogan B, Babataheri A, Hwang Y, Barakat AI, Husson J. Characterizing Cell Adhesion by Using Micropipette Aspiration. Biophysical journal. 2015;109(2):209-19.
52. Lee LM, Liu AP. A microfluidic pipette array for mechanophenotyping of cancer cells and mechanical gating of mechanosensitive channels. Lab on a Chip. 2015;15(1):264-73.
53. Wang A, Vijayraghavan K, Solgaard O, Butte MJ. Fast stiffness mapping of cells using high-bandwidth atomic force microscopy. ACS nano. 2015;10(1):257-64.
54. Li J, Dao M, Lim C, Suresh S. Spectrin-level modeling of the cytoskeleton and optical tweezers stretching of the erythrocyte. Biophysical Journal. 2005;88(5):3707-19.
55. Planus E, Fodil R, Balland M, Isabey D. Assessment of mechanical properties of adherent living cells by bead micromanipulation: comparison of magnetic twisting cytometry vs optical tweezers. Journal of biomechanical engineering. 2002;124(4):408-21.
56. De Vlaminck I, Valantine HA, Snyder TM, Strehl C, Cohen G, Luikart H, et al. Circulating cell-free DNA enables noninvasive diagnosis of heart transplant rejection. Science translational medicine. 2014;6(241):241ra77-ra77.
57. Dudani JS, Gossett DR, Henry T, Di Carlo D. Pinched-flow hydrodynamic stretching of single-cells. Lab on a Chip. 2013;13(18):3728-34.
58. Masaeli M, Gupta D, O'Byrne S, Henry T, Gossett DR, Tseng P, et al. Multiparameter mechanical and morphometric screening of cells. Scientific reports. 2016;6:37863.
59. Lin J, Kim D, Henry TT, Tseng P, Peng L, Dhar M, et al. High-throughput physical phenotyping of cell differentiation. Microsystems & Nanoengineering. 2017;3:17013.
60. Wirtz D, Konstantopoulos K, Searson PC. The physics of cancer: the role of physical interactions and mechanical forces in metastasis. Nature Reviews Cancer. 2011;11(7):512.
61. Bonakdar N, Gerum R, Kuhn M, Spörrer M, Lippert A, Schneider W, et al. Mechanical plasticity of cells. Nature Materials. 2016.
62. Trickey WR, Baaijens FP, Laursen TA, Alexopoulos LG, Guilak F. Determination of the Poisson's ratio of the cell: recovery properties of chondrocytes after release from complete micropipette aspiration. Journal of biomechanics. 2006;39(1):78-87.

63. Ofek G, Wiltz DC, Athanasiou KA. Contribution of the cytoskeleton to the compressive properties and recovery behavior of single cells. Biophysical journal. 2009;97(7):1873-82.
64. Chow S-C, Wang H, Shao J. Sample size calculations in clinical research: CRC press; 2007.
65. Freshney RI. Culture of specific cell types. Culture of animal cells: a manual of basic technique. 2005.
66. Willey JC, Harris CC. Immortalized human bronchial epithelial cell line. Google Patents; 1995.
67. Sugarman BJ, Aggarwal BB, Hass PE, Figari IS, Palladino MA, Shepard HM. Recombinant human tumor necrosis factor-alpha: effects on proliferation of normal and transformed cells in vitro. Science. 1985;230(4728):943-5.
68. Giard DJ, Aaronson SA, Todaro GJ, Arnstein P, Kersey JH, Dosik H, et al. In vitro cultivation of human tumors: establishment of cell lines derived from a series of solid tumors. Journal of the National Cancer Institute. 1973;51(5):1417-23.
69. Wakatsuki T, Schwab B, Thompson NC, Elson EL. Effects of cytochalasin D and latrunculin B on mechanical properties of cells. Journal of cell science. 2001;114(5):1025-36.
70. Coué M, Brenner SL, Spector I, Korn ED. Inhibition of actin polymerization by latrunculin A. FEBS letters. 1987;213(2):316-8.
71. Morton WM, Ayscough KR, McLaughlin PJ. Latrunculin alters the actin-monomer subunit interface to prevent polymerization. Nature cell biology. 2000;2(6):376.
72. Schiffhauer ES, Luo T, Mohan K, Srivastava V, Qian X, Griffis ER, et al. Mechanoaccumulative elements of the mammalian actin cytoskeleton. Current Biology. 2016;26(11):1473-9.
73. Srivastava V, Robinson DN. Mechanical stress and network structure drive protein dynamics during cytokinesis. Current Biology. 2015;25(5):663-70.
74. Bathe M, Shirai A, Doerschuk CM, Kamm RD. Neutrophil transit times through pulmonary capillaries: the effects of capillary geometry and fMLP-stimulation. Biophysical journal. 2002;83(4):1917-33.
75. Rosenbluth M, Lam W, Fletcher D. Analyzing cell mechanics in hematologic diseases with microfluidic biophysical flow cytometry. Lab on a chip. 2008;8(7):1062.
76. Nyberg KD, Scott MB, Bruce SL, Gopinath AB, Bikos D, Mason TG, et al. The physical origins of transit time measurements for rapid, single cell mechanotyping. Lab on a Chip. 2016;16(17):3330-9.
77. Dokukin ME, Guz NV, Sokolov I. Quantitative study of the elastic modulus of loosely attached cells in AFM indentation experiments. Biophysical journal. 2013;104(10):2123-31.
78. Li Q, Lee G, Ong C, Lim C, editors. Probing the elasticity of breast cancer cells using AFM. 13th International Conference on Biomedical Engineering; 2009: Springer.
79. Xu C, Wang Y, Jiang N, Yang H, Lin J, Xie S, editors. Elasticity measurement of breast cancer cells by atomic force microscopy. Twelfth International Conference on

Photonics and Imaging in Biology and Medicine (PIBM 2014); 2014: International Society for Optics and Photonics.
80. Alcaraz J, Buscemi L, Grabulosa M, Trepat X, Fabry B, Farré R, et al. Microrheology of human lung epithelial cells measured by atomic force microscopy. Biophysical journal. 2003;84(3):2071-9.
81. Acerbi I, Luque T, Giménez A, Puig M, Reguart N, Farré R, et al. Integrin-specific mechanoresponses to compression and extension probed by cylindrical flat-ended AFM tips in lung cells. PLoS One. 2012;7(2):e32261.
82. Demichelis A, Divieto C, Mortati L, Sassi M, Sassi G, editors. Preliminary measurements of elasticity properties of lung tumor living cells for cancer detection. Medical Measurements and Applications (MeMeA), 2015 IEEE International Symposium on; 2015: IEEE.
83. Liu AY, Roudier MP, True LD. Heterogeneity in primary and metastatic prostate cancer as defined by cell surface CD profile. The American journal of pathology. 2004;165(5):1543-56.
84. Symmans WF, Liu J, Knowles DM, Inghirami G. Breast cancer heterogeneity: evaluation of clonality in primary and metastatic lesions. Human pathology. 1995;26(2):210-6.
85. Dexter DL, Spremulli EN, Fligiel Z, Barbosa JA, Vogel R, VanVoorhees A, et al. Heterogeneity of cancer cells from a single human colon carcinoma. The American journal of medicine. 1981;71(6):949-56.
86. Polyak K. Heterogeneity in breast cancer. The Journal of clinical investigation. 2011;121(10):3786-8.
87. Fisher R, Pusztai L, Swanton C. Cancer heterogeneity: implications for targeted therapeutics. British journal of cancer. 2013;108(3):479-85.
88. Chang JC, Brewer GJ, Wheeler BC. A modified microstamping technique enhances polylysine transfer and neuronal cell patterning. Biomaterials. 2003;24(17):2863-70.
89. Wang L, Sun B, Ziemer KS, Barabino GA, Carrier RL. Chemical and physical modifications to poly (dimethylsiloxane) surfaces affect adhesion of Caco‐2 cells. Journal of biomedical materials research Part A. 2010;93(4):1260-71.
90. Zhou J, Ellis AV, Voelcker NH. Recent developments in PDMS surface modification for microfluidic devices. Electrophoresis. 2010;31(1):2-16.
91. Ronan W, Deshpande VS, McMeeking RM, McGarry JP. Numerical investigation of the active role of the actin cytoskeleton in the compression resistance of cells. Journal of the Mechanical Behavior of Biomedical Materials. 2012;14:143-57.
92. Rivest F, Pachacek A, Pack R, Goodman K, Cho N, Lustig M, et al., editors. Toward Real-time Cell Detection and Characterization Using Barker-coded Node-pore Sensing (NPS). Proceedings of the 2015 μTAS Conference, Gyeongju, Korea; 2015.
93. Kellman M, Rivest F, Pechacek A, Sohn L, Lustig M, editors. Barker-Coded node-pore resistive pulse sensing with built-in coincidence correction. Acoustics, Speech and Signal Processing (ICASSP), 2017 IEEE International Conference on; 2017: Ieee.

94. Kavallaris M. Microtubules and resistance to tubulin-binding agents. Nature Reviews Cancer. 2010;10(3):194-204.
95. Pasquier E, Kavallaris M. Microtubules: a dynamic target in cancer therapy. IUBMB life. 2008;60(3):165-70.
96. De Donato M, Mariani M, Petrella L, Martinelli E, Zannoni GF, Vellone V, et al. Class III β - tubulin and the cytoskeletal gateway for drug resistance in ovarian cancer. Journal of cellular physiology. 2012;227(3):1034-41.
97. Bichat F, Mouawad R, Solis-Recendez G, Khayat D, Bastian G. Cytoskeleton alteration in MCF7R cells, a multidrug resistant human breast cancer cell line. Anticancer research. 1996;17(5A):3393-401.
98. Gudjonsson T, Adriance MC, Sternlicht MD, Petersen OW, Bissell MJ. Myoepithelial cells: their origin and function in breast morphogenesis and neoplasia. Journal of mammary gland biology and neoplasia. 2005;10(3):261-72.
99. Ewald AJ, Brenot A, Duong M, Chan BS, Werb Z. Collective epithelial migration and cell rearrangements drive mammary branching morphogenesis. Developmental cell. 2008;14(4):570-81.
100. Mammoto A, Ingber DE. Cytoskeletal control of growth and cell fate switching. Current opinion in cell biology. 2009;21(6):864-70.
101. Garbe JC, Pepin F, Pelissier F, Sputova K, Fridriksdottir AJ, Guo DE, et al. Accumulation of multipotent progenitors with a basal differentiation bias during aging of human mammary epithelia. Cancer Research. 2012;72(14):3687-701.
102. LaBarge MA, Garbe JC, Stampfer MR. Processing of human reduction mammoplasty and mastectomy tissues for cell culture. JoVE (Journal of Visualized Experiments). 2013(71):e50011-e.
103. LaBarge MA. Human Mammary Epithelial Cell (HMEC) Bank Website 2003 [Available from: http://hmec.lbl.gov/mindex.html.
104. MacKeown PK. Stochastic Simulation in Physics, 1997: Springer, Singapore; 1997.
105. Garbe JC, Vrba L, Sputova K, Fuchs L, Novak P, Brothman AR, et al. Immortalization of normal human mammary epithelial cells in two steps by direct targeting of senescence barriers does not require gross genomic alterations. Cell Cycle. 2014;13(21):3423-35.
106. Lee JK, Garbe JC, Vrba L, Miyano M, Futscher BW, Stampfer MR, et al. Age and the means of bypassing stasis influence the intrinsic subtype of immortalized human mammary epithelial cells. Frontiers in cell and developmental biology. 2015;3.
107. Stossel TP, Condeelis J, Cooley L, Hartwig JH, Noegel A, Schleicher M, et al. Filamins as integrators of cell mechanics and signalling. Nature Reviews Molecular Cell Biology. 2001;2(2):138-45.
108. Janmey PA, McCulloch CA. Cell mechanics: integrating cell responses to mechanical stimuli. Annu Rev Biomed Eng. 2007;9:1-34.
109. Lange JR, Fabry B. Cell and tissue mechanics in cell migration. Experimental cell research. 2013;319(16):2418-23.

110. Suresh S. Biomechanics and biophysics of cancer cells. Acta Materialia. 2007;55(12):3989-4014.
111. Provenzano PP, Keely PJ. Mechanical signaling through the cytoskeleton regulates cell proliferation by coordinated focal adhesion and Rho GTPase signaling. J Cell Sci. 2011;124(8):1195-205.
112. Yamaguchi H, Condeelis J. Regulation of the actin cytoskeleton in cancer cell migration and invasion. Biochimica et Biophysica Acta (BBA)-Molecular Cell Research. 2007;1773(5):642-52.
113. Woods A, Wang G, Beier F. Regulation of chondrocyte differentiation by the actin cytoskeleton and adhesive interactions. Journal of cellular physiology. 2007;213(1):1-8.
114. Gourlay CW, Ayscough KR. The actin cytoskeleton: a key regulator of apoptosis and ageing? Nature reviews Molecular cell biology. 2005;6(7):583.
115. Kumar S, Weaver VM. Mechanics, malignancy, and metastasis: the force journey of a tumor cell. Cancer and Metastasis Reviews. 2009;28(1-2):113-27.
116. Prabhune M, Belge G, Dotzauer A, Bullerdiek J, Radmacher M. Comparison of mechanical properties of normal and malignant thyroid cells. Micron. 2012;43(12):1267-72.
117. Benham-Pyle BW, Pruitt BL, Nelson WJ. Mechanical strain induces E-cadherin–dependent Yap1 and β-catenin activation to drive cell cycle entry. Science. 2015;348(6238):1024-7.
118. ALTMAN G, HORAN R, Martin I, Farhadi J, STARK P, Volloch V, et al. Cell differentiation by mechanical stress. The FASEB Journal. 2002;16(2):270-2.
119. Luu YK, Capilla E, Rosen CJ, Gilsanz V, Pessin JE, Judex S, et al. Mechanical stimulation of mesenchymal stem cell proliferation and differentiation promotes osteogenesis while preventing dietary ‐ induced obesity. Journal of Bone and Mineral Research. 2009;24(1):50-61.
120. Saha S, Ji L, de Pablo JJ, Palecek SP. Inhibition of human embryonic stem cell differentiation by mechanical strain. Journal of cellular physiology. 2006;206(1):126-37.
121. Cabrera-Benítez NE, Parotto M, Post M, Han B, Spieth PM, Cheng W-E, et al. Mechanical stress induces lung fibrosis by epithelial-mesenchymal transition (EMT). Critical care medicine. 2012;40(2):510.
122. Gjorevski N, Boghaert E, Nelson CM. Regulation of epithelial-mesenchymal transition by transmission of mechanical stress through epithelial tissues. Cancer Microenvironment. 2012;5(1):29-38.
123. Sato M, Levesque MJ, Nerem RM. Micropipette aspiration of cultured bovine aortic endothelial cells exposed to shear stress. Arteriosclerosis, Thrombosis, and Vascular Biology. 1987;7(3):276-86.
124. Sato M, Theret D, Wheeler L, Ohshima N, Nerem R. Application of the micropipette technique to the measurement of cultured porcine aortic endothelial cell viscoelastic properties. Journal of biomechanical engineering. 1990;112(3):263-8.
125. Desprat N, Guiroy A, Asnacios A. Microplates-based rheometer for a single living cell. Review of scientific instruments. 2006;77(5):055111.

126. Guck J, Ananthakrishnan R, Mahmood H, Moon TJ, Cunningham CC, Käs J. The optical stretcher: a novel laser tool to micromanipulate cells. Biophysical journal. 2001;81(2):767-84.
127. Yang T, Bragheri F, Minzioni P. A comprehensive review of optical stretcher for cell mechanical characterization at single-cell level. Micromachines. 2016;7(5):90.
128. Haase K, Pelling AE. Investigating cell mechanics with atomic force microscopy. Journal of The Royal Society Interface. 2015;12(104):20140970.
129. Guo Q, Park S, Ma H. Microfluidic micropipette aspiration for measuring the deformability of single cells. Lab on a Chip. 2012;12(15):2687-95.
130. Cartagena-Rivera AX, Wang W-H, Geahlen RL, Raman A. Fast, multi-frequency, and quantitative nanomechanical mapping of live cells using the atomic force microscope. Scientific reports. 2015;5:11692.
131. Preira P, Valignat M-P, Bico J, Théodoly O. Single cell rheometry with a microfluidic constriction: Quantitative control of friction and fluid leaks between cell and channel walls. Biomicrofluidics. 2013;7(2):024111.
132. Hu S, Lam RH. Characterization of viscoelastic properties of normal and cancerous human breast cells using a confining microchannel. Microfluidics and Nanofluidics. 2017;21(4):68.
133. Coulter WH. Means for counting particles suspended in a fluid. Google Patents; 1953.
134. Saleh O, Sohn L. Quantitative sensing of nanoscale colloids using a microchip Coulter counter. Review of Scientific Instruments. 2001;72(12):4449-51.
135. Freshney RI. Culture of specific cell types: Wiley Online Library; 2005.
136. Giard DJ, Aaronson SA, Todaro GJ, Arnstein P, Kersey JH, Dosik H, et al. In Vitro Cultivation of Human Tumors: Establishment of Cell Lines Derived From a Series of Solid Tumors 2. Journal of the National Cancer Institute. 1973;51(5):1417-23.
137. Reddel RR, Yang K, Rhim JS, Brash D, Su RT, Lechner JF, et al. Immortalized human bronchial epitherial mesothelial cell lines. Google Patents; 1989.
138. Kubitschke H, Schnauss J, Nnetu K, Warmt E, Stange R, Kaes J. Actin and microtubule networks contribute differently to cell response for small and large strains. New Journal of Physics. 2017;19(9):093003.
139. Bostock C, Prescott D, Kirkpatrick J. An evaluation of the double thymidine block for synchronizing mammalian cells at the G1-S border. Experimental cell research. 1971;68(1):163-8.
140. Sinkus R, Tanter M, Xydeas T, Catheline S, Bercoff J, Fink M. Viscoelastic shear properties of in vivo breast lesions measured by MR elastography. Magnetic resonance imaging. 2005;23(2):159-65.
141. Fletcher DA, Mullins RD. Cell mechanics and the cytoskeleton. Nature. 2010;463(7280):485.
142. Lindberg U, Karlsson R, Lassing I, Schutt CE, Höglund A-S, editors. The microfilament system and malignancy. Seminars in cancer biology; 2008: Elsevier.

143. Proietti S, Catizone A, Masiello MG, Dinicola S, Fabrizi G, Minini M, et al. Increase in motility and invasiveness of MCF 7 cancer cells induced by nicotine is abolished by melatonin through inhibition of ERK phosphorylation. Journal of pineal research. 2018;64(4):e12467.
144. Geltmeier A, Rinner B, Bade D, Meditz K, Witt R, Bicker U, et al. Characterization of dynamic behaviour of MCF7 and MCF10A cells in ultrasonic field using modal and harmonic analyses. PloS one. 2015;10(8):e0134999.
145. Gardel ML, Kasza KE, Brangwynne CP, Liu J, Weitz DA. Mechanical response of cytoskeletal networks. Methods in cell biology. 2008;89:487-519.
146. Brangwynne CP, MacKintosh FC, Kumar S, Geisse NA, Talbot J, Mahadevan L, et al. Microtubules can bear enhanced compressive loads in living cells because of lateral reinforcement. J Cell Biol. 2006;173(5):733-41.
147. Baluska F, Barlow P. The role of the microtubular cytoskeleton in determining nuclear chromatin structure and passage of maize root cells through the cell cycle. European journal of cell biology. 1993;61(1):160-7.
148. Rusan NM, Fagerstrom CJ, Yvon A-MC, Wadsworth P. Cell cycle-dependent changes in microtubule dynamics in living cells expressing green fluorescent protein-α tubulin. Molecular biology of the cell. 2001;12(4):971-80.
149. Charras GT, Horton MA. Single cell mechanotransduction and its modulation analyzed by atomic force microscope indentation. Biophysical journal. 2002;82(6):2970-81.
150. Shapiro E, Biezuner T, Linnarsson S. Single-cell sequencing-based technologies will revolutionize whole-organism science. Nature Reviews Genetics. 2013;14(9):618.
151. White AK, VanInsberghe M, Petriv I, Hamidi M, Sikorski D, Marra MA, et al. High-throughput microfluidic single-cell RT-qPCR. Proceedings of the National Academy of Sciences. 2011;108(34):13999-4004.
152. Streets AM, Zhang X, Cao C, Pang Y, Wu X, Xiong L, et al. Microfluidic single-cell whole-transcriptome sequencing. Proceedings of the National Academy of Sciences. 2014;111(19):7048-53.
153. Yeung A, Evans E. Cortical shell-liquid core model for passive flow of liquid-like spherical cells into micropipets. Biophysical journal. 1989;56(1):139-49.
154. Karcher H, Lammerding J, Huang H, Lee RT, Kamm RD, Kaazempur-Mofrad MR. A three-dimensional viscoelastic model for cell deformation with experimental verification. Biophysical journal. 2003;85(5):3336-49.
155. Schmid-Schönbein G, Sung K, Tözeren H, Skalak R, Chien S. Passive mechanical properties of human leukocytes. Biophysical Journal. 1981;36(1):243-56.
156. Leterrier J. Water and the cytoskeleton. Cellular and molecular biology (Noisy-le-Grand, France). 2001;47(5):901-23.
157. Haider MA. A radial biphasic model for local cell-matrix mechanics in articular cartilage. SIAM Journal on Applied Mathematics. 2004;64(5):1588-608.
158. Bonakdar N, Gerum R, Kuhn M, Spörrer M, Lippert A, Schneider W, et al. Mechanical plasticity of cells. Nature materials. 2016;15(10):1090.

159. Goldmann WH, Auernheimer V, Thievessen I, Fabry B. Vinculin, cell mechanics and tumour cell invasion. Cell biology international. 2013;37(5):397-405.
160. Peyton SR, Ghajar CM, Khatiwala CB, Putnam AJ. The emergence of ECM mechanics and cytoskeletal tension as important regulators of cell function. Cell biochemistry and biophysics. 2007;47(2):300-20.
161. Dent R, Trudeau M, Pritchard KI, Hanna WM, Kahn HK, Sawka CA, et al. Triple-negative breast cancer: clinical features and patterns of recurrence. Clinical cancer research. 2007;13(15):4429-34.
162. Schneider BP, Winer EP, Foulkes WD, Garber J, Perou CM, Richardson A, et al. Triple-negative breast cancer: risk factors to potential targets. Clinical Cancer Research. 2008;14(24):8010-8.
163. Hudis CA, Gianni L. Triple-negative breast cancer: an unmet medical need. The oncologist. 2011;16(Supplement 1):1-11.
164. Martin SK, Kamelgarn M, Kyprianou N. Cytoskeleton targeting value in prostate cancer treatment. American journal of clinical and experimental urology. 2014;2(1):15.
165. Checchi PM, Nettles JH, Zhou J, Snyder JP, Joshi HC. Microtubule-interacting drugs for cancer treatment. Trends in pharmacological sciences. 2003;24(7):361-5.
166. Tommasi S, Mangia A, Lacalamita R, Bellizzi A, Fedele V, Chiriatti A, et al. Cytoskeleton and paclitaxel sensitivity in breast cancer: The role of β -tubulins. International journal of cancer. 2007;120(10):2078-85.
167. Hartwell LH, Kastan MB. Cell cycle control and cancer. Science. 1994;266(5192):1821-8.
168. Kastan MB, Bartek J. Cell-cycle checkpoints and cancer. Nature. 2004;432(7015):316.
169. Abraham RT. Cell cycle checkpoint signaling through the ATM and ATR kinases. Genes & development. 2001;15(17):2177-96.
170. Smith J, Tho LM, Xu N, Gillespie DA. The ATM–Chk2 and ATR–Chk1 pathways in DNA damage signaling and cancer. Advances in cancer research. 108: Elsevier; 2010. p. 73-112.
171. Rivest F, Pachacek A, Pack R, Goodman K, Cho N, Lustig M, et al., editors. Toward real-time cell detection and characterization using barker-coded node-pore sensing (nps). Proceedings of the 2015 μTAS Conference; 2015.
172. Kellman MR, Rivest FR, Pechacek A, Sohn LL, Lustig M. Node-Pore Coded Coincidence Correction: Coulter Counters, Code Design, and Sparse Deconvolution. IEEE Sensors Journal. 2018;18(8):3068-79.
173. Sinnokrot MO, Barry JR, Madisetti VK. The Asymmetric Golden Code for Fast Decoding on Time-Varying Channels. Wireless Personal Communications. 2011;58(3):421-37.
174. Liu Z, Huang F, Du J, Shu W, Feng H, Xu X, et al. Rapid isolation of cancer cells using microfluidic deterministic lateral displacement structure. Biomicrofluidics. 2013;7(1):011801.

175. McGrath J, Jimenez M, Bridle H. Deterministic lateral displacement for particle separation: a review. Lab on a Chip. 2014;14(21):4139-58.
176. Di Carlo D, Irimia D, Tompkins RG, Toner M. Continuous inertial focusing, ordering, and separation of particles in microchannels. Proceedings of the National Academy of Sciences. 2007;104(48):18892-7.
177. Kuntaegowdanahalli SS, Bhagat AAS, Kumar G, Papautsky I. Inertial microfluidics for continuous particle separation in spiral microchannels. Lab on a Chip. 2009;9(20):2973-80.
178. Zhang J, Tian X-J, Zhang H, Teng Y, Li R, Bai F, et al. TGF-β–induced epithelial-to-mesenchymal transition proceeds through stepwise activation of multiple feedback loops. Sci Signal. 2014;7(345):ra91-ra.
179. O'Connell GD, Tan AR, Cui V, Bulinski JC, Cook JL, Attur M, et al. Human chondrocyte migration behaviour to guide the development of engineered cartilage. Journal of tissue engineering and regenerative medicine. 2017;11(3):877-86.
180. Alegre-Aguarón E, Sampat SR, Xiong JC, Colligan RM, Bulinski JC, Cook JL, et al. Growth factor priming differentially modulates components of the extracellular matrix proteome in chondrocytes and synovium-derived stem cells. PLoS One. 2014;9(2):e88053.
181. Sarrió D, Rodriguez-Pinilla SM, Hardisson D, Cano A, Moreno-Bueno G, Palacios J. Epithelial-mesenchymal transition in breast cancer relates to the basal-like phenotype. Cancer research. 2008;68(4):989-97.
182. Larue L, Bellacosa A. Epithelial–mesenchymal transition in development and cancer: role of phosphatidylinositol 3′ kinase/AKT pathways. Oncogene. 2005;24(50):7443.

Appendix

Appendix A

Customized MATLAB code to analyze signals generated from mechano-NPS

```
%% Set variables

Nstart =403;
FiletoRead=5;
thresholds=[1e-4 .8e-3];

file_num = [Nstart,FiletoRead]; % file numbers, 1 is the first #, 2 is
the number of files to read after

error=0.08;
dt=50;
Ndown=20;   %down sampling period
Fs=50;  %sampling frequency [kHz]

%% Reading data files

mydata = cell(1,1+file_num(2));
    k = file_num(1); % initialize reads
    i = 1;
    while (k < file_num(1) + file_num(2))
        file_name = sprintf('trial1_%05d.txt',k);
        file_id = fopen(file_name);
        file_data = textscan(file_id,'%f');
        mydata{i} = file_data{:};
        k = k + 1;
        i = i + 1;
        fclose(file_id);
    end

y=cat(1,mydata{:}); % concatenate data
y_smoothed=fastsmooth(y',100,1,1); % perform smoothing
y_detrend=detrend(y_smoothed); % remove trend
ym=downsample(y_detrend,Ndown); % downsample by period N

clear myfilename mydata i k,

%% Threshold signal by differences

% take the difference of ym, threshold by th1
% thresholds = [1.5e-4, 1.0e-3]; % thresholds for differences, user
% provided

    ym_diff = diff(ym); % compute difference
    ym_diff(abs(ym_diff) < thresholds(1)) = 0; % threshold values below
thresholds(1)

for i=1:size(ym,2)-1
    if ym_diff(i)<-thresholds(2)
       k=i+1;
       for j=k:size(ym,2)-1
```

```
            if  abs(ym_diff(j))<thresholds(2)
                ym_diff(j)=0;
            elseif ym_diff(j)>thresholds(2)
                break;
            end
        end
    end
end

%% identify nonzero differences, A is the matrix of nonzero differences

    backset = 20;
    A = ones(3,length(nonzeros(ym_diff))); % preallocation
    k=0;
    for i=1:length(ym_diff)
        if abs(ym_diff(i))>0
            k=k+1;
            A(1,k)=i*Ndown; % array index of nonzero
            A(2,k)=ym_diff(i); % nonzero value
            A(3,k)=(i-backset)*Ndown; % backward offset for baseline
current
        end
    end

    clear tmp,

%% Remove error from A

    k=1;
    while (k < ceil(log(length(A))))
        i=1;
        while (i < length(A))

            % Case 1: current and next both positive && next > current
            if A(2,i) > 0 && A(2,i+1) > 0 && ...
                    A(2,i) < A(2,i+1)
                % move next into current
                A(:,i)=A(:,i+1);

            % Case 2: current and next both positive && current > next
            elseif A(2,i) > 0 && A(2,i+1) > 0 && ...
                    A(2,i) > A(2,i+1)
                % move current into next
                A(:,i+1)=A(:,i);

            % Case 3: current and next both negative && current > next
            elseif A(2,i) < 0 && A(2,i+1) < 0 && ...
                    A(2,i) > A(2,i+1)
                % move next into current
                A(:,i)=A(:,i+1);

            % Case 4: current and next both negative && next > current
            elseif A(2,i) < 0 && A(2,i+1) < 0 && ...
                    A(2,i) < A(2,i+1)
                % move current into next
```

```
                A(:,i+1)=A(:,i);
            end

            i=i+1;
        end
        k=k+1;
    end

%% Remove repeats in A

    stop = length(A);
    i = 1;

    while (i < stop)
       if (A(:,i) == A(:,i+1))
           A(:,i) = [];
           stop = stop - 1;
       else
           i = i + 1;
       end
    end

%% Rectangularize pulses
    ym_rect = ym;
    k=1;
    while (k <= 50)
        i = 1;
        while (i < length(A))

            if A(2,i) < 0 && A(2,i+1) > 0 % look for sign change in
differences
                ym_rect(A(1,i)/Ndown:A(1,i+1)/Ndown) = ...
                    mean(ym(A(1,i)/Ndown:A(1,i+1)/Ndown));
                % replace all values in between with mean
            end

            i=i+1;
        end
        k=k+1;
    end


%% Figures
    figure('units', 'pixels', 'pos',[0 0 1300 1000])
    subplot(2,2,1)
    plot(ym_diff,'b-');
    title('Differenciation of I')
    set(gca,'FontSize',20)
    subplot(2,2,2)
    plot(y_smoothed,'k-');
    title('y_{detrend}')
    set(gca,'FontSize',20)
    subplot(2,2,3:4)
    plot(ym_rect);
    title('ym')
```

```
    set(gca,'FontSize',20)
    grid on

%% Detect NPS pulses, build pulse matrix P
    i=1;
    k = 0;
    while (i < length(A))
        if A(2,i) < 0 && A(2,i+1) > 0 && A(3,i) > 0 % check non-repeats
            k=k+1;
            P(k,1) = A(1,i);  % Start index
            P(k,2) = y_detrend(A(3,i)); % normalized baseline current
            P(k,3) = mean(y_detrend(A(1,i)+1:A(1,i+1)-1)); % avg
current between pulses
            P(k,4) = A(1,i+1)-A(1,i); % change in index
            P(k,5) = y_smoothed(A(3,i)); % baseline current, no detrend
            P(k,6) = A(1,i+1); % End index
            %P(k,7) = y_detrend(A(1,i+1)+dt);
        end
        i=i+1;
    end
 %%
    N=1;
    for k=1:length(P)-6
        start_index = P(k,1); % starting index of pulse
        fileN = floor(start_index/20000)+file_num(1); % compute which
file # the pulse is in
        I = P(k,5); % compute baseline current
        dI = mean(abs([P(k,2) - P(k,3), P(k,2) - P(k+1,3)])); % average
NP current drop
        dI1 = P(k,2) - P(k+3,3); % squeeze current drop
        dT = (P(k+1,6) - P(k,1))/2/Fs; % NP transit time in ms
        dT1 = (P(k+4,1)-P(k+3,1))/Fs; % squeeze transit time in ms

        % post-squeeze NP current drops
        dI4 = abs(P(k,2) - P(k+4,3));
        dI5 = abs(P(k,2) - P(k+5,3));
        dI6 = abs(P(k,2) - P(k+6,3));

        % recovery time determined when post-squeeze NP current drop
reaches
        % pre-squeeze NP current drop
        if abs(dI6-dI)/dI < error % last pulse is recovered
            Tr = (P(k+5,1) - P(k+3,1))/Fs; % recovery time in ms

        elseif abs(dI5-dI)/dI < error % 2nd to last pulse is recovered
            Tr = (P(k+4,1) - P(k+3,1))/Fs; % recovery time in ms

        elseif dI4 < dI*(1-error) && dI5 < dI*(1-error) && dI6 < dI*(1-
error) % never recovers
            Tr = inf;

        else
            Tr = 0;
        end
```

```
    if dI>0 && dI1>0
    Out(N,:)=[start_index/Ndown fileN I dI dI1 dT dT1 Tr];
    N=N+1;
    end

end
```

Appendix B

Customized MATLAB code to analyze signals generated from visco-NPS

```
%% set variables

Nstart =1330;
FiletoRead=10;

file_num = [Nstart,FiletoRead]; % file numbers, 1 is the first #, 2 is
the number of files to read after
Fs=50;  %sampling frequency [kHz]
Ndown=10;    %down sampling period
buffer = 3000;  %buffer to measure baseline current at the both end of
signal
MaxSignalSize=7000; %Maximum length of signal to set matrix
MaxSignalSize2=5000; %Maximum length of dSignal to set matrix
ThrX=1.5e-4; %derivative threshold value for node-pore

%% read data files

mydata = cell(1,1+file_num(2));
    k = file_num(1); % initialize reads
    i = 1;
    while (k < file_num(1) + file_num(2))
        file_name = sprintf('trial1_%05d.txt',k);
        file_id = fopen(file_name);
        file_data = textscan(file_id,'%f');
        mydata{i} = file_data{:};
        k = k + 1;
        i = i + 1;
        fclose(file_id);
    end

y=cat(1,mydata{:}); % concatenate data
y_smoothed=fastsmooth(y',100,1,1); % perform smoothing
y_detrend=detrend(y_smoothed); % remove trend

clear myfilename mydata i k,

%% find outliers && group by clumps
out = isoutlier(y_detrend);

out_ind = 1;
group = zeros(2,length(out));
group_ind = 1;
while out_ind < length(out)
    if out(out_ind) == 1
        group(1,group_ind) = out_ind; % first number in the group
        group(2,group_ind) = 1; %counter for consecutive 1s
        out_ind = out_ind + 1;
            while out_ind < length(out) && out(out_ind) == 1 %checks if
the following data is 0
```

```
                group(2,group_ind) = group(2,group_ind) + 1; %adds to
the count
                out_ind = out_ind + 1;
            end
    end
    out_ind = out_ind + 1;
    group_ind = group_ind + 1;
end
group(:, all(group==0))=[]; % removes 0, 0 data

clear out out_len out_ind,

%% combines signals if the gap btwn the signals is small
gap = 1000;
group_ind = 1;
while group_ind < length(group)
    last_index = group(1,group_ind) + group(2,group_ind); %last point
of group
    if group(1, group_ind + 1) - last_index < gap % checks if the gap
btwn groups is small. If so, we combine the groups
        group(2, group_ind) = group(1, group_ind + 1) + group(2,
group_ind + 1) - group(1, group_ind); %last index of 2nd group - first
index of 1st = length
        group(:,group_ind + 1) = [];
    else
        group_ind = group_ind + 1;
    end
end

%% creates "signals" matrix
% takes each group and puts it in matrix "signals" with each column
being a
% cell signal data

signal_max = max(group(2,:));
signal_detrend = zeros(MaxSignalSize,length(group)); % creates a matrix
with size (group x (number of data points + buffer))
signal_smooth = zeros(MaxSignalSize,length(group));

for xx=1:length(group)
    if group(2,xx)<MaxSignalSize

        for i = 1:length(group)
            start_signal = group(1,i) - 1500;

            if start_signal < 1
                buffer = buffer - start_signal;
                start_signal = 1;
            end
            end_signal = start_signal + group(2,i) + buffer;

            if (end_signal-start_signal)< MaxSignalSize
            data1 = y_smoothed(start_signal:end_signal);
```

```
            data2 = y_detrend(start_signal:end_signal);
            end

            signal_smooth(1:length(data1),i) = data1;
            signal_detrend(1:length(data2),i) = data2;
            signal_down=downsample(signal_detrend,Ndown);
            signal_length(1,i)=size(signal_down(:,i),1);
            buffer = 3000;

        end
    end
end
clear start_signal end_signal buffer gap last_index group_ind data1
data2 signal_max xx,

%% derivative of signal

for i=1:length(group)
    signal_temp=signal_down(1:signal_length(1,i),i);
    signal_diff(1:signal_length(1,i)-1,i)=diff(signal_temp);
    clear signal_temp
end

clear y y_detrend y_smoothed ym

%% find threshold and clean up random noise

for jj=1:length(group)

    Thr1=ThrX; %derivative threshold value for node-pore
    pks=[0 0 0 0];
    locs=[0 0 0 0];

    [pks,locs]=findpeaks(signal_detrend(:,jj),'MinPeakProminence',1e-
3); %find peaks

    TF=isoutlier(pks);  %find outlier within peaks

    for k=1:length(pks)     %keep pks only for the contraction channel
        if TF(k)==1
            pks(k)=NaN;
            locs(k)=NaN;
        end
    end
    pks(find(isnan(pks)))=[];
    locs(find(isnan(locs)))=[];

    Thr2=mean(pks)*0.9;     %2nd thresholds for the contraction channel
    Thr(:,jj)=[Thr1; Thr2];

    if Thr1~=0
        for k=1:length(signal_diff(:,jj))
```

```
        if abs(signal_diff(k,jj))< Thr1
            signal_diff(k,jj)=0;
        end
    end
end

if Thr2~=0
    for i=1:length(signal_down(:,jj))
        if signal_down(i,jj)<Thr2
            k=i+1;
           for j=k:length(signal_down(:,jj))
                if  signal_down(j,jj)<Thr2
                    signal_diff(j,jj)=0;
                elseif signal_down(j,jj)>Thr2
                    break;
                end
           end
        end
    end
end

hFig=figure(jj);
set(hFig,'Position', [0 300 1200 400])

subplot(1,2,1)
x_temp=1:1:length(signal_detrend(:,jj));
p1=plot(signal_detrend(:,jj));
hold on
p2=plot(locs,pks,'ob');
p3=plot(x_temp,Thr2*ones(1,length(signal_detrend(:,jj))),'r-');
hold off
legend(p3,sprintf('%0.2e',Thr2))
set(gca,'FontSize',15)

subplot(1,2,2)
x_temp2=1:1:length(signal_diff(:,jj));
plot(signal_diff(:,jj))
hold on
p4=plot(x_temp2,Thr1*ones(1,length(signal_diff(:,jj))),'r-');
p5=plot(x_temp2,-Thr1*ones(1,length(signal_diff(:,jj))),'r-');
legend(p4,sprintf('%0.2e',Thr1))
set(gca,'FontSize',15)

fprintf([ 'ENTER will return thresholds,\n' ...
                'S will reture 0\n' ...
                'Or, just enter new threshold for node-pore \n' ...
                ]);
OK = input('---\n','s');

switch OK
    case []
        Thr(:,jj)=[Thr1; Thr2];
    case{'s','S'}
        Thr(:,jj)=[0; 0];
```

```
        otherwise

            Thr1=str2double(OK);
            fprintf(['Now enter new threshold for the contraction
channel \n']);
            Thr2=input('---\n');
            Thr(:,jj)=[Thr1; Thr2];

            close all
                hFig=figure(jj);
                set(hFig,'Position', [0 300 1200 400])

                subplot(1,2,1)
                x_temp=1:1:length(signal_detrend(:,jj));
                p1=plot(signal_detrend(:,jj));
                hold on
                p2=plot(locs,pks,'ob');

p3=plot(x_temp,Thr2*ones(1,length(signal_detrend(:,jj))),'r-');
                hold off
                legend(p3,sprintf('%0.2e',Thr2))
                set(gca,'FontSize',15)

                subplot(1,2,2)
                x_temp2=1:1:length(signal_diff(:,jj));
                plot(signal_diff(:,jj))
                hold on

p4=plot(x_temp2,Thr1*ones(1,length(signal_diff(:,jj))),'r-');
                p5=plot(x_temp2,-
Thr1*ones(1,length(signal_diff(:,jj))),'r-');
                legend(p4,sprintf('%0.2e',Thr1))
                set(gca,'FontSize',15)

                fprintf(['Press ENTER \n']);
                a=input('---\n');
    end
    close all
end

clear i j jj k locs locs1 pks pks1 TF a p1 p2 p3 p4 p5 OK hFig Thr1
Thr2 x_temp x_temp2


preData=zeros(9,length(group));
global ii;
for ii=1:length(group)
[dSignal(:,ii), preData(:,ii)] = stepX (signal_smooth(:,ii),
signal_detrend(:,ii), signal_diff(:,ii), Ndown, file_num, Fs,
MaxSignalSize2);
end

%% export signal and measured data
```

```
global fj fi

if isempty(fj)
    fj=1;
end

savename=sprintf('SignalOut_trial%03d.mat',fj);
fj=fj+1;

if isempty(fi)
    fi=1;
end

for i=1:length(group)
    if preData(1,i)~=0
        SignalOut(:,fi)=signal_smooth(:,i);
        MeasureOut(:,fi)=preData(:,i);
        dSignalOut(:,fi)=dSignal(:,i);
        ThrOut(:,fi)=Thr(:,i);
        save(savename,'SignalOut','MeasureOut','dSignalOut','ThrOut')
        fi=fi+1;
    end
end

clear dSignal file_data file_id file_name file_num FiletoRead group i
ii j MaxSignalSize Ndown Nstart preData signal_detrend signal_diff
signal_down signal_length signal_measure signal_smooth Thr ThrX
close all
```

Appendix C

Example of MATLAB code to measure viscoelastic properties of cells

```
%% Read out pulse
load('SignalOut_trial048.mat')
for i=1:length(MeasureOut)

    I=MeasureOut(4,i);
    dI=MeasureOut(5,i);
    U0=700/MeasureOut(6,i);
    dT=MeasureOut(7,i);
    dIDynamic=dSignalOut(:,i);
    dIDynamic(dIDynamic==0)=[];

    d=(dI*L*(D^2)/(I+dI*L*0.8/D))^(1/3); %cell diameter
    w=10*pi*1000/dT;

    t=0:1:length(dIDynamic)-1;
    t=t./(1000*f);

    width=transpose((w_max+w_min)/2+(w_max-w_min)/2.*cos(w*t));
%channel width
    e=(d-width)./d;          %strain
    D2=D.*(width./w_np).^0.5;  %effective D of cont. channel[um]

    dD=(dIDynamic.*L.*(D2.^2)./(I+dIDynamic.*L.*0.8./D2)).^(1/3);
    dD=pi.*(dD.^2)./(4*width); %deformed diameter
    StressMu=2.*(dP.*((w_max+w_min)/2).*1e-6).*(dD.*1e-6)./(pi.*(d*1e-
6)^2); %stress x mu

    xdata=transpose(t);
    x0=[100, 1000, 0, 0.3];
    lb=[0, 0, 0, 0];
    ub=[inf, inf, inf, inf];
    fun =@(x,xdata)((x(1)*(1-((w_max+w_min)/(d*2)))-x(2)*((w_max-
w_min)/(2*d))*cos(w*xdata)-((w_max-
w_min)/2/d)*x(3)*sin(w*xdata)).*x(4));
    ydata=StressMu;
    x=lsqcurvefit(fun,x0,xdata,ydata,lb,ub);

    RheologyOut_M7_L500_3p(:,i)=[MeasureOut(1,i); MeasureOut(2,i); d;
5000/dT; x(1); x(2); x(3); x(4); U0];


end

    RheologyOut_M7_L500_3p=transpose(RheologyOut_M7_L500_3p);
    save RheologyOut_M7_L500_3p.mat
```